2015

Nanoarchitectured Energy Storage Devices

Zenan Yu
University of Central Florida

STARS Citation
Yu, Zenan, "Nanoarchitectured Energy Storage Devices" (2015). *Electronic Theses and Dissertations, 2004-2019*. 1498.
https://stars.library.ucf.edu/etd/1498

NANOARCHITECTURED ENERGY STORAGE DEVICES

by

ZENAN YU
B.S. Shanghai University, 2011

A dissertation submitted in partial fulfillment of requirements
for the degree of Doctor of Philosophy
in the Department of Materials Science and Engineering
in the College of Engineering & Computer Science
at the University of Central Florida
Orlando, Florida

Spring Term
2015

Major Professor: Jayan Thomas

ABSTRACT

Supercapacitors, the devices that connect the gap between batteries and conventional capacitors, have recently attracted significant attention due to their high specific capacitance, substantially enhanced power and energy densities, and extraordinary cycle life. In order to realize even better performance with supercapacitors, rejuvenated effort towards developing nanostructured electrodes is necessary.

In this dissertation, several strategic directions of nanoarchitecturing the electrodes to enhance the performance of supercapacitors are investigated. An introduction and background of supercapacitors, which includes motivation, classification and working principles, recent nanostructured electrode materials studies, and devices fabrication, are initially presented. A facile method, called Spin-on Nanoprinting (SNAP), to fabricate highly ordered manganese dioxide (MnO_2) nanopillars is introduced. The SNAP method that is further modified to develop carbon nanoarray electrodes is also discussed. Subsequently, a template-free method to develop high aspect ratio copper oxide nanowhiskers on copper substrate is presented, which boosts the surface area by 1000 times compared to non-nanostructured copper substrate. Electrochemically deposited MnO_2 on the nanostructured substrate provided a specific capacitance of about 1379 F g^{-1} which is very close to the theoretical value (~ 1400 F g^{-1}) due to this efficient nanostructure design. In addition, a novel method to decorate metal nanoparticles on graphene aerogel, which considerably enhances the electronic conductivity and the corresponding specific capacitance, is demonstrated. Moreover, ferric oxide (Fe_2O_3) nanorods prepared by a simple hydrothermal method is discussed. Asymmetric devices assembled based on Fe_2O_3 nanorods and MnO_2 nanowhiskers show excellent electrochemical properties. The devices not only display the capability to store energy but also transmit electricity through the inner copper core. These two functions are independent and do not interfere with each other. Finally, a summary of this dissertation as well as some potential future directions are presented.

To my wife and parents

ACKNOWLEDGMENT

It is with immense gratitude that I acknowledge the support and help of my family, friends and committee members who contributed to the completion of this degree.

I wish to thank, first and foremost, my advisor, Dr. Jayan Thomas, for being a tremendous mentor for me throughout my graduate study. He has the attitude and the essence of a great scientist: he constantly and convincingly instilled a spirit of adventure with respect to research and scholarship. His support, wisdom and commitment to the highest standards motivated me all the time. He acts as a role model of being a good scientist whom I can learn from.

I am also grateful to the committee members. Dr. Sudipta Seal, Dr. Jiyu Fang, and Dr. Kalpathy Sundaram, thanks for the encouragement, time, and attention. I would like to extend my deep gratitude to Dr. Lei Zhai for his contributions towards my intellectual and professional growth at the University of Central Florida.

I also thank Dr. Laurene Tetard, Dr. Ming Su, and Dr. Yajie Dong for their kind suggestions in both research and life.

I would like to thank my wife whose love and support kept me strong for all the days we spent apart to pursue this degree. I am most fortunate to have such a great friend and partner, who never failed to boost my ego during the hardest and frustrating times of my study. I could not have done this without her.

I am truly indebted to my parents whose love, patience and faith inspired me to begin this journey. Their prayers and teachings have been immeasurably valuable.

I thank my colleagues who share their enthusiasm and comments on my work: Dr. Binh Duong, Chao Li, Panit Chantharasupawong, Dr. Chaoming Wang, Julian Moore, Danielle Abbitt, Matthew McInnis, Jean Calderon, Dr. Guangming Tao, Shashank Saraf, and Swetha Barkam.

I like to thank my friends, especially Andy Huffman, Erin Huffman, Fanchao Yi, Minpei Wang, Qinsheng Li, David Shen, and Edward Shen for their friendship, encouragement, and advices.

Most of all, I give thanks to God for giving me the determination to pursue this degree, the wisdom to conquer the barriers of culture and language and the persistence in finding truth. Without his faithfulness and guidance, I would not have been able to go this far and finish this degree.

TABLE OF CONTENTS

LIST OF FIGURES

1 INTRODUCTION[*]

1.1 Motivation

Today, research community and industry have invested considerable effort in developing renewable and sustainable energy sources. In order to fully utilize these sources, compatible energy storage systems need to be developed as well. Among energy storage systems, supercapacitors have drawn considerable attention during recent years due to their fast charge-discharge characteristics, high power density, and excellent cycle stability. Currently, supercapacitors are used along with batteries to provide the additional power required in many applications. However, they cannot be used as stand-alone units in these applications since their energy density is inferior to that of batteries. For example, commercially available supercapacitors can provide energy densities of less than 10 Wh Kg^{-1} whereas Li-ion batteries can provide energy densities of more than 180 Wh Kg^{-1}.[1, 2] Nevertheless, the power density and cycle life of supercapacitors are far superior to those of Li-ion batteries. At present, the scientific community is striving to considerably improve the energy and power densities of supercapacitors by developing new electrode materials and electrolytes, and ingenious device design.

Achieving noteworthy improvements in supercapacitor performances by means of better electrode materials together with low-cost and environment-friendly production require a deep fundamental understanding of the charge storage mechanisms, transport pathways of electrons and ions and electrochemically active sites. Advances in nanomaterials, ideal candidates for improved ion adsorption or faster surface redox reactions, have fostered extensive research

---

[*] The work presented in this chapter is an extension of Z. Yu, L. Tetard, L. Zhai, and J. Thomas. *Energy Environ. Sci.* 2015, 8, 702-730. Reproduction has been permitted by © 2015 Creative Commons.

efforts toward the enhancement of electrochemically active sites for charge transfer and controlled ionic and electronic transport at small diffusion length scales.

Therefore, this dissertation focuses on several nanoarchitectured designs for enhancing supercapacitor's performance.

1.2 Chapter Outline

Chapter 2 starts with background discussion which includes introduction of supercapacitors, nanostructured electrode materials, and device fabrication. This section gives a comprehensive review of supercapacitors.

After the background information, synthesis and capacitive behavior of MnO_2 nanopillars is presented in Chapter 3. This chapter includes a three-step approach to easily obtain highly ordered MnO_2 nanoarrays and their electrochemical performance as supercapacitor electrodes.

In Chapter 4, symmetric supercapacitor devices based on carbon nanopillars is presented. Carbon nanopillars can be produced by the carbonization of polymer nanopillars that are obtained by a simple spin-on nanoprinting technique. Symmetric supercapacitor devices are assembled by two identical electrodes with carbon nanopillars and tested in a two-electrode system.

Chapter 5 presents symmetric supercapacitors with MnO_2 nanowhiskers. In this Chapter, a template-free method to fabricate high aspect ratio one dimensional nanostructures is introduced. MnO_2 can be subsequently deposited on these nanostructures. In addition, the symmetric supercapacitors are assembled in a cable shape, which allows high flexibility and excellent bendability.

Subsequently, in Chapter 6, fabrication of asymmetric supercapacitors with functionalized graphene aerogel and MnO_2 is presented. A novel method is introduced to decorate graphene nanosheets with metal nanoparticles. Asymmetric supercapacitors are assembled using functionalized graphene aerogel as anodes and MnO_2 thin film as cathodes.

In Chapter 7, fabrication of asymmetric supercapacitors with Fe_2O_3 nanorods and MnO_2 nanowhiskers is discussed. A simple hydrothermal method is introduced to synthesis FeOOH nanorods, followed by post annealing to obtain Fe_2O_3 nanorods. MnO_2 nanowhiskers are produced using the same method described in Chapter 5. Coil-type asymmetric supercapacitors are assembled by coiling the anodes (Fe_2O_3) on cathodes (MnO_2) with a separator in between.

Chapter 8 concludes this dissertation and possible future directions.

1.3 References

1. B. E. Conway, *Electrochemical Supercapacitors: Scientific Fundamentals and Technological Applications*, Springer, New York, 1999.

2. P. Simon and Y. Gogotsi, *Nat. Mater.*, 2008, **7**, 845-854.

2 BACKGROUND[*]

2.1 Introduction of Supercapacitors

2.1.1 Classification and Working principles

Supercapacitors are electrochemical capacitors with high capacitances that could reach values up to 10,000 farads at an output potential of 1.2 V, which bridges the gap between batteries and conventional capacitors. Supercapacitors are generally classified into two types based on their storage mechanism, the electrochemical double layer capacitors (EDLCs) and pseudocapacitors. EDLCs physically store charges via reversible ion adsorption at the electrode-electrolyte interface, while pseudocapacitors chemically store their charges via redox reaction at the vicinity (a few nanometers) of the surface.

Figure 2.1 a and b illustrate the working principal of EDLCs and pseudocapacitors with half-cell configuration (the counterpart half-cell configurations are identical with opposite charges/ions). In figure 2.1a, when an electrical field is applied on an EDLC, a layer of polarized solvent molecular layer (*e.g.* water molecule if water solvent is used) called inner Helmholts plane (IHP) will form and closely attach to the electrode surface due to physical forces (*e.g.* electrostatic force). The electrical double-layers are generated on the left and right sides of the IHP that serves as molecular dielectric. On the right side, a layer is formed from the solvated and dissolved ions in the electrolyte; while on the left side, a layer is emerged on the surface lattice structure of the electrode. The amount of charges stored in an EDLC (*i.e.* capacitance) can be calculated via the formula for conventional capacitors: $C = \mathcal{E}A/D$, where $\mathcal{E}$ is the permittivity of

---

[*] The work presented in this chapter is an extension of Z. Yu, L. Tetard, L. Zhai, and J. Thomas. *Energy Environ. Sci.* 2015, 8, 702-730. Reproduction has been permitted by © 2015 Creative Commons.

materials, *A* is the electrode surface area, and D is the distance between two electrodes. In typical EDLC designs, activated carbons that have giant surface area *A* are used plus the extremely tiny distance *D* due to the thin thickness of IHP, which results in substantially improved capacitance compared to conventional capacitors.

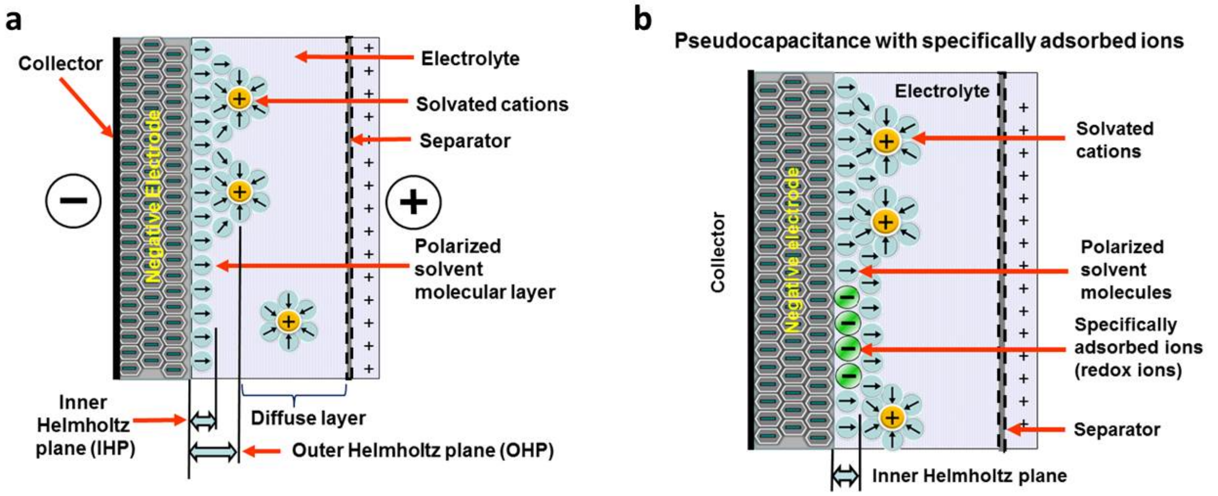

Figure 2.1 Working principal of (a) EDLCs and (b) pseudocapacitors. Copyright under Creative Commons CC0 1.0, meaning there is no limitation to copy, modify, distribute, and perform the work without asking permission.

In Figure 2.1b, when an electric field is applied on a pseudocapacitor, an electrical double-layer will be formed, which is same as that in EDLCs. In addition to the electrical double-layer, some ions in the electrolyte will be adsorbed on the surface of electrode and charge-transfer will take place between the electrode atoms and ions. This charge-transfer is originating from reversible redox, intercalation, or electro-adsorption processes. This charge-transfer process allows more charges stored at the interfaces between electrode and electrolyte. As a result, pseudocapacitors typically have more capacitance (up to 100 times) than EDLCs with the same surface area, depending on the electrode materials and the structures of electrodes.

2.1.2 Evaluation criteria and influencing factors

The criteria for designing a high-performance supercapacitor electrode include high specific capacitance (energy stored per unit mass, volume, or area of active materials), large rate capability (capacitance retention at high scan rate or current density), and high cycle stability. In addition, the toxicity and cost of the active materials used in an electrode design should be taken into account as well. Therefore, in order to realize a high-performance supercapacitor electrode, factors that determine the specific capacitance, rate capability, and cycle stability need to be mentioned here. (1) Surface area: Since charges are stored on the surface of the supercapacitor electrodes, an electrode with a higher surface area leads to an improved specific capacitance. Nanostructuring of electrode materials is a feasible method to considerably improve the surface area of the electrodes. (2) Electronic and ionic conductivity: As specific capacitance and rate capability are considerably dependent on both electronic and ionic conductivity, a high electronic and ionic conductivity will help to maintain the rectangular nature of cyclic voltammetry (CV) curve and symmetric nature of galvanostatic charging-discharging (GCD) curves. They also reduce the specific capacitance losses as scan rates/current densities are increased. Typical approaches to enhance the electronic conductivity include binder-free electrode design and nanostructured current collector design to provide efficient electron pathways for charge transport. To increase the ionic conductivity, precise control of pore size and prudent design strategies are used (e.g. more open structures for ion transport). (3) Mechanical and chemical stability: The cycle stability is greatly influenced by the mechanical and chemical stability of electrode materials during cycling. Phase change, dissolution, and side reaction of active materials are the major reasons for causing cycle instability. Sensible electrode surface protection may substantially boost the cycle stability.

2.1.3 Electrode Materials

Figure 2.2 exhibits a hierarchical diagram of electrode materials for supercapacitors. Typically, electrode materials for EDLCs are made of carbon-based materials (including activated carbons, carbon aerogels, carbon nanotubes (CNTs), and graphene), while that for pseudocapacitors are conducting polymers (*e.g.* polypyrrole, polyaniline, poly(3,4-ethylenedioxythiophene), *etc.*), metal oxides (*e.g.* RuO_2, MnO_2, CoO_x, NiO, Fe_2O_3, *etc.*), metal dichalcogenides (*e.g.* MoS_2, VS_2, *etc.*), and metal carbides/nitrides ($Ti_3C_2T_x$, VN, TiN, *etc.*).

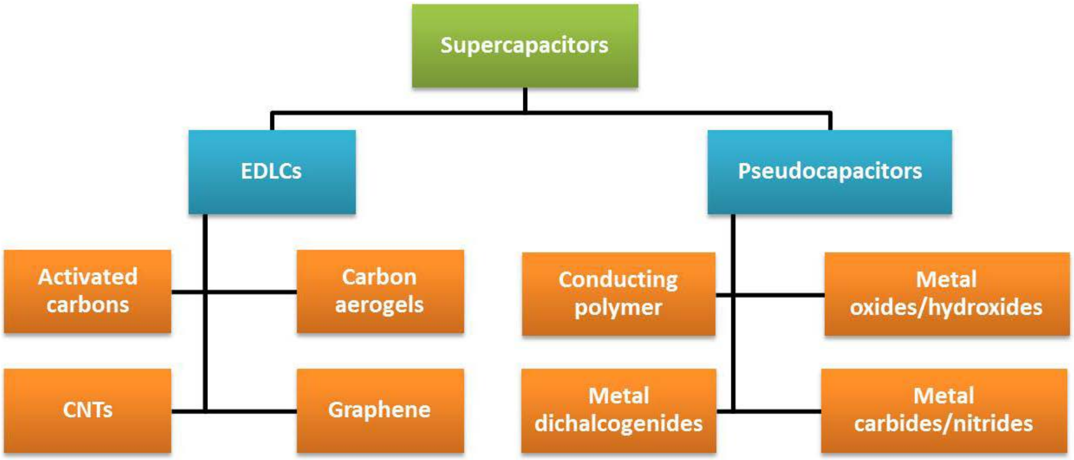

Figure 2.2 Electrode materials for supercapacitors.

2.2 Nanostructured Electrode Materials

Typically, nanomaterials can be classified into zero dimensional (0D), one dimensional (1D), two dimensional (2D) and three dimensional (3D) categories.[1-3] Particles which are more or less spherical in shape like fullerenes, quantum dots, nano-onions, nanoparticles, etc. are considered as 0D. Nanostructures with 1D are interesting due to their dimensionality dependence on its functional properties. They include nanotubes, nanofibers, nanowires, nanopillars, nanoribbons and nanobelts. Typically, materials with a thickness of a few atomic layers and with the other two dimensions beyond the nanometric size range are considered as 2D materials. Graphene and many other layered van der Waals solids like $MoS_{2,}$ $CaGe_2$ and $CaSi_2$, fall under the 2D category. Materials with three dimensions beyond the nanometric size range but still preserve the advantages of nano size effect are regarded as 3D materials. Mesoporous carbon and graphene aerogel fall under 3D category.

2.2.1 0D Electrode Materials

According to the strict definition, 0D nanostructures are spherical particles that have three dimensions constrained on the nanoscale (usually 1 – 100 nm). Nevertheless, particles with diameters up to 1 μm are usually regarded as nanoparticles as well, as the benefit provided by the effect of their small size has been observed for this size range. In this section, three subcategories of 0D nanostructures used as electrodes in supercapacitors are considered, *viz.*, solid, hollow, and core-shell 0D nanostructures.

2.2.1.1 Solid 0D Nanostructures.

As the foundation of 0D nanostructures, solid nanoparticles (nanospheres) are the most intensely investigated for designing supercapacitor electrodes. Carbon materials (e.g. activated carbon,[4] carbon nanospheres,[5] and mesoporous carbon[6, 7]) and transition metal oxides (e.g. MnO_2,[8, 9] NiO,[10-12] Fe_3O_4,[13] etc.) have been widely fabricated into solid nanoparticles for electrode materials. Among carbon materials, activated carbons (ACs) are distinct due to their high surface area (up to 3000 m^2 g^{-1}) and economical fabrication process. In addition, ACs propose a wide range of pore size distribution including micropores (< 2 nm), mesopores (2 – 50 nm), and macropores (> 50 nm).[14] ACs are generally produced by either physical or chemical activation of versatile carbonaceous precursors such as wood, coal, nutshell, and so forth. Larger surface area is usually expected to result in a higher specific capacitance. However, even with a surface area of up to 3000 m^2 g^{-1}, only small specific capacitance (<10 μF cm^{-2}) could be obtained with ACs.[15] This is due to the fact that specific capacitance is not only determined by surface area but also by other parameters such as pore size distribution, pore shape and structure, accessibility of the electrolyte, and electrical conductivity.[16] Therefore, an ideal design of ACs should meet at least two requirements: (1) large surface area for the enhancement of electrochemically active sites and (2) suitable pore size and structure for the transportation of ions in the electrolyte. In addition to ACs, Gogotsi, Simon, and their co-workers have prepared onion-like carbon by annealing nanodiamond powder at 1800 ºC.[17, 18] The carbon onions were found to possess a moderate specific surface area (~ 500 m^2 g^{-1}) compared to ACs; however, the surface can be fully accessed by ions. As a result, micro-supercapacitors based on these onion-like carbons showed ~70% rate capability from 1 to 100 V s^{-1} and an excellent relaxation time constant (26 ms) compared to that of activated carbon (700 ms).

The above mentioned criteria for designing ideal ACs are also applicable to transition metal oxide nanoparticles in pseudocapacitors as they rely on fast surface redox reactions. Additionally, as most of the transition metal oxides suffer from poor electrical conductivity, enhancing the bulk electrical conductivity should also be taken into account. For example, Chen and co-workers have fabricated nanoporous metal/oxide hybrid supercapacitor electrodes in order to enhance the electrical conductivity of MnO_2.[19] In this method, conductive nanoporous gold was first produced by de-alloying $Ag_{65}Au_{35}$ using HNO_3, followed by growing nanocrystalline MnO_2 (with a grain size of ~ 5 nm) into the nanopores. The resulting nanoporous Au/MnO_2 supercapacitor electrode showed a high specific capacitance of ~ 1145 F g^{-1} at 50 mV s^{-1}, which can be attributed to nanoporous gold that allows easy and efficient access to both electrons and ions. Recent advances in using perovskite materials for solar energy harvesting have greatly stimulated the enthusiasm of researchers to exploit these materials for other potential fields. Lately, Stevenson, Johnston, and co-workers have prepared $LaMnO_3$ nanoparticles via reverse-phase hydrolysis method as supercapacitor electrode material.[20] They have found that oxygen intercalation has significant effect on $LaMnO_3$ perovskite nanoparticles as supercapacitor electrodes. The specific capacitances of $LaMnO_{3.09}$ and $LaMnO_{2.91}$ reached 586.7 and 609.8 F g^{-1}, respectively. Interestingly, the capacitance difference (~ 4%) was found to be close to the oxygen content difference (~ 6%), implying that the oxygen intercalation is the major charge storage mechanism of $LaMnO_3$ perovskite supercapacitor electrodes. This assumption was further demonstrated by applying electrolyte with varying anion concentrations as well as different electrolyte types (i.e. neutral and alkaline electrolytes). As a result, perovskite-type materials with anion vacancies can be exploited to store charge through oxygen intercalation. Therefore, in addition to traditional solid 0D active materials (e.g. activated carbon), perovskite materials might open a new paradigm as supercapacitor electrode materials.

2.2.1.2 Hollow 0D Nanostructures.

Hollow 0D nanostructures have been recognized as promising candidates for electrode design due to their peculiar properties such as low density, high surface-to-volume ratio and shortened pathways for transporting both mass and charges.[21] Hollow 0D nanostructures are generally synthesized via three distinct approaches: hard templating, soft templating, and template-free methods. Among them, hard templating methods have been widely adopted because of their remarkable advantages in controlling the size, shape, and structure of the products.[22] Typically, a single-shelled hollow nanosphere is created by coating a thin layer of precursor materials onto a spherical hard template (e.g. silica spheres, polystyrene colloid spheres, carbonaceous spheres, etc.), followed by removing the template either by calcination or by chemical etching. For example, Yang and co-workers reported the synthesis of hollow carbon nanospheres by carbonizing its hollow nanosphere precursor obtained through a silica sphere-assisted hard templating method.[23] The resulting hollow carbon nanospheres showed a high surface area (1704 m^2 g^{-1}), large bimodal mesopores (6.4 and 3.1 nm), and large pore volumes (1.6 cm^3 g^{-1}). With such a design, a specific capacitance of 251 F g^{-1} at 50 mV s^{-1} was achieved for the hollow carbon nanospheres. Hollow 0D structures based on other electrode materials such as MnO_2,[24, 25] NiO,[26, 27] NiS,[28] etc. have been investigated as well.

In addition to single shelled hollow 0D nanostructures, multiple shelled samples have also shown fascinating characteristics (e.g. substantially improved surface-to-volume-ratio) for efficient electrode material design. Similarly, electrode materials like NiO,[29] Co_3O_4,[30] and Fe_2O_3,[31] have been successfully fabricated into multi-shelled structures. For example, Zhang and co-workers reported the synthesis of NiO hollow nanospheres via layer-by-layer (LBL) self-assembly for supercapacitor application.[29] In their method, the number of shells was directly determined by the cycles of immersion-precipitation process before removing the carbonaceous template via calcination (Figure 2.3a). Single, double, and triple shelled NiO nanospheres were prepared by repeating the immersion-precipitation process for 0, 1, and 2 times (Figure 2.3b – c). The double-shelled NiO nanospheres exhibited the highest surface area (92.00 m^2 g^{-1}), which ascribes to their more loosely-packed structure compared to their single and triple shelled counterparts. As a result, the double shelled NiO nanospheres showed the most enhancement in specific capacitance (612.5 F g^{-1}). Since many other promising electrode materials have not been fabricated into 0D multi shelled structures, much effort still needs to be dedicated in the future.

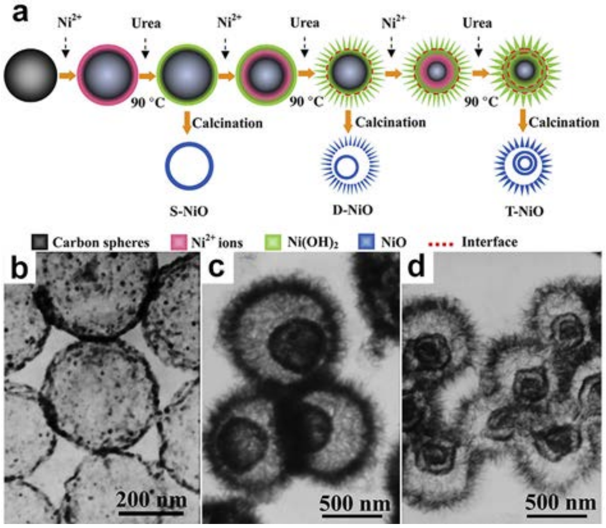

Figure 2.3 (a) Schematic of synthesizing multishelled NiO hollow nanospheres using LBL self-assembly. TEM images show NiO hollow nanospheres with (a) single-shell, (b) double-shells, and (c) triple-shells. Reproduced with permission from ref. 29. Copyright 2014 Elsevier.

2.2.1.3 Core-Shell 0D Nanostructures.

Core-shell 0D nanostructures often refer to a solid or hollow nanoparticle coated with a thin shell. Combing faradaic and non-faradaic materials into core-shell 0D nanostructures offer considerable advantages including enhanced electrical conductivity, less agglomeration, robust chemical and mechanical stability, etc.[32-35] For example, Zhao and co-workers have grown conducting polymer (polyaniline (PANI)) on hollow carbon spheres as supercapacitor electrode materials.[32] Hollow carbon spheres (HCS) with high specific area (2239 m^2 g^{-1}) were first prepared using ferrocene as the carbon precursor and silica spheres as the template. PANI was then conformally grown on the surface of the HCS by polymerizing aniline at room temperature for 12h. HCS-PANI core shell structures with an optimized content of PANI showed a specific capacitance of 525 F g^{-1}, which is almost two times greater than that of pristine HCS (268 F g^{-1}). However, the rate capability of HCS-PANI decayed with increasing PANI content, which can be attributed to the pore blockage due to the reduced accessibility of electrolyte ions. Zhao's group also synthesized core-shell nanoparticles with carbon core and MnO_2 shell by direct redox reaction between graphitic hollow carbon spheres (GHCS) and $KMnO_4$ solution at 70 °C.[33] The as-prepared GHCS-MnO_2 core-shell nanostructures showed a maximum specific capacitance of 190 F g^{-1} at 0.1 A g^{-1} with an optimized MnO_2 content (64 wt%), more than two times higher than that of pristine GHCS (95 F g^{-1}). Moreover, the GHCS-MnO_2 core-shell nanostructures maintained 55% capacitance retention while current density increased from 0.1 to 10 A g^{-1}, indicating a porous structure of MnO_2 shell was formed to provide efficient diffusion pathway for electrolyte ions.

2.2.2 1D Electrode Materials

1D nanostructures are slivers of material with two dimensions constrained on nanoscale.[36] They have been extensively studied for the design of electrode materials for supercapacitors due to their unique and superior chemical and physical properties. For instance, the longitudinal axle of 1D nanostructures can provide efficient transport pathway for both electrons and ions,[37] while maintaining the similar benefits of 0D nanostructures in the two nanoscale dimensions. In this section, we place 1D nanostructures into two major categories: homostructures and heterostructures.

2.2.2.1 1D Homostructures

1D homostructures are structures with only one singular structure such as nanorods, nanowires, nanotubes, *etc*. They can be divided into three groups, namely, nanorods/nanopilars with aspect ratios (length/diameter) less than 10, nanowires with aspect ratios more than 10, and nanotubes with hollow interiors.[38] The methods for synthesizing 1D homostructures are versatile and can generally be divided into two major types, template-assisted and template-free methods. For template-assisted methods, sacrificial templates (*e.g.* AAO templates) are commonly used to shape the initial structure, followed by the removal of the templates with an acidic or basic solution. For template-free methods, various approaches like hydrothermal synthesis, chemical vapor deposition (CVD), and electrodeposition are generally employed to directly grow 1D homostructures. Recently, vertical growth of active material on the conductive substrate either by a “bottom-up” or “top-down” method has become one of the most promising electrode design approaches. Such a design guarantees efficient transport of electrons between current collector and active material because of the binder-free design. It also enables fast transfer of ions between electrolyte and active materials because of the available void space between adjacent nanostructures.

Nanorods/nanopillars. Although the moderate aspect ratio of nanorods/nanopillars limits the enhancement of surface area compared to nanowires/nanofibers, the significantly lower chances for individual nanorod/nanopillar to collapse or clump into its neighboring structures makes them more accessible to the electrolyte, which effectively increases the ionic conductivity.

Tong and co-workers have reported oxygen-deficient Fe_2O_3 nanorods as supercapacitor electrode material.[39] Nanorod-like FeOOH was first hydrothermally synthesized in an aqueous solution containing ferric chloride, sodium nitrate, and hydrogen chloride. Subsequently, the FeOOH nanorods were heated at high temperature in air and N_2, separately, which resulted in pristine Fe_2O_3 nanorods and oxygen-deficient Fe_2O_3 nanorods. Interestingly, the oxygen-deficient Fe_2O_3 nanorods exhibited more than two times of the specific capacitance (64.5 F g^{-1}) enhancement than that of pristine Fe_2O_3. This phenomenon may be attributed to the existence of oxygen vacancies which considerably enhance the donor density and in turn improve the conductivity and reactivity of Fe_2O_3 nanorods.

Nanowires. Nanowires have been widely studied as electrode material due to their high aspect ratio that can provide large surface area to store charges and an efficient pathway to transport charges. Taking PANI nanowires as an example, Li and co-workers have synthesized vertically aligned PANI nanowires as supercapacitor electrodes by means of electrochemical deposition using AAO templates.[40] The electrochemical deposition was carried out at a constant potential of 0.75 V for 5000 s in an electrolyte solution containing aniline and sulfuric acid. PANI nanowire arrays were obtained upon removing the AAO template in a 0.01 M NaOH solution. These samples showed a specific capacitance of 1142 F g^{-1} at a current density of 5 A g^{-1}, with 5% capacitance fading after 500 cycles. Regardless of the superior electrochemical performance of PANI nanowires, the usage of AAO templates limits the practicality of this fabrication process for large scale production since a new AAO template is required for every array of nanostructures produced. Lately, Wei and co-workers reported a facile one-step template-free approach to synthesize PANI nanowire arrays.[41] In their method, PANI nanowire could directly be electropolymerized by a simple galvanostatic deposition process at a constant current of 0.01 mA cm^{-2} for 1 h. Consequently, the as-prepared PANI nanowire arrays showed 950 F g^{-1} at a current density of 1 A g^{-1} and 16% loss after 500 cycles.

Lately, a ternary metallic oxide, spinel nickel cobaltite ($NiCo_2O_4$), has attracted substantial attention due to its high conductivity (more than two orders of magnitude higher than single NiO or Co_3O_4) and multiple oxide states that enable rich redox reactions originating from both nickel and cobalt ions.[42, 43] For example, Lou and co-workers have successfully grown $NiCo_2O_4$ nanoneedle arrays directly on conductive substrates as supercapacitor electrodes.[44] In their synthetic process, a conductive substrate was first immersed into a solution containing nickel nitrite, cobalt nitrite, ethanol, and water in an appropriate ratio and heated to 85 °C for 8h, followed by annealing at 250 °C for 90 min. Remarkably, the $NiCo_2O_4$ nanoneedle arrays showed a capacitance of 1118.6 F g^{-1} and about 10.6% loss in capacitance after 2000 cycles.

Nanotubes. Compared to solid nanostructures (e.g. nanowires), tubular nanostructures typically offer higher surface area with less utilization of mass, resulting in more gravimetric specific capacitance. Nanotubes are usually synthesized via template-assisted method, CVD, hydrothermal method, etc. For template-assisted method, nanotubes can be easily prepared by partially infiltrating the nanotube forming material into a nanoporous template. This is due to the fact that materials preferentially anchor on the walls of nanochannels at their early infiltrating stage. Therefore, it is critical to manipulate the infiltration process in order to produce tubular nanostructures. For example, MnO_2 nanotube arrays were synthesized using AAO template via electrochemical deposition for 10 min; whereas MnO_2 nanowire arrays were obtained after 60 min of deposition.[45] The MnO_2 nanotube arrays showed a specific capacitance of 320 F g^{-1}, while only 101 F g^{-1} was measured for the nanowire arrays. Using the same strategy, other electrode materials were synthesized with tubular nanostructure such as RuO_2,[46] PEDOT,[47] etc.

The discovery of carbon nanotubes (CNTs) has led to several applications in energy storage field. CNTs as supercapacitor electrode materials, and especially vertically aligned CNTs directly grown on conductive substrates, have drawn remarkable attention due to their moderate to high surface area (120 – 500 m^2 g^{-1}), porous structure, superior electronic conductivity, and excellent mechanical and thermal stability. Ajayan and co-workers have grown aligned CNTs (400 μm long) on metal alloy (Inconel) using vapour-phase catalyst delivery.[48] The CV curves showed rectangular and symmetric shape even at a scan rate of 1000 mV s^{-1}, suggesting ideal capacitive behavior and low contact resistance between the CNTs and the substrate. The specific capacitance of a supercapacitor based on these vertically aligned CNT arrays was found to be 18 F g^{-1}. Iijima and co-workers reported a method to prepare densely packed and aligned CNTs using zipping effect as supercapacitor electrode material.[49] The specific capacitance of the aligned CNTs showed 80 F g^{-1}, which is roughly twice the value of 45 F g^{-1} for the entangled CNTs. Recently, Kim and co-worker have grown vertically aligned CNTs directly on conductive carbon papers using an Al/Fe catalyst via water-assisted CVD.[50] These aligned CNTs exhibited a specific capacitance of about 200 F g^{-1} at 20 A g^{-1}.

2.2.2.2 1D Heterostructures

Unlike homostructures, heterostructures usually consist of more than one component. One major advantage of using heterostructured electrode design is the synergic improvement of intrinsic properties of each component for better electrical conductivity, faster ionic transport, greater electrochemical reversibility and cycle stability, and improved mechanical stability. Owing to these advantages, 1D heterostructures are currently considered as one of the potential candidates for the next generation electrode designs.

Core-shell 1D heterostructures. Core-shell 1D heterostructures often refer to a 1D nanostructure (e.g. nanorod, nanowire, nanotube, etc) coated with a thin shell. Among various heterostructures, core-shell heterostructures have received considerable attentions due to their unique structural properties that can effectively decline the surface energy which reduces the aggregation possibility of active materials as well as relieves side reaction between electrode and electrolyte, resulting in better reversibility and cycle stability of electrodes. Therefore, rational synthesis of advanced core-shell heterostructures with fascinating synergetic properties offers a promising approach to improve electrochemical performance. Typically, most of the core-shell heterostructures are prepared by initially creating a 1D nanostructured core backbone, followed by sheathing the shell materials. Various methods have been explored in order to obtain such advanced configuration including sputtering, electrochemical deposition, hydrothermal synthesis, CVD, electrospinning, etc. Due to the versatile combinations of electrode materials in terms of core and shell in a core-shell design, herein they are simply grouped into two categories: (a) current collector core – active material shell and (b) active material core – active material shell. For the convenience of discussion, we denote material A (core) and material B (shell) as A@B for the remainder of the manuscript.

(a) Current collector core – active material shell: In this configuration, 1D nanostructured current collector core can provide shortened pathways for electron transport, which effectively enhances the available electrochemically active sites. Owing to the high electrical conductivity as well as excellent mechanical stability, metals have been selected as pivotal current collector candidates. When metals are forged into 1D nanostructures like nanowires or nanotubes, active materials can be deposited onto these 1D metal nanostructures and hence form core-shell 1D nanostructured electrode materials. There are several approaches to synthesize 1D metal nanostructures including template-assisted preparation,[51-54] soft solution processing,[38, 55, 56] vapor phase synthesis,[57-59] and self-assembling.[60, 61] Among them, template-assisted preparation is the most intensively studied method for 1D metal nanostructure synthesis. Particularly, 1D metal nanostructures can be fulfilled by either shaping with the help of sacrificial templates (e.g. AAO) or directly coating active material on supercapacitive-inactive 1D nanostructures. For the former case, a pioneering work led by Teberna and co-workers reported Cu nanowire array prepared using AAO template as current collector, which was subsequently deposited with active materials (Fe_3O_4).[54] Following a similar concept, other works have been demonstrated such as Ni@MnO_2,[62, 63] Ni@NiO,[64] Au@MnO_2,[65] Ni@Co_3O_4,[66] Mn@MnO_2,[67] etc. For the latter, since the inert core does not give any contribution to the electrochemical properties, the metal coated structure is still regarded as the current collector core.

In addition to metals, other materials such as ZnO, SnO_2, Zn_2SnO_4, and ITO have been fabricated into 1D nanostructures and served as current collector cores to deposit active material shells.[68-75] To date, most 1D current collectors are either nanowires or nanorods, while reports about nantubular current collectors are relatively few. However, electrodes based on nanotubular current collectors show promising results since both inner and outer surfaces can be utilized for depositing active materials.

(b) Active material core – active material shell: Active material core – active material shell presents another promising combination of 1D core-shell heterostructures due to both core and shell materials contributing to electrochemical performance. Generally, active materials used in supercapacitors can be classified into two groups: EDLC materials and pseudocapacitive materials. There can be four types of core-shell combinations, namely, EDLC material core – EDLC material shell, EDLC material core – pseudocapacitive material shell, pseudocapacitive material core – EDLC material shell, and pseudocapacitive material core – pseudocapacitive material shell. Among these categories, EDLC material core – pseudocapacitive material shell and pseudocapacitive material core – pseudocapacitive material shells are the two major players.

EDLC material core and pseudocapacitive material shell constitutes an appealing combination of core-shell design due to the following merits: (1) EDLC materials as core have better cycle stability due to their electrostatic charge and discharge storage mechanism (i.e. no phase changes), which makes them robust backbones even for large number of cycles; (2) Also EDLC core material have better electrical conductivity compared to pseudocapacitive materials, which facilitates the transportation of electrons; (3) pseudocapacitive materials as shell can effectively offset the low capacitance contribution from EDLC materials core. In this regard, Zhai and co-workers have demonstrated the feasibility of EDLC material core and pseudocapacitive material shell such as CNT@PPy-MnO_2,[76] CNT@PEDOT-MnO_2,[77] and CNT@PANI-MnO_2.[78] In CNT@PPy-MnO_2, multiwall CNTs were first well-dispersed and wrapped around using 18 wt% Poly(4-styrenesulfonic acid) (PSS), which also provides attractive forces for pyrrole and metal ions upon negative charging. PPy-MnO_2 composite shell was subsequently prepared by adding pyrrole and $KMnO_4$. As a result, CNT@PPy-MnO_2 core-shell nanowires showed ~ 268 F g^{-1} specific capacitance, which is much higher than CNT@MnO_2 (~170 F g^{-1}) and CNT@PPy (~160 F g^{-1}). Significantly, 93% rate capability of CNT@PPy-MnO_2 was retained from 5 to 100 mV s^{-1}, while only 35% and 72% were retained by CNT@MnO_2 and CNT@PPy respectively in the same scan rate range when tested separately. Moreover, CNT@PPy-MnO_2 exhibited very stable cycle life (10% reduction after 5000 cycles); in contrast, a specific capacitance reduction of 61% and 45% was observed under the same test conditions for CNT@MnO_2 and CNT@PPy, respectively.

A similar strategy reported by Ajayan and co-workers is the combination of CNT core and MnO_2 shell.[79, 80] First, MnO_2 nanotubes were obtained by vacuum infiltrating manganese nitrate solution into an AAO template pre-electrodeposited with Au, followed by subsequent annealing in the air at 300 °C for 10 h. CNTs were then grown on the inner void left by the MnO_2 shells by CVD process and hence obtained CNT@MnO_2 1D core-shell heterostructure upon removing the AAO template. Significantly, the core-shell arrays showed almost two times enhancement of specific capacitance compared to pure MnO_2. Moreover, no apparent structural change was detected even after 1000 cycles, indicating remarkable mechanical and cycle stability.

Pseudocapacitive material core – pseudocapacitive material shell presents another intriguing core-shell design because both core and shell materials have redox reactions during charge and discharge processes, which results in high specific capacitances. In this regard, Fan's group has synthesized versatile combinations of pseudocapacitive materials with 1D core-shell heterostructures including Co_3O_4@MnO_2,[81] CoO@NiHON,[82] Co_3O_4@NiO,[83] CoO@TiO_2,[84] and Co_3O_4@PEDOT-MnO_2.[85] Taking Co_3O_4@MnO_2 core-shell nanowires as an example, Co_3O_4

nanowire core was first hydrothermally grown for 5 h, followed by coating a thin carbon layer and hydrothermal deposition of MnO_2 from a $KMnO_4$ solution at 160 °C for 1 – 5 h. The as-synthesized core-shell heterostructures presented a specific capacitance of 480 F g^{-1} at 2.67 A g^{-1} and excellent rate capability (56% retention with current density up to 44.7 mA cm^{-2}).[81] Following a similar concept, Liu and co-workers further improved the performance by employing $NiCo_2O_4$ instead of Co_3O_4 due to its better electronic conductivity (as mentioned earlier).[86] Consequently, the final product of $NiCo_2O_4@Ni_xCo_{1-x}(OH)_2$ core-shell nanowires considerably increased the specific capacitance up to 1500 F g^{-1} and improved the rate capability up to 67% retention at 90 mA cm^{-2}.

It should be noted that some of the metal oxides, such as V_2O_5, MnO_2 and Co_3O_4, suffer from dissolution issues due to phase changes upon cycling, which gradually erodes the quantity of electrochemically active materials, resulting in poor cycling and mechanical stability.[87-89] Therefore, a rational design like a durable protective coating which can effectively inhibit the structural collapse or break-down of metal oxide core and alleviate the strain generated during cycling is essential. In this regard, conducting polymers are generally selected as promising protective shell materials due to their high stability, mechanical flexibility, and excellent electronic conductivity.[90] For example, Wu and co-workers reported core-shell structure of PPy grown on V_2O_5 nanoribbon for supercapacitors.[87] V_2O_5 nanoribbons were first prepared hydrothermally in a solution containing NH_4VO_3 and poly(ethylene oxide)-block-poly(propylene oxide)-block-poly(ethylene oxide) copolymer at 120 °C. The as-prepared V_2O_5 nanoribbons were dispersed in water by using anionic surfactant. The anionic surfactant also provided electrostatic force to absorb pyrrole at a later stage. After adding pyrrole and $FeCl_3$, a core-shell structured V_2O_5@PPy was obtained (Figure 2.4a). Significantly, a supercapacitor assembled using V_2O_5@PPy as anode and activated carbon as cathode showed less than 5% capacitance fading after 10000 cycles, while one assembled under the same condition without PPy film on the V_2O_5 anode showed 17.5% capacitance loss. This result demonstrates the effectiveness of PPy shell in preventing the dissolution of V_2O_5 upon cycling (Figure 2.4b). Furthermore, the electrolyte for PPy@V_2O_5 electrode after cycling showed transparent color, while yellow electrolyte was observed for the V_2O_5 electrode, indicating that vanadium ions diffuse into the electrolyte without a protective coating. Similarly, other works employing conducting polymers as protective shell have been demonstrated including MnO_2@PEDOT-PSS,[91, 92] Co_3O_4@PANI,[93] MnO_2@PPy,[94, 95] V_2O_5@PEDOT-MnO_2,[96] etc. Further studies are needed to address the relationship between the thickness of protective coating and electrochemical performances (e.g. cycle stability and rate capability). This is because, even though the protective coating could effectively prevent the dissolution issue, it could, in turn, block the accessibility of ions if it is too thick, which impedes the rate capability.

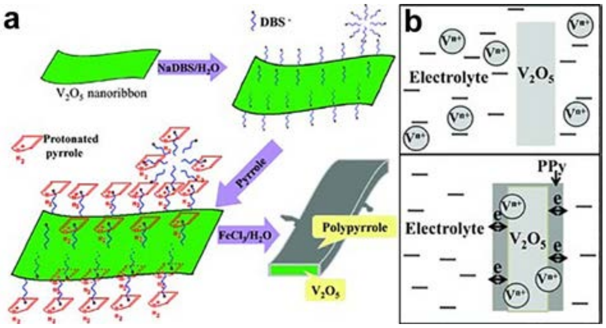

Figure 2.4 (a) Schematic shows the growth of PPy on V_2O_5 nanoribbon surface. (b) PPy shell helps the electronic transport and prevents the dissolution of vanadium in electrolyte. Reproduced with permission from ref. 87. Copyright 2013 WILEY-VCH Verlag GmbH & Co. KGaA, Weinheim.

Other 1D heterostructures. Composites containing 0D and 1D nanomaterials have been extensively studied for other heterostructures as well. For instance, by doping 0D nanomaterials into 1D nanomaterial matrix, Gu and co-workers have prepared vertically-aligned CNT arrays and doped them with MnO_2 nanoflowers by electrochemical deposition.[97] The MnO_2/CNT composites exhibited a specific capacitance of 199 F g^{-1} which is much higher than pristine CNT (27 F g^{-1}) and 97% capacitance retention even after 20000 cycles. This impressive result may be attributed to the employment of CNT arrays, which provides not only high electronic and ionic conductivity but also sturdy mechanical stability. Another example reported by Lee and co-workers was the loading of well-dispersed MnO_2 nanoparticles into PEDOT nanowires.[98] PEDOT nanowires were first prepared by electrochemical deposition of PEDOT in AAO template, followed by removal of the template using NaOH solution. MnO_2 nanoparticles were subsequently loaded into the PEDOT nanowires by soaking the PEDOT nanowires into $KMnO_4$ solution. The MnO_2/PEDOT composites delivered a specific capacitance of 250 F g^{-1} and an 80% rate capability was maintained from 5 to 25 mA cm^{-2}.

2.2.3 2D Electrode Materials

The most widely explored materials for 2D nanostructured-electrode fall under the following three categories. The first one includes carbon-based electrodes, which have been the most extensively investigated since the emergence of graphene, and found most applications in EDLC. Secondly, electrodes made of metal oxides and hydroxides, which have also been widely studied as active materials for pseudocapacitors, will be discussed. Finally, recent developments in transition-metal dichalcogenides (TMDs) including MoS_2 and VS_2 will be overviewed.

2.2.3.1 Carbon Based Electrodes.

Various forms of carbon have been considered for electrode materials in supercapacitors.[99, 100] Moderate specific capacitance together with long cycle life represent the holy-grail for carbon-based electrodes. Currently low conductivity of porous carbon material, despite their high surface area, constitutes a major limitation for supercapacitors with high-power density.[101-102] On the other hand, CNTs offer both high surface area and conductivity, but show high contact resistance at the electrode-current collector and expensive synthesis have hampered their scale up processing for large scale manufacturing. Thus, the emergence of graphene has provided an alternative to overcome the limitations of carbon-based electrodes and lead to new directions in the development and optimization of electrode materials. As a result, graphene is currently the most common material used for 2D material-based electrodes in energy storage devices due to its chemical stability (i.e. resistance to oxidative processes),[99, 103-105] as well as its unique intrinsic electrical (i.e. fast transport of electrons), mechanical and thermal properties.[106] Recently, the capacitance of graphene in its monolayer form was experimentally measured (~21 $\mu F\ cm^{-1}$),[107] with a projected ~500 $F\ g^{-1}$ for an ideal single layer graphene-based EDLC, in which the surface area could be fully utilized. Such an electrode would constitute a record in carbon electrode materials for EDLCs but designing remains a great challenge.

In addition, as discussed by Ruoff and co-workers in one of the first demonstrations of graphene as electrodes for supercapacitors, it eliminates the necessity of using conductive fillers to improve the electrode conductivity.[108] It also offers the possibility to increase the electrode thickness while greatly improving the performance including a higher ratio of electrode material to collector/separator and higher energy densities. Moreover, large surface area of graphene is very attractive for supercapacitor electrode materials.[108-110] The surface area of graphene is predicted to be as high as 2630 m^2 g^{-1} and all the more exciting is the fact that it intrinsically consists of structured, accessible pores and interlayer spaces (i.e. better accessibility for ions).[108, 109] Thin films of graphene electrodes have been obtained by various methods aiming at large scale production, including CVD,[111-113] electrostatic spray deposition,[112] electrophoretic deposition,[18, 112] and ink-jet printing.[78, 112, 114] Nevertheless, to date, chemical approaches to make graphene oxide (GO) are the most cost-effective ton-scale method to produce graphene-based electrode materials. However, despite higher production yield, additional treatments are required to overcome its low conductivity. Among various treatments, chemically modified graphene (CMG) and reduced graphene oxide (rGO) are of particular interest as they offer a scalable and cost-effective chemical approach and produce a material with conductivity close to that of graphene.[99, 108, 115, 116] As a result, rGO has been extensively used as a highly conductive electrode material and the mechanisms of reduction of GO becomes highly important in the development of 2D electrode materials for supercapacitors.

(a) Performance of chemically prepared rGO electrodes: A variety of reducing agents have been considered to restore the graphene network and its conductivity in the GO sheets.[117-120] Hydrazine is the most commonly reported reducing agent for GO reduction. Ruoff and co-workers described the synthesis of CMG by reduction of suspended graphene oxide in water using hydrazine hydrate.[108] The resulting sheets showed a surface area of 705m^2 g^{-1} and provided specific capacitances of 135 and 99 F g^{-1}, respectively, in aqueous and organic electrolytes. Chen and co-workers discussed GO gas-based reduction by hydrazine at room temperature to lower agglomeration in the system.[99, 100] The electrode materials resulting from their protocol were

shown to surpass CMG or CNT-based supercapacitors,[108, 121, 122] with a maximum capacitance ~205 F g^{-1}, energy density of 28.5 Wh kg^{-1} in an aqueous electrolyte solution and ~90% specific capacitance retained after 1200 cycle tests. C-N and C-O bonds, creating numerous hydrophilic polar sites, were present in the material, and seemed to improve the wettability of the electrodes.[99] Despite the seemingly high packing of the layers, the agglomeration was shown to be lower than with other protocols, allowing ions from the electrolyte to penetrate in-between layers and increase the capacitance of the system.

Other reducing agents including hydroquinone[120, 123] and NaBH4[120, 124, 125] have also been used to reduce GO. Interestingly, activated graphene using KOH in GO, another form derived from graphene obtained by chemical activation of exfoliated GO prepared by Ruoff and co-workers, revealed large surface area (3100 m^2 g^{-1}), high specific capacitance (up to ~170 F g^{-1}) and great electrical conductivity.[115] Despite the chemical processes involved in the formation of the activated layers, low oxygen and hydrogen content were found in the final product. Furthermore, ~97% of the capacitance was retained after 10000 cycles.

(b) Performance of rGO electrodes prepared by physical methods: Vacuum low-temperature exfoliation and laser treatments are among the physical methods used for the reduction of GO in energy storage applications. Chen and co-workers have recently demonstrated that graphene flakes obtained as a result of low-temperature vacuum exfoliation demonstrated excellent energy storage performance.[126] The devices were tested in aqueous and organic electrolytes and exhibited specific capacitance of 220 F g^{-1} and 120 F g^{-1}, respectively.[126]

Thermal treatment of GO suspension from 150 – 200 °C has also been shown to produce rGO by removing the oxygen from GO thus enabling high conductivity up to 5230 S m^{-1}.[120] A specific capacitance of 122 F g^{-1} at 5 mA could be achieved after thermal treatment at 200 °C, corresponding to a charge/discharge rate of ~1000 mA g^{-1}. This constitutes an improvement of the specific capacitance of ~ 20% by direct comparison with the performance of a supercapacitor prepared using rGO obtained with hydrazine,[108] and compares well with other standard electrode-materials.[127] The advantage of this approach is its potential for scalable "green" production of carbon-based supercapacitor electrode materials.

On the other hand, laser reduction of GO is also getting substantial attention,[128-131] in part due to the ability to pattern rGO-GO structures with customized geometries in the same piece of GO, in plane or in 3D. For example, Ajayan and co-workers have developed a laser writing technique to directly convert GO to rGO.[128] In their study, the structure of the laser induced rGO was found to be porous, due to the decomposition of functional groups and water during laser treatment. Due to the anisotropic nature of ion mobility and transport distances, the capacitance was found to be highly dependent on the geometry of the patterned structures. The highest area capacitance of 0.51 mF cm^{-2} was obtained for in-plane disc geometry with no electrolyte. Comparatively, an interdigitated rGO supercapacitor with an organic electrolyte and electrode of the same thickness exhibited a mean capacitance density of 0.4 mF cm^{-2}.[130] A 30 to 35% drop in capacitance was found after 10000 cycles, but the same performance could be improved by long exposure to ambient environment or aqueous electrolytes.[128] In contrast, Kaner and co-workers found that the laser-treated GO obtained using a LightScribe CD/DVD optical drive can provide an impressive conductivity (~1740 S m^{-1}).[129] In addition, the nanosheets were found to be well aligned, with outstanding mechanical properties (only 1% change in conductivity after 1000 bending cycles). The formation of rGO-GO interfaces by laser reduction paves the way to in-plane supercapacitors with new configuration of ion percolation for higher performance.

The laser reduction methods also addresses one of the several challenges that greatly impede the performance of the devices, in particular restacking of graphene nanosheets.[103] This phenomenon is caused by van der Waals interaction between successive graphene layers.[103] In fact this is one of many extensive research efforts that have been employed to develop protocols preventing graphene restacking. Curved graphene was also shown to improve the performance of supercapacitors by taking advantage of the maximum intrinsic surface capacitance and surface area.[110] In addition, the formation of rGO-GO interfaces by laser reduction paves the way to in-plane supercapacitors with new configuration of ion percolation for higher performance. As demonstrated by Ajayan and co-workers,[113] the in-plane design fosters ions to interact with all the graphene layers resulting in the maximum utilization of electrochemical surface area.

Given the diversity of the results obtained with GO and reduced GO, a fundamental model describing the electrode polarizability, electrolyte dynamics, possible chemical processes, structural defects in the electrodes and pore characteristics would be of great interest to speed up the material discovery. However, this is a complex problem to model. Recently, Kim and co-workers considered the role of oxidation in molecular dynamics models and demonstrated that the capacitance is highly dependent on the configuration of the oxidation,[116] as it modifies the electrode surface accessibility of the ions. Although limited in the parameters considered for the calculations, the approach shows great promise to catalyse electrode optimizations.

Overall, the initial reports of graphene-based electrodes in electrochemical supercapacitors indicated specific capacitance of 117 F g^{-1} in aqueous H_2SO_4 with operating voltage to 1V for electrode preparation by graphitic oxide exfoliation and by nanodiamond transformation.[132] Specific capacitance of 135 F g^{-1} and voltage up to 1V in aqueous media were obtained with CMG[108] with energy density of about 32 Wh g^{-1}.[132]

2.2.3.2 Metal Oxides and Hydroxides.

Metal oxides like RuO_2, IrO_2, MnO_2, NiO, Co_2O_3, SnO_2, V_2O_5 and MoO_2, are considered as important electrode materials for supercapacitors.[123] Their implementation in the form of 2D electrodes is taking the centre stage of hybrid device development. Deposition methods such as spin coating, anodization, electrodeposition, atomic layer deposition, spray deposition, and sputtering have been employed to deposit smooth thin films with optimal texture and low grain boundary density.[112, 133]

2D MnO_2 (up to 2nm in thickness) has been considered for cathode electrodes. Using soft template methods, Kang and co-workers showed high specific capacitance as high as 774 F g^{-1} up to 10000 cycles.[134] The MnO_2 electrodes were used in aqueous $Ca(NO_3)_2$-SiO_2 gel electrolyte. The electrodes were prepared using a soft template technique. MnO_2 nanosheets were obtained by mixing sodium bis(2-ethylhexyl)sulfosuccinate and water to form a binary lamellar structure, to which $KMnO_4$ is added. The dissolution of $KMnO_4$ occurs only in the aqueous phase of the mixture and the growth of MnO_2 is automatically initiated in the aqueous phase. Scan rates from 2 to 50 mV s^{-1} could be demonstrated. For RuO_2 thin film electrodes, performances up to 730 F g^{-1} were demonstrated.[135, 136]

2.2.3.3 Transition-Metal Dichalcogenides (TMDs).

Layered transition-metal dichalcogenides, in their monolayer forms, have recently taken an important role in material sciences for applications in optoelectronics, nanoelectronics and sensors. However, they have not been actively considered as possible electrode materials for supercapacitors. Although graphene in-plane design has already demonstrated great results, its large scale implementation is hindered by high costs associated with the production of large-area low-defect graphene production. TMDs offer a variety of properties that could overcome the shortcomings of graphene. However, it remains to be seen whether TMDs may have an equivalent impact as graphene for in-plane supercapacitors.

Among TMDs being considered for electrode materials, MoS_2 may be of special interest for EC, as its intrinsic conductivity was calculated to be higher than other similar metal oxides, while its theoretical capacity was predicted to surpass that of graphite.[137, 138] However, to date, the literature related to MoS_2 for EC electrodes is rather limited.[139, 140] Soon and Loh carried out electrochemical impedance spectroscopy to characterize the performance of an arrangement of dense edge-oriented MoS_2 films for micro-supercapacitor and found that the performance is similar to that of CNT electrodes.[139, 140] Other studies with various configuration of MoS_2 lead to medium performance electrodes.[86, 95, 141] More recently, flower-like MoS_2 electrode material developed by Geng and co-workers exhibited a specific capacitance of 168 F g^{-1} (at 1 A g^{-1}, 1M KCl) and retained ~93% capacitance after 3000 cycles.[139]

Among other TMDs with intrinsically high conductivity, VS_2 represents a favorable alternative to graphene; further strengthened by the feasibility of exfoliation of layers after intercalation with NH_3 (Figure 2.5).[142] Numerous tests were carried out on this new material. The conductivity remained constant throughout the 200 bending cycles test and is of great promise for flexible applications. The fabricated in plane device exhibited a specific capacitance ~317 F cm^{-3}, comparable to graphene based electrodes, with a good stability (90% after 1000 cycles).

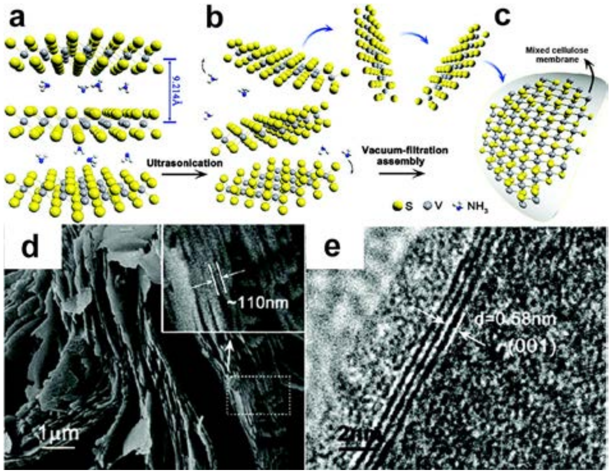

Figure 2.5 VS_2 nanosheets for supercapacitor electrodes. S-V-S multilayers with intercalated NH_3 molecules (a) is used to exfoliate thin layers of VS_2 (b). The transfer is accomplished by vacuum filtration and the layers are transfered on mixed cellulose membranes (c). SEM (d) and HR-TEM (e) images of the multilayer with NH_3. Reproduced with permission from ref. 142. Copyright 2011 American Chemical Society.

2.2.3.4 Transition-Metal Carbides and/or Nitrides (MXenes).

Recently, Gogotsi and co-workers introduced MXenes as a new family of promising 2D supercapacitor electrode materials.[143-146] MXenes consist of highly conductive carbide and carbonitride layers, which surfaces are designed to be hydrophilic and primarily hydroxyl-terminated. High capacitance (over 300 F cm^{-3}) can be achieved by cations (Mg^{2+}, K^+, Na^+, Al^{3+}, NH^{4+}, Ba, Ca, Cs, Li) intercalation, including cations of various charges and sizes. Although ions intercalation is typically used in battery materials for energy storage, the slow diffusion rate hinder the charge/discharge performances. However, processes based on ion adsorption are often used in supercapacitors. In MXene, cation intercalation rates are unusually high, and the process is referred to as the intercalation pseudocapacitance.[147]

MXenes derive from the family of layered hexagonal MAX phases, a group including more than 60 forms of ternary nitrides or carbides, where M represents an early transition metal (e.g. Ti, V, Cr, Nb, etc.), A stands for an A-group element (e.g. Al, Si, Sn, In, etc.), and X represents C and/or N. The synthesis of MXene involves removing the A of MAX compounds by selective etching. While numerous MXenes were predicted theoretically,[148, 149]only about eleven MXenes are tested experimentally to date. Theoretically, it has been demonstrated that the surface termination (hydroxyl, fluorine) can be used to modify some of the MXene properties, such as their conductivity and bandgap.

Among the reported studies, a MXene, $Ti_3C_2T_x$, was obtained by etching Ti_3AlC_2 by hydrofluoric acid (HF) at room temperature.[145] A binder-free $Ti_3C_2T_x$ MXene material with surface area of 98 m^2 g^{-1} was obtained by delamination (single to few layers) and filtration of Ti_3AlC_2. It showed high flexibility and high volumetric capacitance (as high as 350 F cm^{-3}) in aqueous electrolyte NaOH.[143] To date, research towards electrode materials based on MXenes are limited; nevertheless, as a new promising 2D supercapacitor electrode material, much effort needs to be dedicated in this direction.

2.2.4 3D Electrode Materials

3D porous structures of active materials provide large surface area, well-defined pathways to electrolyte access and mechanical stability for efficient supercapacitor electrodes. Generally, 3D electrodes are built either using metal foam as templates or organizing active materials into 3D nanostructures.

2.2.4.1 Metal Foams as 3D Nanostructured Current Collectors.

Metal foams such as nickel foams provide highly porous and conductive substrates for the deposition of active materials including graphene, CNTs, conjugated polymers and metal oxides to build supercapacitor electrodes.[150-155] Compared with carbon based 3D substrates, metal foams have higher electrical conductivity and better mechanical properties but at the cost of larger density and lower specific surface area. 3D Co/Ni oxides with different morphologies were controllably synthesized and deposited on nickel foam substrates.[151] The synthesis involves a co-electrodeposition of bimetallic (Ni, Co) hydroxide precursors on a nickel foam scaffold and a subsequent thermal transformation of the precursors to Ni_xCo_{1-x} oxides. The crystal structure, morphology and electrochemical performance of the 3D Ni_xCo_{1-x} oxides can be readily manipulated by simply varying the Co/Ni molar ratio in the electrodeposition electrolyte. With the increase in the Co/Ni molar ratio, the structure changes from a NiO crystal dominant structure to $NiCo_2O_4$ and finally to a Co_3O_4 dominant structure. The unique 3D network architecture provides large solid/liquid interfacial area and facilitates efficient electron and ion transport. The electrode prepared with $Ni_{0.61}Co_{0.39}$ oxide on Nickel foam showed a specific capacitance of 1523.0 F g^{-1} at 2 A g^{-1} current density and retained 95.30% of its specific capacitance at a current density of 30 A g^{-1} after 1000 cycles. This electrode was used as a positive electrode with activated carbon as a negative electrode to build an asymmetrical supercapacitor and delivered a prominent energy density of 36.46 Wh kg^{-1} at a power density of 142 W kg^{-1}.[151]

Ozkan and co-workers used nickel foams to grow graphene and CNTs followed by a deposition of ruthenium oxide (RuO_2) nanoparticles on CNTs.[150] The hierarchical and porous structures enable efficient access of electrolyte to the active materials (CNT-RuO_2 network layer) and provide a conductive framework to charge transport attributed to the embedded CNTs. The composite had a high energy density of 39.28 Wh kg^{-1} and power density of 128.01 kW kg^{-1} and showed an excellent cycle stability of 106% capacitance retention over 8100 cycles.

Similarly, electrodes were prepared using well-aligned CoO nanowire arrays grown on 3D nickel foams with polypyrrole uniformly immobilized onto nanowire surface to utilize high electrochemical activities of CoO and polypyrrole as well as the short ion diffusion pathway in ordered mesoporous nanowires.[155] Such synergy between materials and structures leads to a high specific capacitance of 2223 F g^{-1}, good rate capability, and good cycle stability (99.8% capacitance retention after 2000 cycles). An asymmetrical supercapacitor device fabricated using the hybrid materials as the positive electrode and activated carbon film as the negative electrode achieved a maximum voltage of 1.8 V, high energy density (~43.5 Wh kg^{-1}) and power density (~5500 W kg^{-1} at 11.8 Wh kg^{-1}), and outstanding cycle stability (~20000 times with 91.5% capacitance retention).

Mn/MnO_2 core-shell 3D porous structures were fabricated from ordered polystyrene sphere templates. Mn was electrically deposited between polystyrene spheres from N-butyl-N-methyl pyrrolidinium TFSI ionic liquid solution of $MnCl_2$. After removing polystyrene template by tetrahydrofuran, the 3D Mn template was anodized in a KCl aqueous solution to produce a Mn/MnO_2 core-shell structure. Such core-shell porous structures contribute several positive factors including larger surface area, high electrical conductivity attributed to Mn and high capacitance of MnO_2 for efficient supercapacitors. Especially, the electrolyte can easily access the active material, leading to high specific capacitance at high scan rate. The optimum specific capacitance of the electrode at 500 mV s^{-1} is 996 F g^{-1}, maintaining 83% of the capacitance measured at 5 mV s^{-1}.[153] Composite supercapacitor electrodes based on metal foams have high electrical conductivity, good mechanical properties, and easy access of electrolyte to active materials, which leads to high specific capacitance and good cycle stability.

2.2.4.2 3D Nanostructures Based on Carbon Materials.

Mesoporous carbon (MC) has been used as promising materials for supercapacitor electrode materials because of their large specific surface area and interconnected pores with tunable size. Since Ryoo and co-workers reported the fabrication of ordered MC from the ordered mesoporous silica molecular sieves as templates,[156, 157] much effort has been devoted to exploring the application of such materials as supercapacitor electrodes. The studies of utilizing MC as electrode materials for EDLCs suggest that the pore size and symmetry have profound effect on the performance by influencing the accessibility of electrolytes. The pore size distribution with best performance ranges from 0.6 to 3 nm depending on different types of electrolytes.[158, 159] While these EDLCs can reach the specific capacitance of 140 F g^{-1} which is much higher than those using commercial carbon, their performance is limited by the relative low electrical conductivity. [160]

Further improvement can be achieved by doping [161] and depositing electrochemically pseudocapactive materials such as metal oxides, [162-164] PANI,[165-169] and their mixtures[170] onto MC templates. For example, nitrogen- and sulfur-codoped 3D cubic ordered MC (KNOMC) materials with controlled dopant content (10.0−4.6 atom % for nitrogen and 0.94 − 0.75 atom % for sulfur) have demonstrated a specific capacitance of 320 F g^{-1} because the incorporated S and N species function as pseudo-active materials.[161] Metal oxides have also been added onto MC to increase the capacitance. For example, MnO_2 nanoparticles were imbedded in the MC through a redox reaction between permanganate ions and carbons.[164] The ordered mesoporous structures were retained through the control of the concentration of permanganate ion. The resulted composite structure showed a specific capacitance of 200 F g^{-1} with decent electrochemical stability and reversibility. Nanostructured PANI has been deposited on various MC substrates through chemical oxidative polymerization and it greatly increased the specific capacitance due to its high capacitance and electrical conductivity.[171] Li and co-workers have deposited PANI needle-like structures on MC and studied the effect of the structure on electrochemical properties.[167] It was found that the composite with 60% PANI deposition has the best performance (517 F g^{-1}), suggesting that a bimodal pore structure with some open pores facilitates the ion diffusion and shorten the charge transfer distance. PANI–CMK-3–MnO_2 ternary nanocomposites were built by co-deposition of conductive PANI and MnO_2 on MC and further improved the specific capacitance to 695 F g^{-1}.[170] In such composite, MnO_2 nanoparticles stabilizes the interaction between the quinoid ring of PANI and the CMK-3–MnO_2, while the PANI nanolayer retards the dissolution of MnO_2 nanoparticles during the charge–discharge process, leading to high cycle stability.

Theoretical studies[172, 173] and experimental investigation[174] of the effect of pore size and distribution on ionic transport properties of porous structures suggest that the coexistence of macropore and mesopore would increase the efficiency of porous carbon as supercapacitor electrodes. Compared with MC, an ordered carbon structure with meso/macro/micropores can achieve a specific capacitance as high as 350 F g^{-1}.[174] Hierarchical carbon structures with a combination of meso/macro/micropores have been produced through various approaches,[175-183] and used as electrode with and without metal oxides.[184, 185] These structures have demonstrated great potential in constructing high performance supercapacitors. Further improvement requires better control of pore size and distribution as well as increased electrical conductivity of porous carbon.

The impact of graphene aerogel structure on the electrochemical performance was systematically investigated by comparing different graphene aerogel structures. Three types of carbohydrates (glucose, β-cyclodextrin, and chitosan) were used as dispersants and reducing agents to fabricate graphene aerogels from GO by a simple hydrothermal route. It was found that different carbohydrates induces different assembling behavior for GO. Glucose produced a highly porous GO network through hydrogen bonding between small glucose molecules and GO sheets (Sample GAGLU). β-cyclodextrin is a macrocyclic oligosaccharide with seven glucopyranose units forming a truncated cone with two hydrophilic rims a hydrophobic cavity. Such structure produced stacked GO blocks containing intertwisted GO (Sample GACD). Chitosan, being a highly charge crystalline polysaccharide, produced densely packed rather than porous GO structures (Sample GACS). Combined with better reducing capacity of glucose, GAGLU has higher specific area, better porous structures and higher electrical conductivity than GACD, and GACS. As a result, GAGLU has the best electrochemical performance among three materials as supercapacitor electrodes.

Similar to MC, high performance composite electrodes have been developed by doping graphene with nitrogen and boron[186] and integrating pseudo-active materials on 3D CNT and graphene structures.[187-199] 3D macroporous electrodes of chemically modified graphene (CMG) were fabricated using polystyrene colloidal particles as a sacrificial template. [187] A thin layer of

MnO_2 was deposited onto the porous electrodes to further improve the capacitance. The porous graphene structure facilitates fast ionic transport within the electrode while preserving decent electrical conductivity. Such combination grants the electrodes excellent electrochemical properties such as high specific capacitance (389 F g^{-1} at 1 A g^{-1}) and 97.7% capacitance retention when the current increases to 35 A g^{-1}. In addition, an asymmetrical supercapacitor assembled using MnO_2/CMG composite electrode and a CMG electrode achieves an energy density of 44 Wh kg^{-1}, a power density of 25 kW kg^{-1}, and excellent cycle life.

As discussed previously, ordered 3D porous structures with controlled pore size and distribution would improve the electrochemical properties. The concept of inherently nanoporous 3D pillared vertically aligned carbon nanotube (VA-CNT)–graphene hybrid architecture with a large surface area has been explored to develop efficient supercapacitors.[200-202] Dai and co-workers prepared a VA-CNT–graphene hybrid by the intercalated growth of VA-CNTs into thermally expanded highly ordered pyrolytic graphite.[201] The resulting VA-CNT–graphene hybridized with a nickel hydroxide coating also demonstrated a high specific capacitance with a notable charging-rate capability, as high as 1065 F g^{-1} (based on the active material) at a current density of 22.1 A g^{-1}. Sun and co-worker have grown carbon nanotubes on graphene sheets through a facile one-pot pyrolysis strategy where cobalt ions and urea were mixed with GO followed by drying and heating the mixture at 900 °C. The length of the carbon nanotubes was tuned by adjusting the amount of precursors. The resulting graphene-CNT composites showed a high specific surface area of 903 m^2 g^{-1} and maximum specific capacitance of 413 F g^{-1}.[202]

As an example of depositing pseudocapative metal oxides on graphene/CNT scaffolds, 3D flower-like β-$Ni(OH)_2$/GO/CNTs composites were prepared via a facile hydrothermal reaction in alkaline solutions. CNTs were introduced to the composite to improve the electrical conductivity. The electrochemical properties of the composites produced at different reaction time were evaluated to understand the effect of composite structures on energy storage efficiency. Hydrothermal reaction converted α-$Ni(OH)_2$ to β-$Ni(OH)_2$ (1h reaction time) and further 3D β-$Ni(OH)_2$ nanoflowers to stacked nanosheets (10h). The electrochemical characterization of three different structures indicates that β-$Ni(OH)_2$ composite prepared through one hour hydrothermal reaction has the best performance with a high specific capacitance of ~1815 F g^{-1} based on $Ni(OH)_2$ (nearly 96% of its theoretical pseudocapacitance) at 2 A g^{-1} and a good cycling performance of ~97% capacitance retention after 2000 cycles at 10 A g^{-1}, attributed to higher stability (vs. α-$Ni(OH)_2$) and more efficient ion diffusion (vs. stacked β-$Ni(OH)_2$).[188]

Zhai and co-workers have incorporated MnO_2 into MWCNT 3D networks as supercapacitor electrodes. More importantly, they have discovered the relationship between MnO_2 migration phenomenon and the scan rates. The structural evolution were examined by studying the structure and electrochemical properties of identical electrodes after 500 CV cycles at various scan rates.[203] By using Electrochemical Quartz Crystal Microbalance (EQCM) to monitor the mass change of the electrode in-situ and SEM to examine the electrodes after CV cycles, MnO_2 was found to “migrate” from the MWCNTs network and “deposit” on the electrode surface upon cycling. The structural change mechanism contains the dissolution of MnO_2 upon reduction, the diffusion of the reduced Mn species from the MWCNT network toward the electrolyte solution, and the deposition of MnO_2 on the electrode surface upon oxidation.[203] The structural change of MnO_2 is highly dependent on the scan rate. For instance, the reduced Mn species have more diffusion time at a lower scan rate, while less reduced species are generated due to the lower associated current density and *vice versa*. A scan rate that might cause the greatest structural evolution of MnO_2 is expected based on this contradictory effect. Figure 2.6a shows the cross section of as-synthesized MWCNT/MnO_2 composites sprayed on a graphite substrate (MCM0) as well as an X-ray line scan spectra of Mn element. The SEM and X-ray line scan spectral data clearly exhibit that MnO_2 nanoflakes are uniformly embedded in the MWCNTs network as the active materials while the MWCNT network serves both as the support for MnO_2 nanoflakes and current collector. In contrast, Figure 2.6 b-f shows the striking changes of electrode structures after 500 CV cycles, and the structural change varies at different scan rates. As a result, a higher specific capacitance could be achieved with a lower scan rate; however, the specific capacitance considerably drops upon cycling due to the dissolution of active material. Therefore, either developing a protective layer as mentioned in the 1D section or manipulating a suitable scan rate that induces the least structural changes while maintaining high specific capacitance is required.

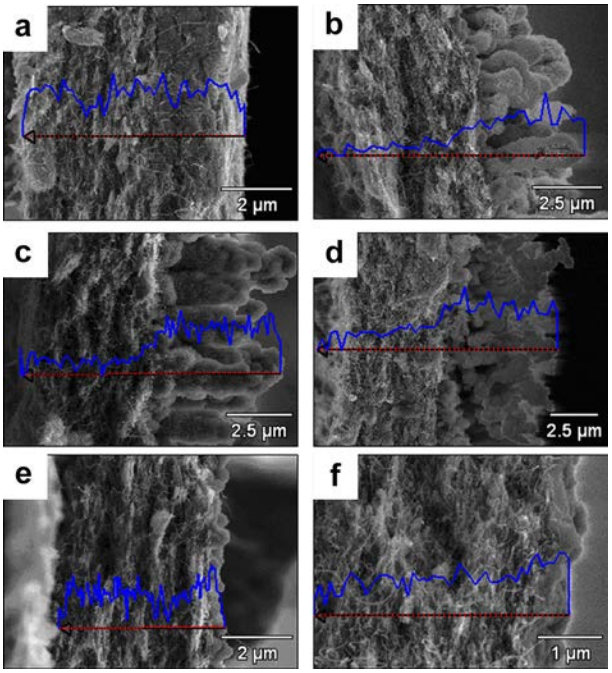

Figure 2.6 Cross-section morphologies and X-ray line scan spectra of Mn element in pristine composites (MCM0), and after 500 cycles at 20 mV s^{-1} (MCM20), 60 mV s^{-1} (MCM60), 100 mV s^{-1} (MCM100), 300 mV s^{-1} (MCM300), and 500 mV s^{-1} (MCM500). (a) MCM0, (b) MCM20, (c) MCM 60, (d) MCM100, (e) MCM300, and (f) MCM500. Reproduced with permission from ref. 203. Copyright 2012 Elsevier.

2.2.4.3 3D Nanostructures Based on Pseudocapacitive Materials.

Different nanostructures of pseudocapacitive materials offer intriguing composition for 3D supercapacitors. Various types of metal oxide nanostructures produced through sol-gel, solvothermal and other approaches have been evaluated electrochemically to understand the impact of their structures on the energy storage properties. NiO nanostructures with three distinct morphologies (flower-like, slice-like and particle-like) were fabricated by a sol-gel method. The BET specific surface area of nanoflower, nanoslice, and nanoparticle NiO was 159, 193, and 233 m^2 g^{-1} and the average pore size was 16.7, 6.3, and 8.8 nm, respectively.[204] With the lowest surface area and largest pore size, the nanoflower NiO nanostructures formed a 3D network, offering the most efficient contact with and transport of the electrolyte. Therefore, this structure granted the best electrochemical properties among three different nanostructures. This study suggests that it is important to facilitate the transport of ions to active materials on the top of large surface area.

3D hierarchical Co_3O_4 twin-spheres with an urchin-like structure were produced by a solvothermal synthesis of cobalt carbonate hydroxide hydrate followed by calcination. The morphology of the precursors evolved from nanorods to sheaf-like bundles, to flower-like structures, to dumbbell-like particles, and eventually to twin-spheres through a three-stage self-assembly of nanorods. Such structure provided larger surface area and better accessibility of electrolytes compared to nanorods and nanodiscs of Co_3O_4. The specific capacitances of the urchin-like structure evaluated from the discharge curves were 781, 754, 700, 670, and 611 F g^{-1} at current densities of 0.5, 1, 2, 4, and 8 A g^{-1}, respectively.[205] Similar urchin-like MnO_2 nanostructures were also produced through a hydrothermal method. It was found that the phase of the products transformed from α-MnO_2 to ε-MnO_2 when Al^{3+} was substituted by Fe^{3+} in the solution. At the same time, the morphology of the product was changed from urchin-like clusters to 3D clew-like structures.[206] The 3D clew-like ε-MnO_2 showed a specific capacitance of 120 F g^{-1} at the scan rate of 5 mV s^{-1}.

Current research in this field focuses on the structural control of the products rather than achieving good electrochemical properties. These nanostructures, although presents interesting shapes, have not demonstrated superior performance compared with pseudocapacitive materials deposited on porous carbons and metal foams. In order to advance the application of metal oxide nanostructures in supercapacitors, it is necessary to improve the electrical conductivity, electrolyte accessibility and cycle stability of the materials.

2.3 Device Configurations

Supercapacitors are generally assembled by sandwiching two electrodes together with a porous separator (ionic conductive but electronic insulated) in between. If the two electrodes are identical, the as-fabricated devices are called symmetric supercapacitors; if the two electrodes are made from different electrode materials, the as-fabricated devices are called asymmetric supercapacitors.

In water-based electrolytes, symmetric supercapacitors are normally confined to an operational potential of no more than 1 V due to the decomposition of water when applied voltage larger than 1.23 V. However, asymmetric supercapacitors are able to work in water-based electrolytes with an operational potential more than 2 V. This is due to both the anode and cathode in one asymmetrical device can utilize different voltage interval ranging from – 1V to 1V. It is essential to realize extended operational potential because the energy density is linear to the square of cell potential. In organic electrolytes, because they can endure a much broader potential that were applied to them, even symmetric supercapacitors can achieve an operational potential up to 3V. However, the downsides of organic electrolytes are their toxicity, high cost, and poor ionic conductivity. Symmetric supercapacitors will be illustrated in Chapters 4 and 5 and asymmetric supercapacitors will be covered in Chapters 6 and 7.

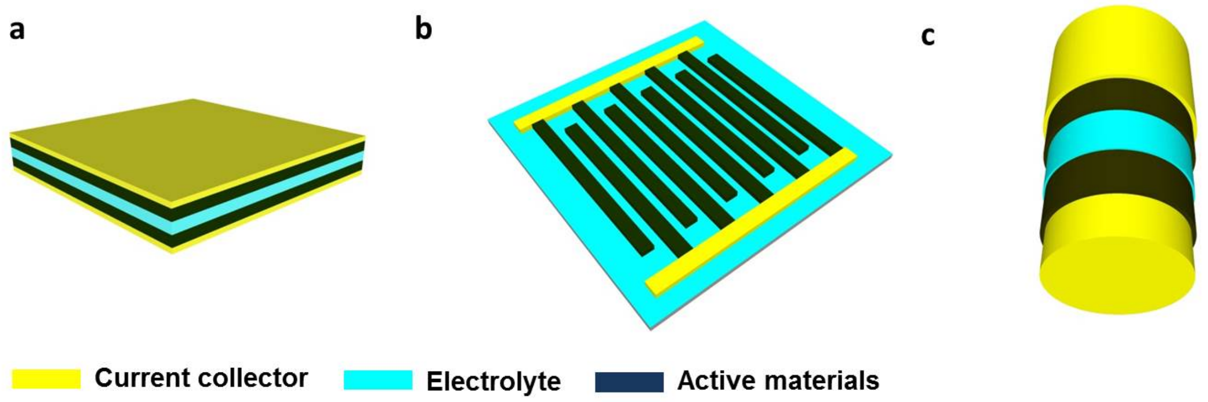

Figure 2.7 Schematic of recent device configurations including (a) sandwich-type, (b) in-plane type, and (c) cable-type.

In addition to traditional sandwich-type supercapacitors (Figure 2.7 a), there are several emerging device architectures that have been intensively investigated in recent years. One of them is in-plane design (Figure 2.7b). In an in-plane supercapacitor design, both electrodes are created on the same substrate. The in-plane design is especially beneficial for graphene based device because it fosters ions to interact with all the graphene layers, resulting in the maximum utilization of electrochemical surface area. Another promising device architecture is the cable-type supercapacitor design (Figure 2.7c). A prototype design is a wire shaped inner electrode wrapped by a foil shaped outer electrode with a separator in between. In such design, devices might have better flexibility/bendability, portability, and lightweight compared to sandwich-type devices. Sandwich-type supercapacitors will be illustrated in Chapters 4 and 6 and cable-type supercapacitors will be covered in Chapters 5 and 7.

2.4 References

1. H. Gleiter, *Acta Mater.*, 2000, **48**, 1-29.

2. V. Pokropivny and V. Skorokhod, *Mater. Sci. Eng. C*, 2007, **27**, 990-993.

3. J. N. Tiwari, R. N. Tiwari and K. S. Kim, *Prog. Mater. Sci.*, 2012, **57**, 724-803.

4. J. Gamby, P. Taberna, P. Simon, J. Fauvarque and M. Chesneau, *J. Power Sources*, 2001, **101**, 109-116.

5. E. Frackowiak, *Phys. Chem. Chem. Phys.*, 2007, **9**, 1774-1785.

6. D.-W. Wang, F. Li, Z.-G. Chen, G. Q. Lu and H.-M. Cheng, *Chem. Mater.*, 2008, **20**, 7195-7200.

7. S. Prabaharan, R. Vimala and Z. Zainal, *J. Power Sources*, 2006, **161**, 730-736.

8. L. Hu, W. Wang, J. Tu, J. Hou, H. Zhu and S. Jiao, *J. Mater. Chem. A*, 2013, **1**, 5136-5141.

9. M. Xue, Z. Xie, L. Zhang, X. Ma, X. Wu, Y. Guo, W. Song, Z. Li and T. Cao, *Nanoscale*, 2011, **3**, 2703-2708.

10. M. P. Yeager, D. Su, N. S. Marinković and X. Teng, *J. Electrochem. Soc.*, 2012, **159**, A1598-A1603.

11. Y.-Z. Zheng, H.-Y. Ding and M.-L. Zhang, *Mater. Res. Bull.*, 2009, **44**, 403-407.

12. Y. Chen, Z. Yu, Y. Chen, L. Luo and X. Wang, Materials for Renewable Energy & Environment (ICMREE), 2011 International Conference on, Shanghai, 2011.

13. X. Du, C. Wang, M. Chen, Y. Jiao and J. Wang, *J. Phys. Chem. C*, 2009, **113**, 2643-2646.

14. C. Liu, F. Li, L. P. Ma and H. M. Cheng, *Adv. Mater.*, 2010, **22**, E28-E62.

15. B. E. Conway, *Electrochemical Supercapacitors: Scientific Fundamentals and Technological Applications*, Springer, New York, 1999.

16. L. L. Zhang and X. Zhao, *Chem. Soc. Rev.*, 2009, **38**, 2520-2531.

17. C. Portet, G. Yushin and Y. Gogotsi, *Carbon*, 2007, **45**, 2511-2518.

18. D. Pech, M. Brunet, H. Durou, P. Huang, V. Mochalin, Y. Gogotsi, P.-L. Taberna and P. Simon, *Nat. Nanotechnol.*, 2010, **5**, 651-654.

19. X. Lang, A. Hirata, T. Fujita and M. Chen, *Nat. Nanotechnol.*, 2011, **6**, 232-236.

20. J. T. Mefford, W. G. Hardin, S. Dai, K. P. Johnston and K. J. Stevenson, *Nat. Mater.*, 2014, **13**, 726-732.

21. X. Lai, J. E. Halpert and D. Wang, *Energy Environ. Sci.*, 2012, **5**, 5604-5618.

22. Z. Zhong, Y.-d. Yin, B. Gates and Y. Xia, *Adv. Mater.*, 2000, **12**, 206-209.

23. B. You, J. Yang, Y. Sun and Q. Su, *Chem. Commun.*, 2011, **47**, 12364-12366.

24. X. Tang, Z.-h. Liu, C. Zhang, Z. Yang and Z. Wang, *J. Power Sources*, 2009, **193**, 939-943.

25. S.-W. Bian, Y.-P. Zhao and C.-Y. Xian, *Mater. Lett.*, 2013, **111**, 75-77.

26. C.-Y. Cao, W. Guo, Z.-M. Cui, W.-G. Song and W. Cai, *J. Mater. Chem.*, 2011, **21**, 3204-3209.

27. W. Yu, X. Jiang, S. Ding and B. Q. Li, *J. Power Sources*, 2014, **256**, 440-448.

28. T. Zhu, Z. Wang, S. Ding, J. S. Chen and X. W. D. Lou, *RSC Adv.*, 2011, **1**, 397-400.

29. Z. Yang, F. Xu, W. Zhang, Z. Mei, B. Pei and X. Zhu, *J. Power Sources*, 2014, **246**, 24-31.

30. Y. Wang, A. Pan, Q. Zhu, Z. Nie, Y. Zhang, Y. Tang, S. Liang and G. Cao, *J. Power Sources*, 2014, **272**, 107-112.

31. X. Lai, J. Li, B. A. Korgel, Z. Dong, Z. Li, F. Su, J. Du and D. Wang, *Angew. Chem. Int. Ed.*, 2011, **50**, 2738-2741.

32. Z. Lei, Z. Chen and X. Zhao, *J. Phys. Chem. C*, 2010, **114**, 19867-19874.

33. Z. Lei, J. Zhang and X. Zhao, *J. Mater. Chem.*, 2012, **22**, 153-160.

34. L. Fan, L. Tang, H. Gong, Z. Yao and R. Guo, *J. Mater. Chem.*, 2012, **22**, 16376-16381.

35. Z.-C. Yang, C.-H. Tang, H. Gong, X. Li and J. Wang, *J. Power Sources*, 2013, **240**, 713-720.

36. Y. Xia, P. Yang, Y. Sun, Y. Wu, B. Mayers, B. Gates, Y. Yin, F. Kim and H. Yan, *Adv. Mater.*, 2003, **15**, 353-389.

37. H. Wang, Q. Gao and L. Jiang, *Small*, 2011, **7**, 2454-2459.

38. J. Chen, B. J. Wiley and Y. Xia, *Langmuir*, 2007, **23**, 4120-4129.

39. X. Lu, Y. Zeng, M. Yu, T. Zhai, C. Liang, S. Xie, M. S. Balogun and Y. Tong, *Adv. Mater.*, 2014, **26**, 3148-3155.

40. G.-Y. Zhao and H.-L. Li, *Micropor. Mesopor. Mater.*, 2008, **110**, 590-594.

41. K. Wang, J. Huang and Z. Wei, *J. Phys. Chem. C*, 2010, **114**, 8062-8067.

42. M. R. Tarasevich and B. N. Efremov, in *Electrodes of Conductive Metallic Oxides Part A*, ed. S.Trasatti, Elsevier, USA, 1982, p. 227.

43. T. Y. Wei, C. H. Chen, H. C. Chien, S. Y. Lu and C. C. Hu, *Adv. Mater.*, 2010, **22**, 347-351.

44. G. Q. Zhang, H. B. Wu, H. E. Hoster, M. B. Chan-Park and X. W. D. Lou, *Energy Environ. Sci.*, 2012, **5**, 9453-9456.

45. H. Xia, J. Feng, H. Wang, M. O. Lai and L. Lu, *J. Power Sources*, 2010, **195**, 4410-4413.

46. C.-C. Hu, K.-H. Chang, M.-C. Lin and Y.-T. Wu, *Nano Lett.*, 2006, **6**, 2690-2695.

47. R. Liu, S. I. Cho and S. B. Lee, *Nanotechnology*, 2008, **19**, 215710.

48. S. Talapatra, S. Kar, S. Pal, R. Vajtai, L. Ci, P. Victor, M. Shaijumon, S. Kaur, O. Nalamasu and P. Ajayan, *Nat. Nanotechnol.*, 2006, **1**, 112-116.

49. D. N. Futaba, K. Hata, T. Yamada, T. Hiraoka, Y. Hayamizu, Y. Kakudate, O. Tanaike, H. Hatori, M. Yumura and S. Iijima, *Nat. Mater.*, 2006, **5**, 987-994.

50. B. Kim, H. Chung and W. Kim, *J. Phys. Chem. C*, 2010, **114**, 15223-15227.

51. C. R. Martin, *Science*, 1994, **266**, 1961-1966.

52. M. P. Zach, K. H. Ng and R. M. Penner, *Science*, 2000, **290**, 2120-2123.

53. E. Menke, M. Thompson, C. Xiang, L. Yang and R. Penner, *Nat. Mater.*, 2006, **5**, 914-919.

54. P.-L. Taberna, S. Mitra, P. Poizot, P. Simon and J.-M. Tarascon, *Nat. Mater.*, 2006, **5**, 567-573.

55. Y. Sun, B. Gates, B. Mayers and Y. Xia, *Nano Lett.*, 2002, **2**, 165-168.

56. Y. Sun, Y. Yin, B. T. Mayers, T. Herricks and Y. Xia, *Chem. Mater.*, 2002, **14**, 4736-4745.

57. S. Vaddiraju, H. Chandrasekaran and M. K. Sunkara, *J. Am. Chem. Soc.*, 2003, **125**, 10792-10793.

58. H. Choi and S.-H. Park, *J. Am. Chem. Soc.*, 2004, **126**, 6248-6249.

59. J. Zhou, N. S. Xu, S. Z. Deng, J. Chen, J. C. She and Z. L. Wang, *Adv. Mater.*, 2003, **15**, 1835-1840.

60. N. Cordente, M. Respaud, F. Senocq, M.-J. Casanove, C. Amiens and B. Chaudret, *Nano Lett.*, 2001, **1**, 565-568.

61. C. Cheng, R. K. Gonela, Q. Gu and D. T. Haynie, *Nano Lett.*, 2005, **5**, 175-178.

62. Y. Lei, B. Daffos, P.-L. Taberna, P. Simon and F. Favier, *Electrochim. Acta*, 2010, **55**, 7454-7459.

63. Z. Su, C. Yang, B. Xie, Z. Lin, Z. Zhang, J. Liu, B. Li, F. Kang and C. Wong, *Energy Environ. Sci.*, 2014, 2652-2659.

64. J. YoungáKim, *RSC Adv.*, 2012, **2**, 8281-8285.

65. W. Yan, J. Y. Kim, W. Xing, K. C. Donavan, T. Ayvazian and R. M. Penner, *Chem. Mater.*, 2012, **24**, 2382-2390.

66. D. Chao, X. Xia, C. Zhu, J. Wang, J. Liu, J. Lin, Z. Shen and H. J. Fan, *Nanoscale*, 2014, **6**, 5691-5697.

67. Q. Li, Z.-L. Wang, G.-R. Li, R. Guo, L.-X. Ding and Y.-X. Tong, *Nano Lett.*, 2012, **12**, 3803-3807.

68. L. Bao, J. Zang and X. Li, *Nano Lett.*, 2011, **11**, 1215-1220.

69. P. Yang, X. Xiao, Y. Li, Y. Ding, P. Qiang, X. Tan, W. Mai, Z. Lin, W. Wu, T. Li, H. Jin, P. Liu, J. Zhou, C. P. Wong and Z. L. Wang, *ACS Nano*, 2013, **7**, 2617-2626.

70. X. Sun, Q. Li, Y. Lü and Y. Mao, *Chem. Commun.*, 2013, **49**, 4456-4458.

71. A. Sumboja, X. Wang, J. Yan and P. S. Lee, *Electrochim. Acta*, 2012, **65**, 190-195.

72. G.-R. Li, Z.-L. Wang, F.-L. Zheng, Y.-N. Ou and Y.-X. Tong, *J. Mater. Chem.*, 2011, **21**, 4217-4221.

73. J. Liu, C. Cheng, W. Zhou, H. Li and H. J. Fan, *Chem. Commun.*, 2011, **47**, 3436-3438.

74. J. Yan, E. Khoo, A. Sumboja and P. S. Lee, *ACS Nano*, 2010, **4**, 4247-4255.

75. J. Bae, M. K. Song, Y. J. Park, J. M. Kim, M. Liu and Z. L. Wang, *Angew. Chem. Int. Ed.*, 2011, **50**, 1683-1687.

76. R. K. Sharma, A. Karakoti, S. Seal and L. Zhai, *J. Power Sources*, 2010, **195**, 1256-1262.

77. R. K. Sharma and L. Zhai, *Electrochim. Acta*, 2009, **54**, 7148-7155.

78. Q. Li, J. Liu, J. Zou, A. Chunder, Y. Chen and L. Zhai, *J. Power Sources*, 2011, **196**, 565-572.

79. A. L. M. Reddy, M. M. Shaijumon, S. R. Gowda and P. M. Ajayan, *Nano Lett.*, 2009, **9**, 1002-1006.

80. A. L. M. Reddy, M. M. Shaijumon, S. R. Gowda and P. M. Ajayan, *J. Phys. Chem. C*, 2009, **114**, 658-663.

81. J. Liu, J. Jiang, C. Cheng, H. Li, J. Zhang, H. Gong and H. J. Fan, *Adv. Mater.*, 2011, **23**, 2076-2081.

82. C. Guan, J. Liu, C. Cheng, H. Li, X. Li, W. Zhou, H. Zhang and H. J. Fan, *Energy Environ. Sci.*, 2011, **4**, 4496-4499.

83. X. Xia, J. Tu, Y. Zhang, X. Wang, C. Gu, X.-b. Zhao and H. J. Fan, *ACS Nano*, 2012, **6**, 5531-5538.

84. C. Guan, X. Xia, N. Meng, Z. Zeng, X. Cao, C. Soci, H. Zhang and H. J. Fan, *Energy Environ. Sci.*, 2012, **5**, 9085-9090.

85. X. Xia, D. Chao, Z. Fan, C. Guan, X. Cao, H. Zhang and H. J. Fan, *Nano Lett.*, 2014, **14**, 1651-1658.

86. L. Huang, D. Chen, Y. Ding, S. Feng, Z. L. Wang and M. Liu, *Nano Lett.*, 2013, **13**, 3135-3139.

87. Q. Qu, Y. Zhu, X. Gao and Y. Wu, *Adv. Energy Mater.*, 2012, **2**, 950-955.

88. Q. Li, J. M. Anderson, Y. Chen and L. Zhai, *Electrochim. Acta*, 2012, **59**, 548-557.

89. G. Binotto, D. Larcher, A. Prakash, R. Herrera Urbina, M. Hegde and J.-M. Tarascon, *Chem. Mater.*, 2007, **19**, 3032-3040.

90. G. A. Snook, P. Kao and A. S. Best, *J. Power Sources*, 2011, **196**, 1-12.

91. R. Liu and S. B. Lee, *J. Am. Chem. Soc.*, 2008, **130**, 2942-2943.

92. J. Duay, E. Gillette, R. Liu and S. B. Lee, *Phys. Chem. Chem. Phys.*, 2012, **14**, 3329-3337.

93. X. Xia, D. Chao, X. Qi, Q. Xiong, Y. Zhang, J. Tu, H. Zhang and H. J. Fan, *Nano Lett.*, 2013, **13**, 4562-4568.

94. J.-G. Wang, Y. Yang, Z.-h. Huang and F. Kang, *Electrochim. Acta*, 2014, **130**, 642-649.

95. W. Yao, H. Zhou and Y. Lu, *J. Power Sources*, 2013, **241**, 359-366.

96. L. Mai, F. Dong, X. Xu, Y. Luo, Q. An, Y. Zhao, J. Pan and J. Yang, *Nano Lett.*, 2013, **13**, 740-745.

97. H. Zhang, G. Cao, Z. Wang, Y. Yang, Z. Shi and Z. Gu, *Nano Lett.*, 2008, **8**, 2664-2668.

98. R. Liu, J. Duay and S. B. Lee, *ACS Nano*, 2010, **4**, 4299-4307.

99. Y. Wang, Z. Shi, Y. Huang, Y. Ma, C. Wang, M. Chen and Y. Chen, *J. Phys. Chem. C*, 2009, **113**, 13103-13107.

100. D. Chen, L. Tang and J. Li, *Chem. Soc. Rev.*, 2010, **39**, 3157-3180.

101. Y. Huang, J. Liang and Y. Chen, *Small*, 2012, **8**, 1805-1834.

102. M. M. Shaijumon, F. S. Ou, L. Ci and P. M. Ajayan, *Chem. Commun.*, 2008, 2373-2375.

103. X. Yang, J. Zhu, L. Qiu and D. Li, *Adv. Mater.*, 2011, **23**, 2833-2838.

104. H. Wang, Y. Liang, T. Mirfakhrai, Z. Chen, H. Casalongue and H. Dai, *Nano Res.*, 2011, **4**, 729-736.

105. K. S. Novoselov, V. I. Falko, L. Colombo, P. R. Gellert, M. G. Schwab and K. Kim, *Nature*, 2012, **490**, 192-200.

106. S. Stankovich, D. A. Dikin, G. H. B. Dommett, K. M. Kohlhaas, E. J. Zimney, E. A. Stach, R. D. Piner, S. T. Nguyen and R. S. Ruoff, *Nature*, 2006, **442**, 282-286.

107. J. Xia, F. Chen, J. Li and N. Tao, *Nat. Nanotechnol.*, 2009, **4**, 505-509.

108. M. D. Stoller, S. Park, Y. Zhu, J. An and R. S. Ruoff, *Nano Lett.*, 2008, **8**, 3498-3502.

109. Q. Qu, S. Yang and X. Feng, *Adv. Mater.*, 2011, **23**, 5574-5580.

110. C. Liu, Z. Yu, D. Neff, A. Zhamu and B. Z. Jang, *Nano Lett.*, 2010, **10**, 4863-4868.

111. J. R. Miller, R. A. Outlaw and B. C. Holloway, *Science*, 2010, **329**, 1637-1639.

112. M. Beidaghi and Y. Gogotsi, *Energy Environ. Sci.*, 2014, **7**, 867-884.

113. J. J. Yoo, K. Balakrishnan, J. Huang, V. Meunier, B. G. Sumpter, A. Srivastava, M. Conway, A. L. Mohana Reddy, J. Yu, R. Vajtai and P. M. Ajayan, *Nano Lett.*, 2011, **11**, 1423-1427.

114. M. Kaempgen, C. K. Chan, J. Ma, Y. Cui and G. Gruner, *Nano Lett.*, 2009, **9**, 1872-1876.

115. Y. Zhu, S. Murali, M. D. Stoller, K. J. Ganesh, W. Cai, P. J. Ferreira, A. Pirkle, R. M. Wallace, K. A. Cychosz, M. Thommes, D. Su, E. A. Stach and R. S. Ruoff, *Science*, 2011, **332**, 1537-1541.

116. A. D. DeYoung, S.-W. Park, N. R. Dhumal, Y. Shim, Y. Jung and H. J. Kim, *J. Phys. Chem. C*, 2014, **118**, 18472-18480.

117. S. Stankovich, D. A. Dikin, R. D. Piner, K. A. Kohlhaas, A. Kleinhammes, Y. Jia, Y. Wu, S. T. Nguyen and R. S. Ruoff, *Carbon*, 2007, **45**, 1558-1565.

118. S. Park, J. An, I. Jung, R. D. Piner, S. J. An, X. Li, A. Velamakanni and R. S. Ruoff, *Nano Lett.*, 2009, **9**, 1593-1597.

119. V. C. Tung, M. J. Allen, Y. Yang and R. B. Kaner, *Nat. Nanotechnol.*, 2009, **4**, 25-29.

120. Y. Zhu, M. D. Stoller, W. Cai, A. Velamakanni, R. D. Piner, D. Chen and R. S. Ruoff, *ACS Nano*, 2010, **4**, 1227-1233.

121. C. Niu, E. K. Sichel, R. Hoch, D. Moy and H. Tennent, *Appl. Phys. Lett.*, 1997, **70**, 1480-1482.

122. C. Du, J. Yeh and N. Pan, *Nanotechnology*, 2005, **16**, 350.

123. G. Wang, L. Zhang and J. Zhang, *Chem. Soc. Rev.*, 2012, **41**, 797-828.

124. H.-J. Shin, K. K. Kim, A. Benayad, S.-M. Yoon, H. K. Park, I.-S. Jung, M. H. Jin, H.-K. Jeong, J. M. Kim, J.-Y. Choi and Y. H. Lee, *Adv. Funct. Mater.*, 2009, **19**, 1987-1992.

125. Y. Si and E. T. Samulski, *Nano Lett.*, 2008, **8**, 1679-1682.

126. W. Lv, D.-M. Tang, Y.-B. He, C.-H. You, Z.-Q. Shi, X.-C. Chen, C.-M. Chen, P.-X. Hou, C. Liu and Q.-H. Yang, *ACS Nano*, 2009, **3**, 3730-3736.

127. A. Burke, *Electrochim. Acta*, 2007, **53**, 1083-1091.

128. W. Gao, N. Singh, L. Song, Z. Liu, A. L. M. Reddy, L. Ci, R. Vajtai, Q. Zhang, B. Wei and P. M. Ajayan, *Nat. Nanotechnol.*, 2011, **6**, 496-500.

129. M. F. El-Kady, V. Strong, S. Dubin and R. B. Kaner, *Science*, 2012, **335**, 1326-1330.

130. Z. Wei, D. Wang, S. Kim, S.-Y. Kim, Y. Hu, M. K. Yakes, A. R. Laracuente, Z. Dai, S. R. Marder, C. Berger, W. P. King, W. A. de Heer, P. E. Sheehan and E. Riedo, *Science*, 2010, **328**, 1373-1376.

131. Y. Zhang, L. Guo, S. Wei, Y. He, H. Xia, Q. Chen, H.-B. Sun and F.-S. Xiao, *Nano Today*, 2010, **5**, 15-20.

132. S. R. C. Vivekchand, C. S. Rout, K. S. Subrahmanyam, A. Govindaraj and C. N. R. Rao, *J. Chem. Sci.*, 2008, **120**, 9-13.

133. C. D. Lokhande, D. P. Dubal and O.-S. Joo, *Curr. Appl. Phys.*, 2011, **11**, 255-270.

134. S. Shi, C. Xu, C. Yang, Y. Chen, J. Liu and F. Kang, *Sci. Rep.*, 2013, **3**, 2598.

135. J. P. Zheng, P. J. Cygan and T. R. Jow, *J. Electrochem. Soc.*, 1995, **142**, 2699-2703.

136. T. P. Gujar, V. R. Shinde, C. D. Lokhande, W.-Y. Kim, K.-D. Jung and O.-S. Joo, *Electrochem. Commun.*, 2007, **9**, 504-510.

137. L. Cao, S. Yang, W. Gao, Z. Liu, Y. Gong, L. Ma, G. Shi, S. Lei, Y. Zhang, S. Zhang, R. Vajtai and P. M. Ajayan, *Small*, 2013, **9**, 2905-2910.

138. B. Lei, G. R. Li and X. P. Gao, *J. Mater. Chem. A*, 2014, **2**, 3919-3925.

139. X. Wang, J. Ding, S. Yao, X. Wu, Q. Feng, Z. Wang and B. Geng, *J. Mater. Chem. A*, 2014, **2**, 15958-15963.

140. J. M. Soon and K. P. Loh, *Electrochem. Solid-State Lett.*, 2007, **10**, A250-A254.

141. K. Krishnamoorthy, G. K. Veerasubramani, S. Radhakrishnan and S. J. Kim, *Mater. Res. Bull.*, 2014, **50**, 499-502.

142. J. Feng, X. Sun, C. Wu, L. Peng, C. Lin, S. Hu, J. Yang and Y. Xie, *J. Am. Chem. Soc.*, 2011, **133**, 17832-17838.

143. M. R. Lukatskaya, O. Mashtalir, C. E. Ren, Y. Dall'Agnese, P. Rozier, P. L. Taberna, M. Naguib, P. Simon, M. W. Barsoum and Y. Gogotsi, *Science*, 2013, **341**, 1502-1505.

144. M. D. Levi, M. R. Lukatskaya, S. Sigalov, M. Beidaghi, N. Shpigel, L. Daikhin, D. Aurbach, M. W. Barsoum and Y. Gogotsi, *Adv. Energy Mater.*, 2014, DOI: 10.1002/aenm.201400815.

145. M. Naguib, M. Kurtoglu, V. Presser, J. Lu, J. Niu, M. Heon, L. Hultman, Y. Gogotsi and M. W. Barsoum, *Adv. Mater.*, 2011, **23**, 4248-4253.

146. M. Naguib, V. N. Mochalin, M. W. Barsoum and Y. Gogotsi, *Adv. Mater.*, 2014, **26**, 992-1005.

147. V. Augustyn, J. Come, M. A. Lowe, J. W. Kim, P.-L. Taberna, S. H. Tolbert, H. D. Abruña, P. Simon and B. Dunn, *Nat. Mater.*, 2013, **12**, 518-522.

148. M. Kurtoglu, M. Naguib, Y. Gogotsi and M. W. Barsoum, *MRS Commun.*, 2012, **2**, 133-137.

149. M. Khazaei, M. Arai, T. Sasaki, C. Y. Chung, N. S. Venkataramanan, M. Estili, Y. Sakka and Y. Kawazoe, *Adv. Funct. Mater.*, 2013, **23**, 2185-2192.

150. W. Wang, S. Guo, I. Lee, K. Ahmed, J. Zhong, Z. Favors, F. Zaera, M. Ozkan and C. S. Ozkan, *Sci. Rep.*, 2014, **4**, 4452.

151. Y.-M. Wang, X. Zhang, C.-Y. Guo, Y.-Q. Zhao, C.-L. Xu and H.-L. Li, *J. Mater. Chem. A*, 2013, **1**, 13290-13300.

152. T. Zhai, F. Wang, M. Yu, S. Xie, C. Liang, C. Li, F. Xiao, R. Tang, Q. Wu, X. Lu and Y. Tong, *Nanoscale*, 2013, **5**, 6790-6796.

153. M.-J. Deng, P.-J. Ho, C.-Z. Song, S.-A. Chen, J.-F. Lee, J.-M. Chen and K.-T. Lu, *Energy Environ. Sci.*, 2013, **6**, 2178-2185.

154. X. H. Xia, J. P. Tu, Y. Q. Zhang, Y. J. Mai, X. L. Wang, C. D. Gu and X. B. Zhao, *J. Phys. Chem. C*, 2011, **115**, 22662-22668.

155. C. Zhou, Y. Zhang, Y. Li and J. Liu, *Nano Lett.*, 2013, **13**, 2078-2085.

156. S. Jun, S. H. Joo, R. Ryoo, M. Kruk, M. Jaroniec, Z. Liu, T. Ohsuna and O. Terasaki, *J. Am. Chem. Soc.*, 2000, **122**, 10712-10713.

157. R. Ryoo, S. H. Joo, M. Kruk and M. Jaroniec, *Adv. Mater.*, 2001, **13**, 677-681.

158. H. Hu, Z. Zhao, W. Wan, Y. Gogotsi and J. Qiu, *Adv. Mater.*, 2013, **25**, 2219-2223.

159. W. Xing, S. Z. Qiao, R. G. Ding, F. Li, G. Q. Lu, Z. F. Yan and H. M. Cheng, *Carbon*, 2006, **44**, 216-224.

160. M. Inagaki, H. Konno and O. Tanaike, *J. Power Sources*, 2010, **195**, 7880-7903.

161. D. Zhang, L. Zheng, Y. Ma, L. Lei, Q. Li, Y. Li, H. Luo, H. Feng and Y. Hao, *ACS Appl. Mater. Interfaces*, 2014, **6**, 2657-2665.

162. L. Wang, Y. Zheng, S. Chen, Y. Ye, F. Xu, H. Tan, Z. Li, H. Hou and Y. Song, *Electrochim. Acta*, 2014, **135**, 380-387.

163. H. Jiang, J. Ma and C. Li, *Adv. Mater.*, 2012, **24**, 4197-4202.

164. X. Dong, W. Shen, J. Gu, L. Xiong, Y. Zhu, H. Li and J. Shi, *J. Phys. Chem. B*, 2006, **110**, 6015-6019.

165. Y. Yan, Q. Cheng, G. Wang and C. Li, *J. Power Sources*, 2011, **196**, 7835-7840.

166. Y. G. Wang, H. Q. Li and Y. Y. Xia, *Adv. Mater.*, 2006, **18**, 2619-2623.

167. Y. Yan, Q. Cheng, Z. Zhu, V. Pavlinek, P. Saha and C. Li, *J. Power Sources*, 2013, **240**, 544-550.

168. Z. Lei, X. Sun, H. Wang, Z. Liu and X. S. Zhao, *ACS Appl. Mater. Interfaces*, 2013, **5**, 7501-7508.

169. W.-X. Liu, N. Liu, H.-H. Song and X.-H. Chen, *Carbon*, 2011, **49**, 4610.

170. Y. Yan, Q. Cheng, V. Pavlinek, P. Saha and C. Li, *Electrochim. Acta*, 2012, **71**, 27-32.

171. D. Li, J. Huang and R. B. Kaner, *Accounts. Chem. Res.*, 2008, **42**, 135-145.

172. H.-K. Song, Y.-H. Jung, K.-H. Lee and L. H. Dao, *Electrochim. Acta*, 1999, **44**, 3513-3519.

173. G.-J. Lee and S.-I. Pyun, *Langmuir*, 2006, **22**, 10659-10665.

174. H. Yamada, H. Nakamura, F. Nakahara, I. Moriguchi and T. Kudo, *J. Phys. Chem. C*, 2006, **111**, 227-233.

175. A. J. Amali, J.-K. Sun and Q. Xu, *Chem. Commun.*, 2014, **50**, 1519-1522.

176. S. Kubo, R. J. White, K. Tauer and M.-M. Titirici, *Chem. Mater.*, 2013, **25**, 4781-4790.

177. Q. Long, W. Chen, H. Xu, X. Xiong, Y. Jiang, F. Zou, X. Hu, Y. Xin, Z. Zhang and Y. Huang, *Energy Environ. Sci.*, 2013, **6**, 2497-2504.

178. M. Oschatz, L. Borchardt, K. Pinkert, S. Thieme, M. R. Lohe, C. Hoffmann, M. Benusch, F. M. Wisser, C. Ziegler, L. Giebeler, M. H. Ruemmeli, J. Eckert, A. Eychmueller and S. Kaskel, *Adv. Energy Mater.*, 2014, **4**, 1300645.

179. Q. Zhao, X. Wang, C. Wu, J. Liu, H. Wang, J. Gao, Y. Zhang and H. Shu, *J. Power Sources*, 2014, **254**, 10-17.

180. D.-W. Wang, F. Li, M. Liu, G. Q. Lu and H.-M. Cheng, *Angew. Chem. Int. Ed.*, 2008, **47**, 373-376.

181. S. Dutta, A. Bhaumik and K. C. W. Wu, *Energy Environ. Sci.*, 2014, **7**, 3574-3592.

182. B. Xu, S. Hou, G. Cao, M. Chu and Y. Yang, *RSC Adv.*, 2013, **3**, 17500-17506.

183. R. Liu, J. Duay and S. B. Lee, *Chem. Commun.*, 2011, **47**, 1384-1404.

184. D. Lan, Y. Chen, P. Chen, X. Chen, X. Wu, X. Pu, Y. Zeng and Z. Zhu, *ACS Appl. Mater. Interfaces*, 2014, **6**, 11839-11845.

185. C. Yuan, J. Li, L. Hou, J. Lin, X. Zhang and S. Xiong, *J. Mater. Chem. A*, 2013, **1**, 11145-11151.

186. Z.-S. Wu, A. Winter, L. Chen, Y. Sun, A. Turchanin, X. Feng and K. Muellen, *Adv. Mater.*, 2012, **24**, 5130-5135.

187. B. G. Choi, M. H. Yang, W. H. Hong, J. W. Choi and Y. S. Huh, *ACS Nano*, 2012, **6**, 4020-4028.

188. X. Ma, J. Liu, C. Liang, X. Gong and R. Che, *J. Mater. Chem. A*, 2014, **2**, 12692-12696.

189. X. Jiang, X. Yang, Y. Zhu, J. Shen, K. Fan and C. Li, *J. Power Sources*, 2013, **237**, 178-186.

190. X. Zhu, P. Zhang, S. Xu, X. Yan and Q. Xue, *ACS Appl. Mater. Interfaces*, 2014, **6**, 11665-11674.

191. S. Wu, W. Chen and L. Yan, *J. Mater. Chem. A*, 2014, **2**, 2765-2772.

192. J. T. Zhang, S. Liu, G. L. Pan, G. R. Li and X. P. Gao, *J. Mater. Chem. A*, 2014, **2**, 1524-1529.

193. Q. Wu, Y. Xu, Z. Yao, A. Liu and G. Shi, *ACS Nano*, 2010, **4**, 1963-1970.

194. J. Xu, K. Wang, S.-Z. Zu, B.-H. Han and Z. Wei, *ACS Nano*, 2010, **4**, 5019-5026.

195. X. Yu, B. Lu and Z. Xu, *Adv. Mater.*, 2014, **26**, 1044-1051.

196. F. Zhang, D. Zhu, X. a. Chen, X. Xu, Z. Yang, C. Zou, K. Yang and S. Huang, *Phys. Chem. Chem. Phys.*, 2014, **16**, 4186-4192.

197. X. Xie, C. Zhang, M.-B. Wu, Y. Tao, W. Lv and Q.-H. Yang, *Chem. Commun.*, 2013, **49**, 11092-11094.

198. L. Zhang, F. Zhang, X. Yang, G. Long, Y. Wu, T. Zhang, K. Leng, Y. Huang, Y. Ma, A. Yu and Y. Chen, *Sci. Rep.*, 2013, **3**, 1408.

199. Y. Shao, H. Wang, Q. Zhang and Y. Li, *J. Mater. Chem. C*, 2013, **1**, 1245-1251.

200. G. K. Dimitrakakis, E. Tylianakis and G. E. Froudakis, *Nano Lett.*, 2008, **8**, 3166-3170.

201. F. Du, D. Yu, L. Dai, S. Ganguli, V. Varshney and A. K. Roy, *Chem. Mater.*, 2011, **23**, 4810-4816.

202. Z.-Y. Yang, Y.-F. Zhao, Q.-Q. Xiao, Y.-X. Zhang, L. Jing, Y.-M. Yan and K.-N. Sun, *ACS Appl. Mater. Interfaces*, 2014, **6**, 8497-8504.

203. Q. Li, J. M. Anderson, Y. Chen and L. Zhai, *Electrochim. Acta*, 2012, **59**, 548-557.

204. S.-I. Kim, J.-S. Lee, H.-J. Ahn, H.-K. Song and J.-H. Jang, *ACS Appl. Mater. Interfaces*, 2013, **5**, 1596-1603.

205. Y. Xiao, S. Liu, F. Li, A. Zhang, J. Zhao, S. Fang and D. Jia, *Adv. Funct. Mater.*, 2012, **22**, 4052-4059.

206. P. Yu, X. Zhang, D. Wang, L. Wang and Y. Ma, *Cryst. Growth Des.*, 2009, **9**, 528-533.

3 FABRICATION AND CAPACITIVE BEHAVIOR OF MnO_2 NANOPILLARS[*]

3.1 Introduction

Energy storage is vital for the development of numerous fields including portable electronic devices, medical devices, and transportation. It is also essential for the utilization of clean and renewable energy. The two major players that impact the growth of energy storage field are batteries and supercapacitors (SCs). Compared to Li-ion batteries, SCs have attracted considerable attention since they poses faster charge/discharge rates, higher power density and much longer lifetimes.[1, 2] As a signature of their reliability, SCs are being used in the emergency doors of Airbus A380, power back-up systems, pacemakers and airbags.[2, 3] Moreover, SCs are rugged, reliable, and maintenance free. However, the major bottleneck that hinders many practical applications of existing SCs is their low energy density (20x lower than batteries). To resolve this problem, one of the practical approaches is to use metal oxides such as RuO_2,[4] MnO_2,[5] NiO,[6] and CoO_x[7], as electrode materials. Their high energy density along with fast and reversible redox reactions at the surface of the electrode surface can significantly enhance the specific capacitance. In fact, the specific capacitance of these pseudocapacitive materials is multiple times better than that of the carbon-based materials in electric double-layer capacitors (EDLCs),[8, 9] which physically store charges via reversible ion absorption at electrode/electrolyte interface.

---

[*] The work presented in this chapter has been published in Z. Yu, B. Duong, D. Abbitt and J. Thomas, *Adv. Mater.* 2013, 25, 3302-3306 and Z. Yu, J. Moore, B. Duong, C. Li, and J. Thomas, *ECS Trans.* 2014, 61, 49-53. Reproduction has been permitted by © 2013 WILEY and © 2014 ECS.

Among pseudocapacitors, ruthenium oxide (RuO_2)-based devices have shown the highest specific capacitance of 1580 F/g (at 1mV/s).[10] However, its toxicity and high cost make RuO_2 less attractive for practical applications. Among other low-cost alternatives, MnO_2 has stood out as the most promising material due to many remarkable features such as environment friendly, low cost, and high theoretical specific capacitance.[11-13] However, it is highly challenging to reach this value due to the low electrical conductivity of MnO_2 (~10^{-5}-10^{-6} S/cm).[14, 15] To improve the electrical conductivity and boost the performance of pseudocapacitors, Simon and Gogotsi[2] proposed the development of binder-free electrodes in which pseudo-capacitive materials would be conformally deposited onto highly conductive and well-ordered nanostructured electrodes. To demonstrate this idea experimentally, various architectures such as arrays of nanowires,[16, 17] nanotubes,[18, 19] and carbon textile, [20, 21] have been used either as electrode materials or framework to deposit pseudo-capacitive materials. However, the high aspect ratio (1:8 or more) of these arrays usually leads to the collapse of the nanowire into its neighboring nanowires, resulting in the decrease of useful surface area, reduction of deposited active materials and limited accessibility of electrolyte. In addition, typical methods for engineering nanoarchitectures mainly rely on techniques such as self-assembly or sacrificial aluminum oxide templates. The producibility of these techniques is modest while the necessary amount of template materials or precursors is generally much more than the product weight. Furthermore, for every nanostructure developed, expensive template materials are eventually removed by dangerous chemical reagents like hydrofluoric acid (HF).[22] Alternatively, nanoimprint lithography (NIL) has become a promising candidate for preparing nanoscale structures.[23, 24] It is a simple, cost-effective, high-resolution, high throughput method for fabricating polymeric nanostructures in a short time. The

NIL process involves the transfer of patterns from a prefabricated mold to a thermoplastic film on a substrate at high temperature and pressure. Even though recent advances allow various materials to be printed by NIL,[25] it is extremely challenging to print a thermoplastic polymer like polyacrylonitrile (PAN) using the typical NIL process since it lacks the viscous flow state when heated in ambient atmospheres.[24] In addition, fabrication of large area structures is another challenge because it requires the substrate and the template to undergo a heating and cooling cycle each time a structure needs to be printed. The thermoplastic polymer would be deformed when heated to its glass transition temperature, hence, previously printed nanopatterns cannot be preserved while printing the neighboring structures at high temperature. Moreover, it is currently impossible to print structures side-by-side using solely one mold by typical NIL technique. Inability to overcome these stringent conditions held back the development of large area nanoimprinted structures using NIL.

Here, we present a facile method to print large area, well-ordered nanostructured supercapacitor electrodes. Our supercapacitor electrode fabrication method is a three-step process involving: (i) fabrication of an inert polymer nanostructure by spin casting on a mold and transferring to a substrate (ii) deposition of current collector electrode material by sputtering and (iii) electrochemical deposition of MnO_2 on to the nanostructured electrode (Figure 3.1a).

The process of fabricating nanostructured PAN film by this approach is entirely new, easy, fast and readily reproducible. To obtain a nanostructured PAN film, we first spin-coated PAN solution on a pre-fabricated silicon (Si) mold, followed by curing and demolding. This film was then directly transferred onto a substrate that was previously coated with a layer of PAN film to assure good adhesion of the patterned film with the substrate. This complete printing process can be performed in less than 5 minutes, but can be carried out in a much faster pace if automated. We have successfully printed a 1cm × 1cm physical area with nanostructures within this time frame; without using any expensive equipment. Moreover, the mold can be used several hundred times without any noticeable damage. Since no temperature or pressure is applied during the transfer, a large area of printed structures can be easily prepared by stitching one film next to another as shown in Figure 3.1b. In addition, it is also possible to print these structures on a flexible substrate to make rolled design supercapacitors. To improve mechanical integrity, we stabilized the PAN film at 250 °C for 3 hours. It is worth mentioning that there are at least two advantages in using PAN as the precursor. Compared to the preparation of polydimethylsiloxane (PDMS) stamp used in common soft lithography techniques,[26] a PAN replica can be prepared in a much shorter-time scale. A PDMS replication process from a master mold typically requires curing at least an hour in a vacuum oven to avoid the entrapment of air bubbles. Moreover, replicating nanosized features using elastomeric stamps often involves the use of hard-PDMS,[27] which cause cracking on the stamp surface during the de-molding process and resulting in unfaithful replication.[28] Meanwhile, fracturing does not happen in our PAN film. This is confirmed based on more than 100 samples characterized under scanning electron microscope (SEM).

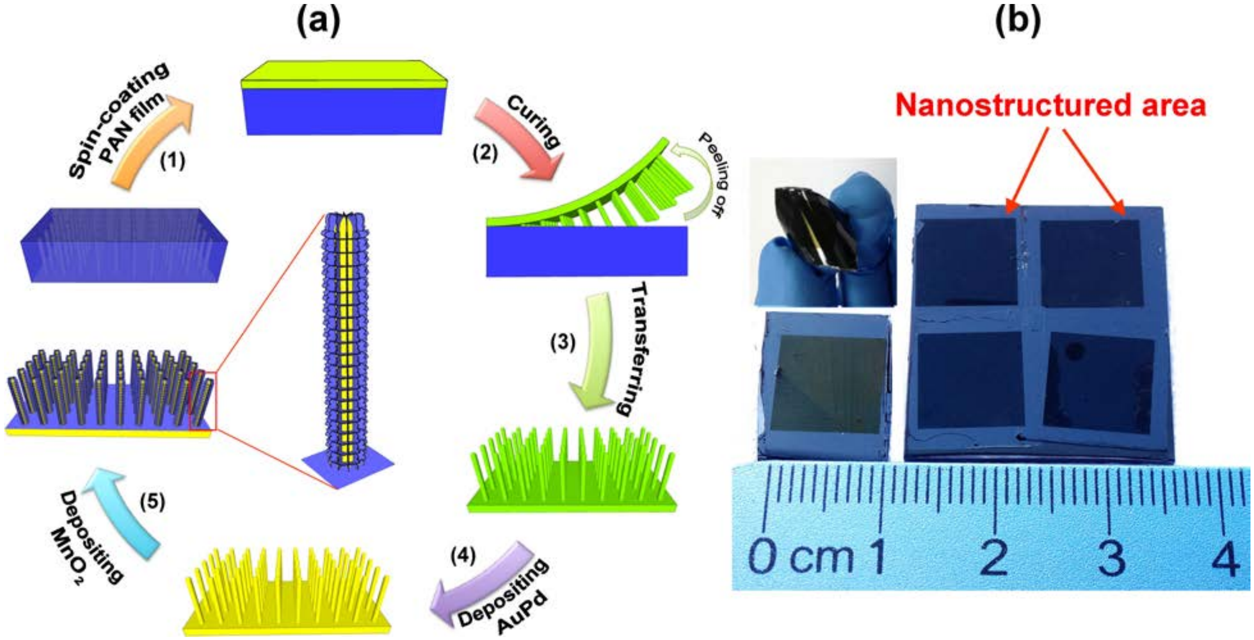

Figure 3.1 (a) Schematic illustration showing the development of MnO_2 coated electrodes. (b) Photographs show single nanostructured electrode (dark area) on a rigid substrate and a flexible substrate. A larger area electrode composed of four nanostructures was also prepared by stitching them side-by-side.

3.2 Preparation of Nanostructured Substrates

The polyacrylonitrile (PAN) solution was prepared by dissolving 8wt% of high molecular (Mw 15000) PAN material in dimethyl formamide (DMF). Appropriate amount of (PAN) solution was spin coated onto a nano-holes structure (mold) uniformly. The as-spun mold was heated at 150 °C for 2 min to evaporate off the solvent. This film was then directly transferred onto a substrate that was previously coated with a layer of PAN film and stabilized at 250 °C for 3 hours. SEM Figure 3.2a shows the top view of the as-printed structures and it reveals arrays of highly ordered nanopillar structures. These nanopillars have diameter of ~140 nm and height of ~ 250 nm, and center-to-center distance of ~200nm.

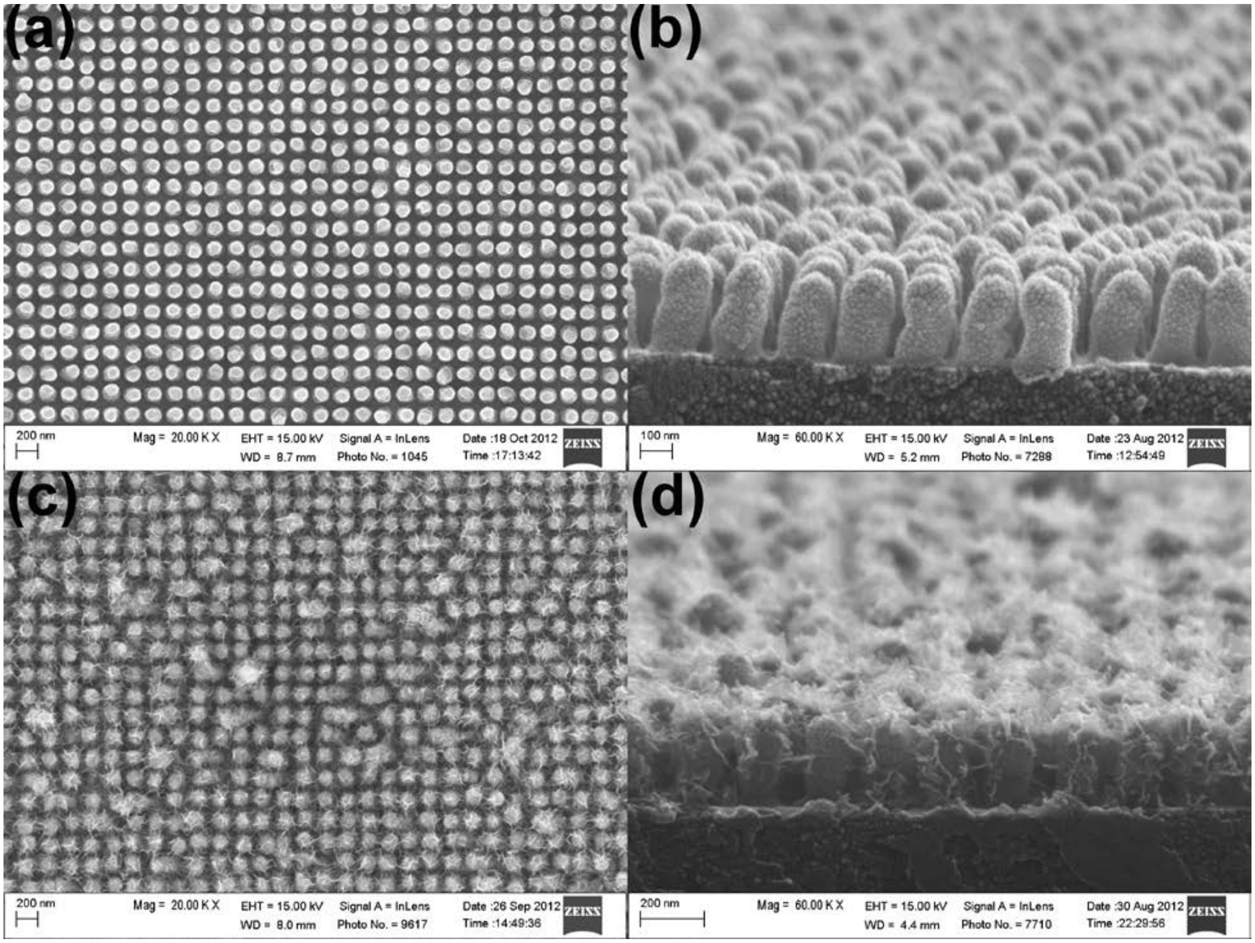

Figure 3.2 SEM images show (a) top view of as-printed PAN nanostructures, (b) side view of nanostructures after sputter coating of AuPd. Electrochemically deposited MnO_2 nanoparticulates on pillar nanoarrays; (c) top view and (d) side view.

3.3 Fabrication of Electrodes

Prior to depositing MnO_2, we coated a thin layer of gold-palladium (AuPd; Au to Pd ratio is 60:40) onto the nanostructured film and it served as an electrode for both MnO_2 electrodeposition and as a current collector in our supercapacitor design. AuPd conducting layer was sputter-coated at 40 mA for 5 minutes (Emitech K550). After AuPd deposition, the pillars dimensions increased to ~170nm in diameter, ~300nm in height (Figure 3.2b). MnO_2 thin layer was deposited onto the nanostructured substrate using an anodic electrodeposition method at a constant current of 0.5 mA cm^{-2} for 45 s-10 minutes. The electrolyte for the deposition was prepared by dissolving 0.01M manganese acetate ($MnAc_2$) and 0.02 M ammonium acetate (NH_4Ac) in a solvent mixture of 90% DI water and 10% dimethyl sulfoxide (DMSO). As shown in Figure 2c, electrodeposited MnO_2 were coated onto each pillar. The diameter and height of the pillars increased to ~200nm and ~340nm, respectively (Figure 3.2c and d). Our calculations based on the dimensions of nanopillars from SEM images reveal that the surface area of nanostructured region is ~4.5 times higher than that of the planar region.

3.4 Materials Characterization

Morphologies were characterized using scanning electron microscopy (SEM, ZEISS ULTRA 55). Chemical compositions were analyzed by X-ray photoelectron spectroscopy (XPS, PHI 5400). Cyclic voltammetry (CV), and galvanostatic charge/discharge (GCD) were performed on an electrochemical workstation (Bio-Logic, SP-150) using a three-electrode configuration in 1M Na_2SO_4. CV was carried out at different scan rates of 5, 20, 50, and 100mV s^{-1}. GCD was measured at 10, 20, 50, and 100A g^{-1}.

3.5 Electrochemical Properties of MnO_2 Nanopillars

To evaluate and compare the enhancement in performance of nanostructured and planar electrodes, we performed cyclic voltammetry (CV) measurements using a three-electrode configuration. CVs of nanostructured electrode (NE) at a scan rate of 100 mV/s (Figure 3.3a) show more rectangularity than that of planar electrode (PE), implying NE exhibited better capacitive behavior. The current obtained in NE compared to PE indicates better electron transportation and MnO_2 utilization as nanostructured design is used.[29] Such superior performances of the MnO_2 coated onto AuPd nanostructures may attribute to two reasons: (1) the large contact area between current collector and active material can significantly shorten the electron transportation path length and (2) decorating active nanomaterial onto nanostructured current collectors leads to the increase in number of electrochemically active sites for the redox reaction. This facilitates rapid diffusion of the cations during the charging/discharging process. In order to investigate the contribution of AuPd into total specific capacitance, CV measurements of pure AuPd without MnO_2 on both NE and PE were carried out. The results reveal the contribution of pure AuPd metal is insignificant (Figure 3.3a). We also performed CV measurements of the NE under different scan rates (Figure 3.3b). The rectangular consistency of these curves at various scan rates ranging from 5 to 100 mV/s reveals excellent capacitive behaviors of NE. The gravimetric specific capacitance of NE reached up to 603 F/g at a scan rate of 5mV/s, while it was 298 F/g for PE (Figure 3.3c). Calculation of specific capacitance is based on subtraction of the capacitance which belongs to the AuPd from the total capacitance. For both gravimetric and areal capacitances at various scan rates, NE showed a consistent enhancement of about 2 times than that of PE. Additionally, the loading mass of MnO_2 is controllable by varying the electrodeposition time. Higher loading mass of MnO_2 can be readily reached by extending the electrodeposition time. For example, a mass of 0.15 mg/cm^2 can be easily reached by extending the electrodeposition time to 10 min, and its specific capacitance still remained 201 F/g at a scan rate of 5 mV/s.

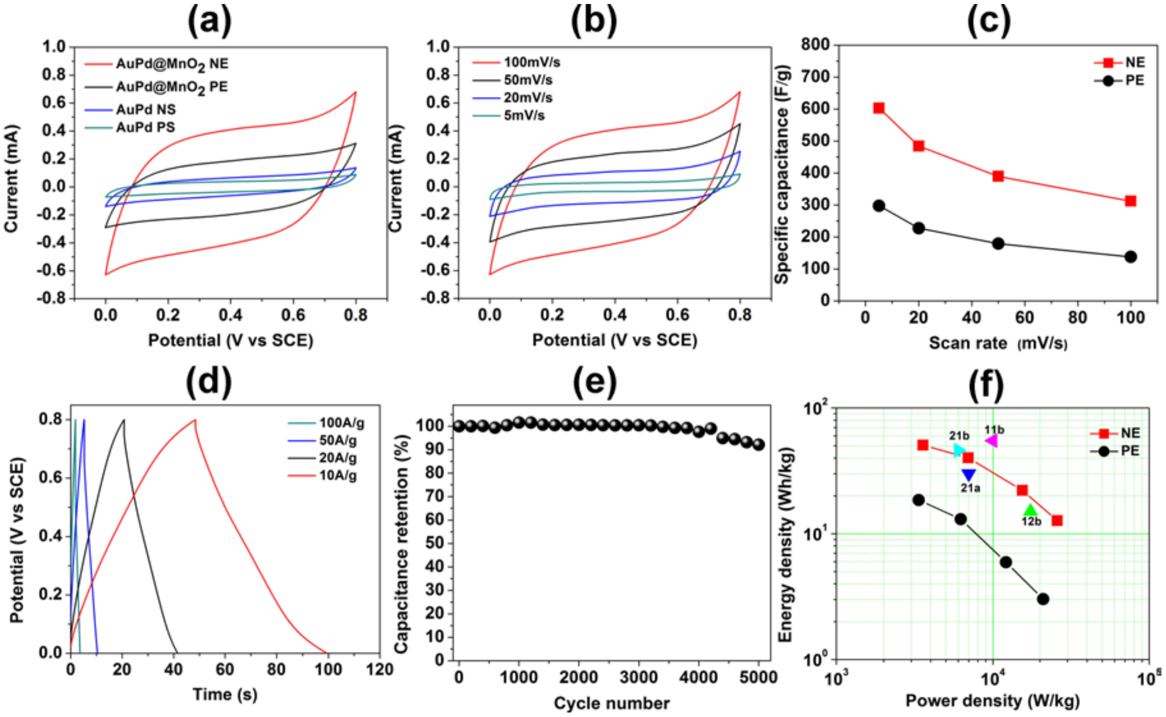

Figure 3.3 (a) CV curves of NE and PE at a scan rate of 100 mV s^{-1} in 1M aqueous Na_2SO_4 electrolyte. (b) CV curves of NE at different scan rates (5-100 mV s^{-1}). (c) Specific capacitances of NE and PE as a function of the scan rate. (d) GCD curves of NE at different current densities (10-100 A g^{-1}). (e) Cycling performance of NE during 5000 cycles at a scan rate of 1000 mV s^{-1}. (f) Energy and power densities of NE and PE.

To learn about the charge storage capacity of our electrodes, we carried out galvanostatic charge/discharge (GCD) measurements. The specific capacitances of NE and PE at current density of 10 A/g are 603 F/g and 237 F/g, respectively. A 150% enhancement in specific capacitance confirms the remarkable advantage of using nanostructured design. GCD curves of NE and PE at different current density validate its efficient capacitive behavior (Figure 3.3d). As the current density increases from 10 to 100 A/g, the specific capacitance of NE still remains at 293 F/g, while it is only 96 F/g for PE. Cycling performance is another important factor that determines the use of SCs in many practical applications. Figure 3.3e shows the cycling performance of the NE after long-term cycling at a scan rate of 1000 mV/s. The capacitance retention of NE is quite stable and still remains 93% of its initial value even after 5000 cycles. Figure 3.3f shows the energy and power densities of the NE and PE. The highest energy density of NE reaches up to 50.68 Wh/kg at a power density of 3.57 kW/kg, while it is only 18.53 Wh/kg for PE at a power density of 3.35 kW/kg. In terms of power density, the highest value for NE can reach up to 25.84 kW/kg at an energy density of 12.73 Wh/kg, while it limits to 20.95 kW/kg for PE at an energy density of 3.02 Wh/kg. The energy and power densities in this study are comparable to other studies using core-shell nanowires and nanotubes of MnO_2.[17, 19, 30, 31] Moreover, these results reveal that our NE fulfill the power requirement (15 kW/kg) for PNGV (Partnership for a New Generation of Vehicles).[32]

3.6 Conclusion

In summary, we have reported the development of MnO_2 decorated, highly ordered nanopillar current collector electrodes for supercapacitors. This novel nanostructure design enhances the surface area nearly 4.5 times compared to that of the planar electrode. Moreover, the nanostructured electrode shows remarkable enhancements in specific capacitance, charge/discharge ability, as well as cyclic stability. The simplicity of the nanoarchitectured electrodes and their phenomenal performances has shown promising features for future energy storage systems.

3.7 References

1. J. R. Miller and A. F. Burke, *Electrochem. Soc. Interface*, 2008, **17**, 53-57.
2. P. Simon and Y. Gogotsi, *Nat. Mater.*, 2008, **7**, 845-854.

3. J. R. Miller and P. Simon, *Science* 2008, **321**, 651-652.

4. C. C. Hu, K. H. Chang, M. C. Lin and Y. T. Wu, *Nano Lett.*, 2006, **6**, 2690-2695.

5. X. Lu, D. Zheng, T. Zhai, Z. Liu, Y. Huang, S. Xie and Y. Tong, *Energy Environ. Sci.*, 2011, **4**, 2915-2921.

6. J. W. Lee, T. Ahn, J. H. Kim, J. M. Ko and J. D. Kim, *Electrochim. Acta*, 2011, **56**, 4849-4857.

7. X. Xia, J. Tu, Y. Mai, X. Wang, C. Gu and X. Zhao, *J. Mater. Chem.*, 2011, **21**, 9319-9325.

8. Y. Zhang, H. Feng, X. Wu, L. Wang, A. Zhang, T. Xia, H. Dong, X. Li and L. Zhang, *Int. J. Hydrogen Energ.*, 2009, **34**, 4889-4899.

9. J. Jiang, Y. Li, J. Liu, X. Huang, C. Yuan and X. W. D. Lou, *Adv. Mater.*, 2012, **24**, 5166-5180.

10. C. C. Hu and W. C. Chen, *Electrochim. Acta*, 2004, **49**, 3469-3477.

11. Y. Jeong and A. Manthiram, *J. Electrochem. Soc.*, 2002, **149**, A1419-A1422.

12. G. Yu, L. Hu, M. Vosgueritchian, H. Wang, X. Xie, J. R. McDonough, X. Cui, Y. Cui and Z. Bao, *Nano Lett.*, 2011, **11**, 2905-2911.

13. C. Liu, F. Li, L. P. Ma and H. M. Cheng, *Adv. Mater.*, 2010, **22**, E28-E62.

14. D. Bélanger, L. Brousse and J. W. Long, *Electrochem. Soc. Interface*, 2008, **17**, 49-52.

15. R. Chandrasekaran, Y. Soneda, J. Yamashita, M. Kodama and H. Hatori, *J. Solid State Electrochem.*, 2008, **12**, 1349-1355.

16. J. Liu, J. Jiang, C. Cheng, H. Li, J. Zhang, H. Gong and H. J. Fan, *Adv. Mater.*, 2011, **23**, 2076-2081.

17. J. Yan, E. Khoo, A. Sumboja and P. S. Lee, *Acs Nano*, 2010, **4**, 4247-4255.

18. Q. Li, Z. L. Wang, G. R. Li, R. Guo, L. X. Ding and Y. X. Tong, *Nano Lett.*, 2012, **12**, 3803-3807.

19. J. H. Kim, K. H. Lee, L. J. Overzet and G. S. Lee, *Nano Lett.*, 2011, **11**, 2611-2617.

20. Y. C. Chen, Y. K. Hsu, Y. G. Lin, Y. K. Lin, Y. Y. Horng, L. C. Chen and K. H. Chen, *Electrochim. Acta*, 2011, **56**, 7124-7130.

21. Y. E. Chen, Z. N. Yu, Y. G. Chen, L. Q. Luo and X. Wang, 2011.

22. A. L. M. Reddy, S. R. Gowda, M. M. Shaijumon and P. M. Ajayan, *Adv. Mater.*, 2012, **24**, 5045-5064.

23. S. Y. Chou, P. R. Krauss and P. J. Renstrom, *Appl. Phys. Lett.*, 1995, **67**, 3114-3116.

24. L. J. Guo, *J. Phy. D: Appl. Phys.*, 2004, **37**, R123.

25. J. Thomas, P. Gangopadhyay, E. Araci, R. A. Norwood and N. Peyghambarian, *Adv. Mater.*, 2011, **23**, 4782-4787.

26. D. Lipomi, R. Martinez, L. Cademartiri and G. Whitesides, *In: Polymer Science: A Comprehensive Reference*, 2012, **vol. 7**, p211.

27. B. Michel, A. Bernard, A. Bietsch, E. Delamarche, M. Geissler, D. Juncker, H. Kind, J. P. Renault, H. Rothuizen and H. Schmid, *IBM J. Res. Dev.*, 2001, **45**, 697-719.

28. Y. Y. Huang, W. Zhou, K. Hsia, E. Menard, J. U. Park, J. A. Rogers and A. G. Alleyne, *Langmuir*, 2005, **21**, 8058-8068.

29. G. Yu, L. Hu, N. Liu, H. Wang, M. Vosgueritchian, Y. Yang, Y. Cui and Z. Bao, *Nano Lett.*, 2011, **11**, 4438-4442.

30. X. Lu, T. Zhai, X. Zhang, Y. Shen, L. Yuan, B. Hu, L. Gong, J. Chen, Y. Gao and J. Zhou, *Adv. Mater.*, 2012, **24**, 938-944.

31. L. Bao, J. Zang and X. Li, *Nano lett.*, 2011, **11**, 1215-1220.

32. D. W. Wang, F. Li, M. Liu, G. Q. Lu and H. M. Cheng, *Angew. Chem. Int. Ed.*, 2008, **47**, 373-376.

4 FABRICATION OF SYMMETRIC SUPERCAPACITORS WITH CARBON NANOPILLARS*

4.1 Introduction

The availability of advanced materials and cost-effective tools for fabrication are essential to the advancement of future sciences and technologies as unprecedented applications will be possible by using nanomaterials. In order to gain rapid progress toward current intriguing challenges, research on existing and new materials has been carried out intensively. Among all, carbon has received tremendous attention since it exhibits many unique structures along with numerous useful properties for a variety of applications, from simple uses for writing or as a coloring agent to a major role in the electrochemical energy storage industry. To date, considerable effort has been devoted to the development of carbon-based electrodes because of its lightweight, high electrical conductivity, stable chemical and electrochemical properties at low cost.[1] Different carbon allotropes exhibiting high surface-to-volume ratio such as graphene,[2-4] reduced graphene oxide,[5-7] carbon nanotubes,[8, 9] onion-like carbon[10, 11] and graphite particles[12] have been considered for use in future batteries and supercapacitors. Unfortunately, processing factors such as temperature, gas flow rates, catalysts, etc., still need to be optimized in order to obtain these sophisticated structures with the desired properties. Amorphous carbon, meanwhile, offers simpler synthesis pathway and still maintains necessary properties to be used in many applications. To improve the modest surface area of amorphous carbon, tailoring carbon into various nanoarchitectures using templates particularly stands out. Carbon nanostructures can be

---

* The work presented in this chapter has been published in B. Duong, Z. Yu, P. Gangopadhyay, S. Seraphin, N. Peyghambarian, and J. Thomas, *Adv. Mater. Interfaces* 2014, 1, 130014. Reproduction has been permitted by © 2014 WILEY.

achieved by diffusing carbon precursors from polymers (i.e. photoresists)[13] or hydrocarbon gases into inorganic templates like anodic aluminum oxide (AAO),[14, 15] silica colloidal crystals[16, 17] and zeolite[18, 19] then followed by carbonization at high temperature (Figure 4.1a). After carbonization, these templates must be removed by chemical etching. With these techniques, nanostructured carbon can be fabricated. However, the large-scale manufacturability via these techniques is limited. Additionally, template materials are eventually removed by expensive and hazardous chemical reagents such as hydrofluoric (HF) acid each time a structure is developed. These unavoidable post-processing steps make these methods incompatible for large area production of nanostructured carbon electrodes.

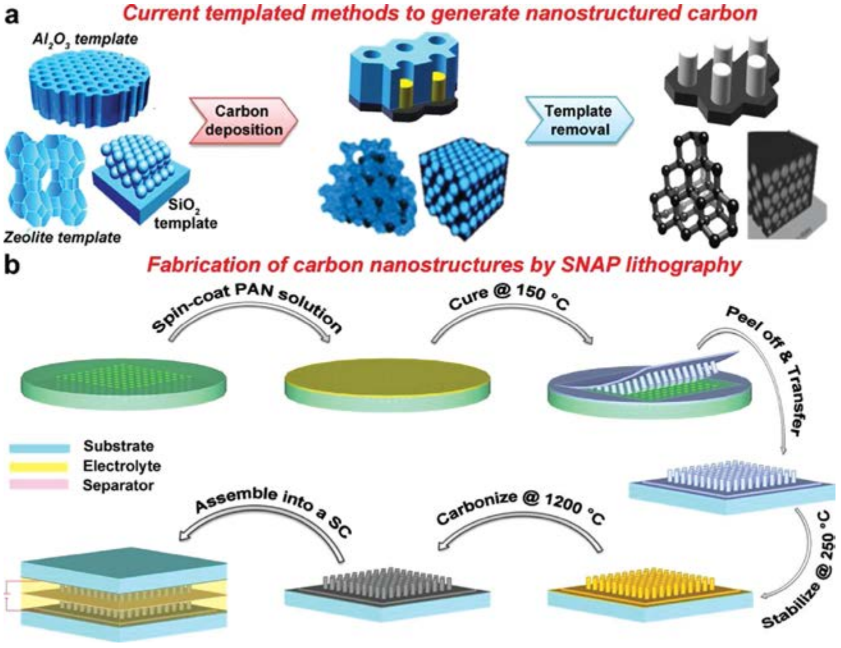

Figure 4.1 (a) Current templated methods for generating carbon nanostructures. (b) Fabrication of carbon nanostructures by SNAP method. A pre-fabricated mold is spin coated with a partially cyclized PAN solution. The film is cured at 150 °C before transferring to a substrate coated with pre-cured PAN film. A nanostructured PAN film is obtained by separating the mold. The PAN film is stabilized by heating to 250 °C for 3 hours. This film is heat treated at higher temperatures to convert to carbon/graphite. Alternatively, laser can be used to instantaneously carbonize the structures within a few seconds. An EDLC supercapacitor device is fabricated with two nanostructured carbon electrodes.

An attractive low cost alternative is nanoimprinting lithography (NIL), which is used to print nanostructures from a hard mold onto a thermoplastic polymer[20-22] under high temperature (80-100 °C above the glass transition temperature, T_g) and pressure. Despite being a thermoplastic polymer, direct printing of structures from polyacrylonitrile (PAN), a common source used for making a variety of carbon products[23-25], is almost impossible by typical NIL process because it lacks the viscous flow state[21] when heated at ambient conditions. Moreover it forms a cyclized structure as it is heated above 200 °C. Inability to overcome the stringent conditions required for the NIL resists, which are absent in carbon precursor polymers, has held back the development of printed carbon nanostructures. To circumvent these challenges, we describe here the spin-on nanoprinting (SNAP) technique, which can be used to accomplish an ideal carbon electrode structures[26] for supercapacitors (SCs) and an easy pathway to fabricate large carbon nanostructure area. This technique is based on the principle that a thin layer of polymer solution is spun-on to a prefabricated mold and transferred directly to a substrate pre-coated with an under-cured polymer film[27] thereby eliminating the necessity of an adhesive resin and UV source. A freestanding film of printed PAN can be developed by simply peeling-off the film from the mold and converting it into carbon. The SNAP technique is simple, fast and economical since it requires only a spin coater and a pre-fabricated mold to perform nanostructuring of carbon. Since the SNAP process can be carried out at room temperature and does not require external pressure, the mold can be used several hundred times without having any noticeable mold degradation. Our previous studies have shown that SNAP is highly suitable to produce micro-, nano-structures from diverse materials,[28, 29] especially for fabricating a large nanostructure area for pseudo-supercapacitors.

The fabrication process from casting the material to transferring, converting it to carbon and assembling it into an electric double-layer capacitor (EDLC) is summarized in Figure 1b. Preparation of the printing medium is explained in detail in the supplementary information. To obtain a nanostructured electrode, we spin-coated PAN solution on a pre-fabricated silicon (Si) mold, followed by curing and removal of the mold. This complete printing process can be performed in less than 5 minutes, but can be carried out in a much faster pace if automated. We have successfully printed a 1cm × 1cm physical area with nanostructures within this time frame without using any expensive printing equipment. The stabilization process of PAN film involved oxidative cyclization of polymer chains by heating the nanostructured films to 250 °C in the presence of oxygen. The formation of a cyclized compound is highly advantageous in preserving the printed structure to withstand the rigors of high temperature processing during carbonization. During carbonization, stabilized PAN does not melt but is converted to various types of carbon depending on the heat treatment involved.

4.2 Preparation of Supercapacitor Devices

Nanostructured and planar supercapacitor devices were assembled by two identical electrodes, which were separated by an ion-porous separator. Silver paste was used to connect copper wires to the carbon films for external electrical contact. To assure reliability of measurements for later comparisons, Kapton tape was used to mask 1×1 cm^2 active area on both planar carbon films and nanostructured carbon films. A separator was wetted by a selected electrolyte and placed in between two identical electrodes. A wooden clip was used to secure the assembled device and for easier handling.

4.3 Characterization Methods

Figure 4.2a and b shows the Scanning Electron Microscopy (SEM) top view image of the PAN pillars printed before and after carbonization, respectively. Printed PAN is converted to carbon nanopillars by heating it to above 800 °C at a rate of 5 °C/min in argon atmosphere. Cross-sectional views of the printed pillars before and after carbonization are given in the insets. The mold showed minimum deterioration even after printing several hundreds of PAN nanostructures. The diameter of the printed carbonized pillars is about 95 nm and the height is about 200 nm. Since the printed structure is transferred to a PAN precoated substrate, large area printed structures can easily be developed by printing nanostructures adjacent to each other. As a proof-of-principle, Figure 4.2c shows the photographs of such a film printed side-by-side. Moreover, it is also feasible to peel off the printed PAN film from the mold for making standalone nanostructured carbon electrodes (Figure 4.2d). We used X-Ray diffraction (XRD) and Raman spectroscopy to monitor the carbonization of stabilized PAN nanostructures. All the samples used herein are made by thermal carbonization. The results of the XRD measurements of the carbonized nanostructured film at 800 °C, 1,000 °C and 1,200 °C are compiled in Figure 4.2e. XRD patterns yield a single characteristic peak at a Bragg angle of $2\theta = 25\ °$ which corresponds to (002) plane of graphite. The intensity and sharpness of the (002) peak gradually increases with increasing heat treatment temperature (HTT). The visible (002) peak at 800 °C indicates that the PAN films exhibit crystalline graphitic domains and more complete carbonization occurs at higher HTT. It was found that the interlayer spacing of graphite is 0.347, 0.0345 and 0.343 nm as the temperature sets 800 °C, 1000 °C and 1200 °C, respectively. The structural rearrangement in the (002) plane is confirmed by the change in graphitic domains L_c

from 0.40 at 800°C to 1.27 nm at 1000 °C. Referring to the phase analysis of similar carbon fibers derived from PAN, this can be attributed to the transition from amorphous to nanocrystalline graphite. The Raman spectra of nanoimprinted PAN film carbonized at 800 °C, 1000 °C and 1200 °C are given in Figure 4.2f. The peaks at 1367 and 1593 cm^{-1} are assigned to disordered and ordered phases of carbon, respectively. The positions of both D-band and G-band increase slightly while their FWHM decreases significantly with carbonization temperature. The relative intensity of the G-band increases with HTT, suggesting the increased ordering in carbon structure.

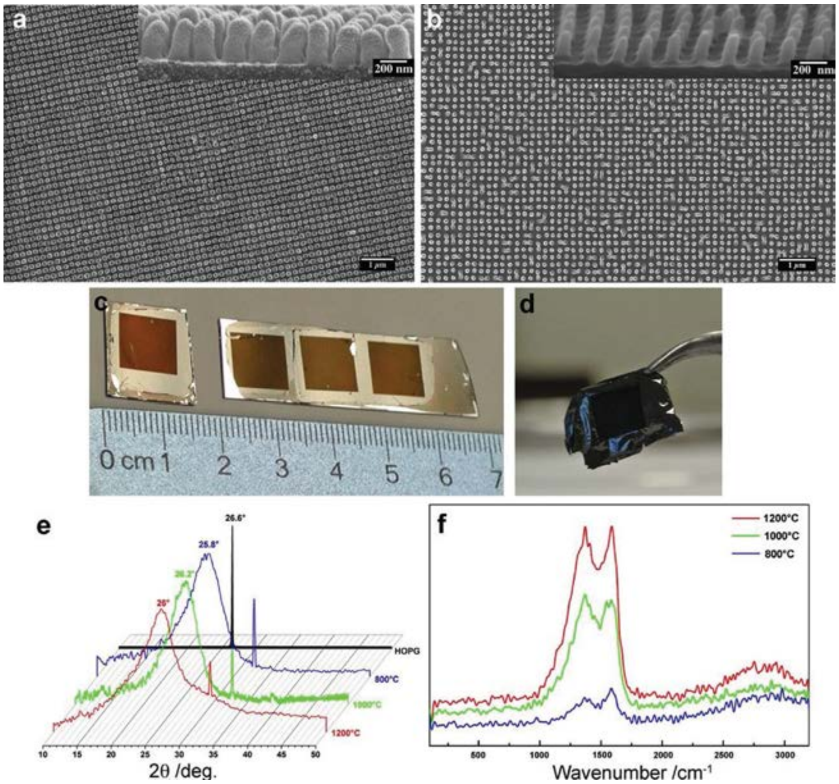

Figure 4.2 SEM images of top view and cross sectional view (inset) of printed PAN pillars (a) before and (b) after carbonization. The printed PAN nanopillars have a diameter of about 124 nm and height of about 250 nm. After carbonization, the diameters and heights of the structures are reduced to about 95 nm and 200 nm, respectively. (c) A photograph shows single nanostructured electrode (left) after stabilization at 250 °C on a rigid substrate. A larger area electrode composed of three nanostructures was prepared by stitching them side-by-side. (d)

Photograph of a freestanding nanostructured carbon film. (e) X-ray diffraction (XRD) patterns and (f) Raman spectra of nanostructured carbon film carbonized at 800 °C, 1,000 °C and 1,200 °C, respectively.

Following best-practice methods for determining an electrode material's performance for supercapacitors,[30] we measured the performance of two-electrode symmetrical supercapacitor cells on an electrochemical workstation (Bio-Logic, SP-150). Electrochemical properties of both planar and nanostructured supercapacitors were analyzed using cyclic voltammetry (CV), Galvanostatic charge-discharge (GCD) and cyclic stability. The CV curves were measured in the range of 0 and 1 V in H_2SO_4 (1M) and 0-3 V in ionic liquid (IL), $EMIMBF_4$ at scan rates of 5, 10, 20, 50, 100, 500, 1,000 mVs^{-1}. Higher scan rate of 5,000, 10,000 and 20,000 mVs^{-1} were tested for IL electrolyte. GCD curved were obtained at various constant current density of 1, 2, 5 μAcm^{-2} and 0.01, 0.02, 0.05, 0.1 $mAcm^{-2}$. Higher current density of 0.5, 1 and 2 $mAcm^{-2}$ were evaluated for devices using IL electrolyte.

4.4 Performance Evaluation of the Devices Based on Carbon Nanopillars

To demonstrate the application of printed nanostructured carbon films as a potential candidate for supercapacitor electrodes, we constructed a planar device (PLD) and nanostructured device (NSD) and analyzed their electrochemical performance using cyclic voltammetry (CV) and galvanostatic charge/discharge (GCD). As shown in Figure 4.3a and b nearly rectangular shaped CV curves are obtained even at high scan rates, indicating high performance capacitor devices. The calculated specific capacitance of PLD is 0.007 mF/cm^2. This value increased to 0.138 mF/cm^2 for NSD, which is in the same range as nanostructured carbon devices prepared by AAO templates along with chemical vapor deposition method in a recent report.[31] Due to uncertainty in the determination of the exact mass of carbonized PAN films, it is more appropriate to express the capacitance in terms of geometrical area instead of in gravimetric unit. The advantage of having nanostructured electrodes is clearly evident in ionic liquid (IL) electrolyte. At the same scan rate, the specific capacitance of NSD (3.4 mF/cm^2) is substantially higher than that of the PLD (0.05 mF/cm^2) in IL ($EMIMBF_4$) electrolyte. The calculated capacitance of NSD is even higher than that of typical electrical double-layer microcapacitors (0.4-2 mF/cm^2).[11] An overview comparison in capacitive behavior between PLDs and NSDs in different electrolytes is shown in Figure 4.3c. Our surface area (SA) calculations show that within 1 cm^2 footprint of the nanopillars, the SA is enhanced about 4 times compared to a planar film. With this enhancement in SA, the experimental results demonstrate that using the nanostructured electrode, the areal specific capacitances of the PLD were enhanced by at least an order of magnitude in aqueous electrolyte and two orders of magnitudes in IL electrolyte. A reproducible and stable capacitive behavior was obtained up to 10,000 cycles (Figure 4.3d) due to the mechanical stability of carbon. The average capacitance still remained >95% of the initial capacitance. We performed a shelf-life test on the same device after a week, interestingly, the capacitance slightly increased and exhibited an excellent cyclic stability of >96% of its initial response.

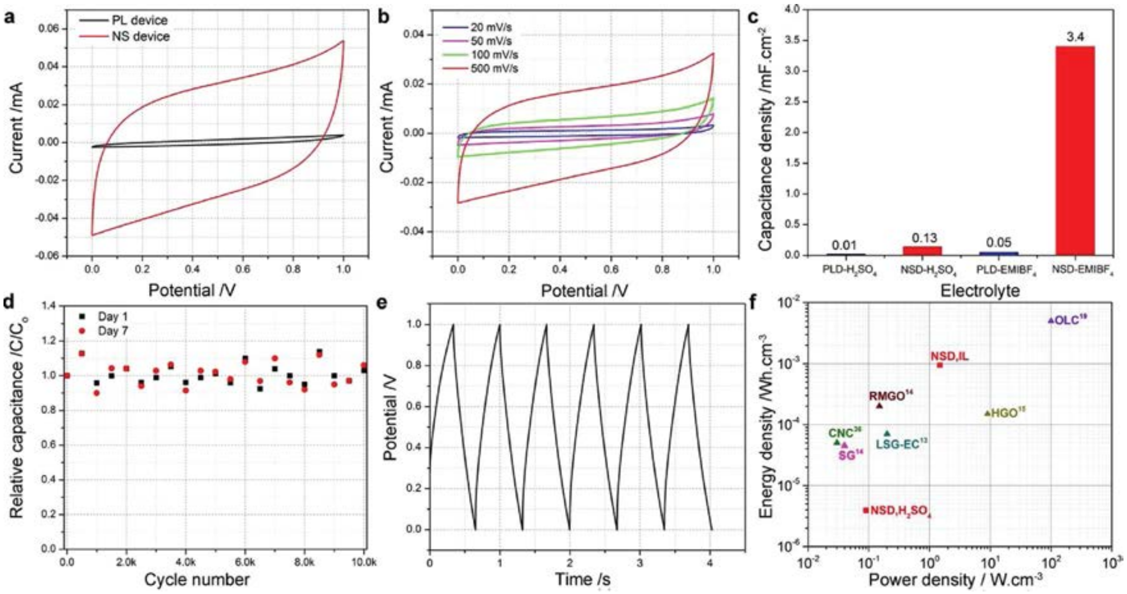

Figure 4.3 (a) Cyclic voltammetry curves of nanoarchitectured-supercapacitor device made of planar carbon films and nanostructured films at 1,000 mV/s, (b) CV curves of NSD at 500 mV/s, 100 mV/s, 50 mV/s and 20 mV/s. (c) Histogram comparison of specific area-based capacitance of NSD and PSD in different electrolytes. (d) The NS device shows excellent cyclic stability and retains >96% of its initial capacitance after 10,000 cycles. (e) Galvanostatic charge-discharge curves of NSD evaluated at 0.05 mA/cm^2. (f) Ragone plot of the specific energy and power density (per cm^3) of NSD in H_2SO_4 and ionic liquid (IL) *without* metal current collector electrodes compared to other supercapacitor devices with metal current collector electrodes. SG: single layer graphene, RMGO: reduced multilayer graphene oxide, HGO: hydrated graphitic oxide, LSG-EC: laser-scribed graphene electrochemical capacitor, OLC: onion-like carbon, CNC: carbon nanocup.

Galvanostatic charge/discharge (GCD) curves of the device show symmetric triangular shapes of the device, demonstrating the formation of an efficient electrical double layer capacitor in the nanostructured electrodes (Figure 4.3e). To learn more about the Coulombic efficiency, we calculated the ratio of times for charging and discharging based on Galvanostatic profile and found that the efficiency of NSD is 87 % while that of PLD is 78 %, confirming a better charge transfer system in NSD. Compared to a planar electrode, ion diffusion length is much shorter when a nanostructured electrode is used which enables higher ion transport from the electrolyte reservoir to the electrode surface. This assists the devices to operate at high current rate, which is an important consideration for practical applications. It is worth mentioning that typical porous carbon-based EDLC are always known to suffer from electrolyte kinetic problems that are associated with long diffusion distance from electrolytic solution to inner pores. Several studies have shown that having nanopillar/nanorod/nanotube type structures can decrease the diffusion length better than nanoporous structures.[32, 33] Another factor affecting the accommodation of charges in supercapacitors is adsorption of ions. This improvement maximizes the number of charges stored per weight or volume; consequently, a device with higher capacitance can be achieved. These two merit features are attributed to the ordered graphitic domains existing in carbonized PAN structures. Since the SA of nanostructured film has 4 times higher than that of the planar one, more crystalline domains are exposed to the electrolyte, which facilitates better ion diffusion and ion adsorption not only at the surface of the carbon nanopillars but within the nanostructured electrode as well. Moreover, we observed a small voltage drop of 0.0017 V for the NSD compared to 0.04 V for PLD, indicating that the NSD has a lower equivalent series resistance (ESR) compared to the PLD. Owing to its lower ESR value, substantial enhancements in energy densities as well as power densities were observed in NSD over PLD (Figure 4.3f). The peak power density for NSD is calculated to be ~0.012 W/cm^3, with a corresponding energy density of ~1.37×10^{-6} Wh/cm^3. Both the power density and energy density of NSD is an order of magnitude higher than that of PLD. Compared to various carbon thin film energy storage devices,[5-7, 11, 31] the energy density of NSD in aqueous electrolyte is lower than that of other devices while the power density is comparable to prior reported data (Figure 4.3f). This is expected because the current collectors used in those studies were either a noble metal (i.e. Au) or graphene, which possess a much higher electrical conductivity than our carbonized PAN films. To improve the performance of our devices, we extended the voltage window to 3V (ionic liquid electrolyte). We were able to achieve an energy density of ~9.4×10^{-4} Wh/cm^3 with a corresponding power density of 1.48 W/cm^3, which is in the same range with the aforementioned reports.

4.5 Conclusion

In summary, we have successfully demonstrated a simple, cost effective and highly reproducible SNAP technique to print carbon nanostructures from PAN polymer precursor. This is accomplished by making use of the liquid nature of a polymer precursor, which directly eliminates the requirement of high temperature and pressure in typical NIL technique. Additionally, we also presented a highly efficient carbonization process that can convert printed PAN pillars to nanostructured carbon by laser irradiation reducing the time required for developing nanostructured carbon from several hours to a few minutes. The electrochemical results show that enhancement in surface area of the nanopatterns can improve the capacitance of the supercapacitor device by one to two orders of magnitude. Moreover, the simple casting and transferring steps involved in making the nanostructures reveal the potential to fabricate large area printed nanostructures by simply printing the structures side-by-side. These promising results indicate that this technique has great prospects in the fabrication of individual electrochemical devices as well as miniaturized integrated nanocomposite energy-storage systems (like supercapacitor-battery hybrid devices).

4.6 References

1. H. Nishihara and T. Kyotani, *Adv. Mater.*, 2012, **24**, 4473-4498.

2. L. L. Zhang, R. Zhou and X. S. Zhao, *J. Mater. Chem.*, 2010, **20**, 5983-5992.

3. A. K. Mishra and S. Ramaprabhu, *J. Phys. Chem. C*, 2011, **115**, 14006-14013.

4. J. R. Miller, R. A. Outlaw and B. C. Holloway, *Science*, 2010, **329**, 1637-1639.

5. M. F. El-Kady, V. Strong, S. Dubin and R. B. Kaner, *Science*, 2012, **335**, 1326-1330.

6. J. J. Yoo, K. Balakrishnan, J. S. Huang, V. Meunier, B. G. Sumpter, A. Srivastava, M. Conway, A. L. M. Reddy, J. Yu, R. Vajtai and P. M. Ajayan, *Nano Lett.*, 2011, **11**, 1423-1427.

7. W. Gao, N. Singh, L. Song, Z. Liu, A. L. Reddy, L. Ci, R. Vajtai, Q. Zhang, B. Wei and P. M. Ajayan, *Nat. Nanotechnol.*, 2011, **6**, 496-500.

8. Z. Chen, V. Augustyn, J. Wen, Y. W. Zhang, M. Q. Shen, B. Dunn and Y. F. Lu, *Adv. Mater.*, 2011, **23**, 791-795.

9. Y. P. Zhai, Y. Q. Dou, D. Y. Zhao, P. F. Fulvio, R. T. Mayes and S. Dai, *Adv. Mater.*, 2011, **23**, 4828-4850.

10. C. Portet, G. Yushin and Y. Gogotsi, *Carbon*, 2007, **45**, 2511-2518.

11. D. Pech, M. Brunet, H. Durou, P. H. Huang, V. Mochalin, Y. Gogotsi, P. L. Taberna and P. Simon, *Nat. Nanotechnol.*, 2010, **5**, 651-654.

12. Z. Chen, J. Wen, C. Z. Yan, L. Rice, H. Sohn, M. Q. Shen, M. Cai, B. Dunn and Y. F. Lu, *Advanced Energy Materials*, 2011, **1**, 551-556.

13. C. L. Wang and M. Madou, *Biosens. Bioelectron.*, 2005, **20**, 2181-2187.

14. T. Kyotani, N. Sonobe and A. Tomita, *Nature*, 1988, **331**, 331-333.

15. C. R. Martin, *Science*, 1994, **266**, 1961-1966.

16. R. Ryoo, S. H. Joo and S. Jun, *J. Phys. Chem. B*, 1999, **103**, 7743-7746.

17. J. Lee, S. Yoon, T. Hyeon, S. M. Oh and K. B. Kim, *Chem. Commun.*, 1999, DOI: 10.1039/A906872d, 2177-2178.

18. Z. X. Ma, T. Kyotani and A. Tomita, *Chem. Commun.*, 2000, DOI: 10.1039/B006295m, 2365-2366.

19. H. Nishihara, Q. H. Yang, P. X. Hou, M. Unno, S. Yamauchi, R. Saito, J. I. Paredes, A. Martinez-Alonso, J. M. D. Tascon, Y. Sato, M. Terauchi and T. Kyotani, *Carbon*, 2009, **47**, 1220-1230.

20. S. Y. Chou, P. R. Krauss and P. J. Renstrom, *Appl. Phys. Lett.*, 1995, **67**, 3114-3116.

21. L. J. Guo, *J. Phys. D-Appl. Phys.*, 2004, **37**, R123-R141.

22. V. Penmatsa, H. Kawarada and C. Wang, *J. Micromech. Microeng.*, 2012, **22**, 045024.

23. T. H. Ko, *J. Appl. Polym. Sci.*, 1991, **43**, 589-600.

24. M. S. A. Rahaman, A. F. Ismail and A. Mustafa, *Polym. Degrad. and Stabil.*, 2007, **92**, 1421-1432.

25. S. K. Nataraj, K. S. Yang and T. M. Aminabhavi, *Prog. Polym. Sci.*, 2012, **37**, 487-513.

26. P. Simon and Y. Gogotsi, *Nat. Mater.*, 2008, **7**, 845-854.

27. Y. Hirai, T. Yoshikawa, M. Morimatsu, M. Nakajima and H. Kawata, *Microelectron. Eng.*, 2005, **78-79**, 641-646.

28. Z. N. Yu, B. Duong, D. Abbitt and J. Thomas, *Adv. Mater.*, 2013, **25**, 3302-3306.

29. B. Duong, P. Gangopadhyay, J. Brent, S. Seraphin, R. O. Loutfy, N. Peyghambarian and J. Thomas, *ACS Appl. Mater. Interfaces*, 2013, **5**, 3894-3899.

30. M. D. Stoller and R. S. Ruoff, *Energ. Environ. Sci.*, 2010, **3**, 1294.

31. H. Y. Jung, M. B. Karimi, M. G. Hahm, P. M. Ajayan and Y. J. Jung, *Sci. Rep.*, 2012, **2**, 773.

32. D. N. Futaba, K. Hata, T. Yamada, T. Hiraoka, Y. Hayamizu, Y. Kakudate, O. Tanaike, H. Hatori, M. Yumura and S. Iijima, *Nat. Mater.*, 2006, **5**, 987-994.

33. B. E. Conway, *Electrochemical supercapacitors: scientific, fundamentals and technological applications*, Plenum, New York, 1999.

5 FABRICATION OF SYMMETRIC SUPERCAPACITORS WITH MnO_2 NANOWHISKERS*

5.1 Introduction

As mentioned in Chapter 3, depositing active materials onto a nanostructured current collector is a very promising approach to achieve high-performance supercapacitors. Although the SNAP technique can easily and quickly print nanostructured electrodes, it is still a challenge to fabricate nanostructured electrodes with large area, template-free, and high aspect ratio arrays without nanostructures clumping together. Here we developed a large area, template-free, high aspect ratio, and freestanding CuO@AuPd@MnO_2 core-shell nanowhiskers (NWs) design. Our electrochemical measurements show that these CuO@AuPd@MnO_2 NWs exhibit remarkable properties including high specific capacitance, excellent reversible redox reactions, and fast charge-discharge ability. Moreover, a novel coaxial supercapacitor cable (CSC) design which combines electrical conduction and energy storage by modifying the copper core used for electrical conduction was demonstrated. For accomplishing large surface area necessary for high supercapacitor performance, we developed NWs on the outer surface of the electrical conduction wire. The NWs structure is developed by just heating the inner core and therefore is practical to upscale the process to make extended lengths. An attractive advantage of using the coaxial design is that electricity can be conducted through the inner conductive metal wire and electrical energy can be stored in the nanostructured concentric layers added to this inner metal wire with an oxide layer in between. It is always a vital task for many applications including aviation to

---

* The work presented in this chapter has been published in Z. Yu, and J. Thomas, *Adv. Mater.* 2014, 26, 4279-4285 and Z. Yu, J. Moore, J. Lorenzo, C. Li, and J. Thomas, *ECS Trans.* 2014, 61, 31-36. Reproduction has been permitted by © 2014 WILEY and ECS.

find better methods to save weight and space, while maintaining the intended purpose. Therefore, integration of electrical cable and energy storage device into one unit offers a very promising opportunity to transmit electricity and store energy at the same time. In addition, CSC built from these NWs exhibits excellent flexibility and bendability, superior long-term cycle stability, and high power and energy densities. The development of this innovative lightweight, flexible, and space saving CSC makes it very attractive for many applications including hybrid and all-electric vehicles, electric trains, heavy machineries, aircrafts and military.

5.2 Fabrication of Electrodes

Fabrication method of electrode based on inner conductor involves three steps: (1) growth of CuO NWs from a pure copper wire by heat treatment; (2) deposition of a conducting metal layer by sputter-coating; (3) electrodeposition of active material onto the nanostructures (Figure 5.1a). CuO NWs can be easily grown on copper wire/foil by a simple heat treatment in air.[32] A pure copper wire/foil was cleaned in an acetone solution for 1 min, followed by washing with distilled (DI) water twice and drying by a nitrogen gas flow. The copper wire/foil was then placed in an alumina crucible (MTI Corporation, CA) and rapidly heated to 500 °C at a heating rate of 20 °C min^{-1} in a MTI Muffle furnace and kept for 4 h. Scanning electron microscope (SEM) image (Figure 5.1b) clearly shows that CuO NWs were grown uniformly on the Cu wire (diameter of ~0.37 mm) when heated at 500 °C for 4 hours. The average lengths of CuO NWs are ~ 15 μm and diameter is ~ 100 nm (Figure 5.1c). Prior to depositing active material, a thin layer of gold-palladium (AuPd; 60% Au: 40% Pd) was deposited onto the CuO NWs to serve as a current collector as well as an anode for electro-deposition of active material. Metal deposition is necessary since CuO is a poor conductor of electricity. This insulating effect of CuO is beneficial in limiting the current leakage from inner core to the outer supercapacitor. It can be noted that the surface of CuO NW became grainier after deposition of AuPd (Figure 1d). MnO_2 was then conformally electrodeposited onto these NWs (Figure 5.1e). MnO_2 active layer was deposited onto the conducting AuPd metal layer using an anodic electrodeposition method at constant current of 0.5 mA cm^{-2} for 3 – 48 min. The electrolyte of electrodeposition was prepared by mixing 0.01 M manganese acetate ($MnAc_2$) and 0.02 M ammonium acetate (NH4Ac) in a solvent containing 90 v/v% of DI water and 10 v/v% of dimethyl sulfoxide (DMSO).The detailed structure of CuO@AuPd@MnO_2 NWs was further examined by high-resolution transmission electron microscopy (HRTEM). Figure 5.1f shows a low-magnification TEM image of CuO@AuPd@MnO_2 NWs which agrees well with the SEM in Figure 5.1e. A HRTEM image was shown in Figure 5.1g, from which a thin MnO_2 film uniformly covering the surface of CuO NWs can be clearly identified. The inset of Figure 5.1g indicates the crystallinity of metal nanoparticles that were sputtered (with a fringe spacing of ~0.24 nm); while no clear fringe spacing was observed for the MnO_2 outer film, revealing the amorphous characteristic of MnO_2. A similar fabrication technique is used to make NW on a flexible copper foil. The thickness of the outer electrode is ~30 μm and vertically grown NWs can be clearly found on the inner side of the outer electrode.

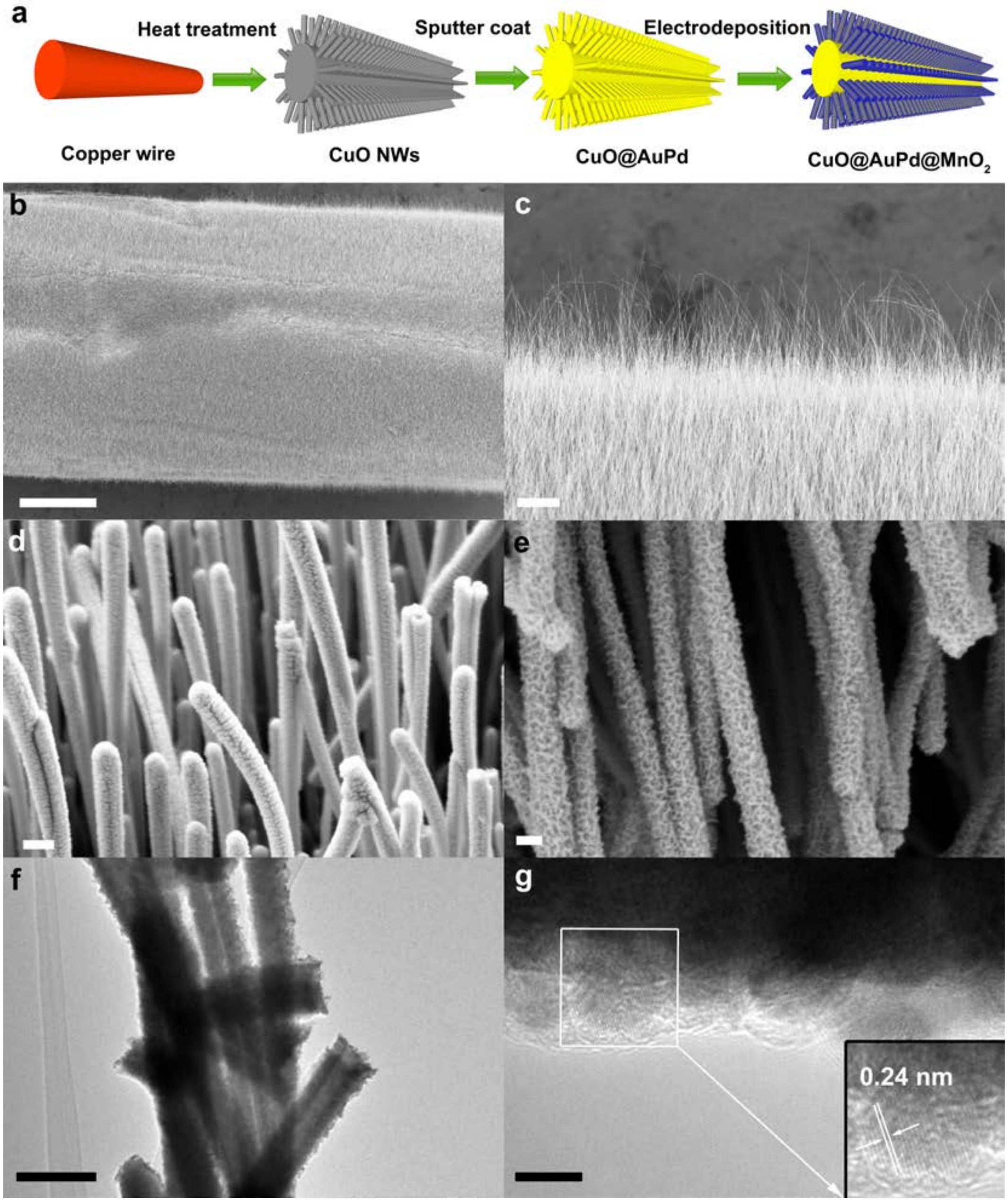

Figure 5.1 (a) Schematic illustration showing the fabrication process of CuO@AuPd@MnO_2 NWs. (b) Top view of SEM image shows that the copper wire is completely covered by CuO NWs. Scale bar, 100 μm. (c) Close-up view of SEM image showing vertically grown CuO NWs. Scale bar, 10 μm. (d) SEM image of AuPd nanoparticles that were conformally sputter-coated onto each NW. Scale bar, 300 nm. (e) SEM image of MnO_2 that was uniformly electrodeposited onto NWs. Scale bar, 200 nm. (f) Low-magnification TEM image of CuO@AuPd@MnO_2 NWs. Scale bar, 200 nm. (g) HRTEM image of CuO@AuPd@MnO_2 NW. Scale bar, 5 nm. The inset is the enlarged HRTEM image of the rectangular area.

5.3 Fabrication of Devices

The gel electrolyte was prepared by dissolving 5.6 g KOH and 10 g PVA in 100 mL DI water. The whole mixture was heated at 90 °C under stirring until all the solute completely dissolves in the solvent. The viscous electrolyte solution was carefully coated onto the MnO_2 deposited area of both inner and outer electrodes with a working length of 1 cm. The outer electrode was then tightly surrounded onto the inner electrode with an ion porous separator (Celgard 3501, NC, 25 μm) in between. After the PVA-KOH gel electrolyte solidified at room temperature, a solid-state CSC was prepared.

5.4 Characterization and Measurements

Surface morphologies were characterized by means of scanning electron microscopy (SEM, ZEISS Ultra 55) and transmission electron microscopy (TEM, TECNAI F30) equipped with an energy-dispersive X-ray spectroscopy (EDS). To investigate the chemical compositions of sample surface, X-ray photoelectron spectroscopy (XPS, PHI 5400) was performed. To compare the electrochemical performance of different materials, a three-electrode system consisting of a working electrode (electrode prepared based on the materials as-synthesized), a platinum counter electrode and a saturated calomel electrode (SCE) as reference electrode was used. Cyclic voltammetry (CV) and galvanostatic charge-discharge (GCD) measurements were performed using this three-electrode configuration in 1M KOH solution on an electrochemical workstation (Bio-Logic, SP-150). The characterization experiments of the devices using solid electrolyte were conducted by a two-electrode system in air at a voltage range of 0 – 0.8 V. Electrochemical impedance spectroscopy (EIS) measurements were performed by applying an

AC voltage with 5 mV amplitude in a frequency range from 10 mHz to 100 kHz. All the calculations including specific capacitance as well as energy and power densities are discussed in detail in the supplementary information.

5.5 Performance Evaluation of the Electrodes/Devices Based on MnO_2 Nanowhiskers

To evaluate the electrochemical properties of $CuO@AuPd@MnO_2$ NWs, cyclic voltammetry (CV) measurements were performed using a three-electrode system in 1M KOH solution. In comparison, pure CuO NWs and CuO@AuPd NWs were also studied using CV measurements. CV curve of $CuO@AuPd@MnO_2$ NWs has much higher current compared to pure CuO and CuO@AuPd NWs, revealing $CuO@AuPd@MnO_2$ has the best supercapacitive behavior (Figure 5.2a). CV curves of $CuO@AuPd@MnO_2$ NWs at different scan rates ranging from 5 to 100 mV s^{-1} were also performed and shown in Figure 5.2b. All the CV curves are close to a symmetrical rectangle-like shape, indicating good electrochemical performance of $CuO@AuPd@MnO_2$ NWs. Different mass loading of MnO_2 were also studied by varying the deposition time ranging from 3 to 48 min. All the CV curves of different deposition time show good rectangularity (Figure 5.2c), implying the good capacitive behavior of the electrodes. The specific capacitance for 3, 6, 12, 24, 48 min deposition of MnO_2 was 1,376, 702, 562, 561, and 493 F g^{-1} (based on MnO_2), respectively, at a scan rate of 5 mV s^{-1} (Figure 5.2d). Calculation of specific capacitance is based on subtraction of the capacitance which belongs to the AuPd from the total capacitance. The highest specific capacitance of 1,376 F g^{-1} was obtained for a 3 min deposition of MnO_2 (mass loading of 0.04 mg cm^{-2}). This value is much higher than other MnO_2 based nanostructures, such as $SnO_2@MnO_2$ nanowires (637 F g^{-1} at 2 mV s^{-1}, 0.08 mg cm^{-2}),[2] AuPd@MnO_2 nanopillars (603 F g^{-1} at 5 mV s^{-1}, 0.01 mg cm^{-2}),[3] WO_{3-x}@Au@MnO_2 nanowires (588 F g^{-1} at 10 mV s^{-1}, 0.04 mg cm^{-2}),[4] TiN/MnO_2 nanotubes (486 F g^{-1} at 2 mV s^{-1}, 0.06 mg cm^{-2}),[5] C@MnO_2 nanorods (302 F g^{-1} at 5 mV s^{-1}, 0.072 mg cm^{-2}),[6] and Zn_2SnO_4@MnO_2 nanorods (621.6 F g^{-1} at 2 mV s^{-1}).[7] In addition, the specific capacitance of our electrode still remained at 493 F g^{-1} even at a higher loading mass of MnO_2 (0.55 mg cm^{-2}). The specific capacitance of electrodes with a deposition time of 3 min show consistent enhancement of up to 2 times than those with longer deposition times by varying the scan rate from 5 to 100 mV s^{-1} (Figure 5.2e). This implies that the elongating deposition times may lead to an increase in thickness of active material, but the condensed packing will result in surface area overlap of MnO_2. In this case, the whole surface area of MnO_2 cannot be fully charged or discharged.

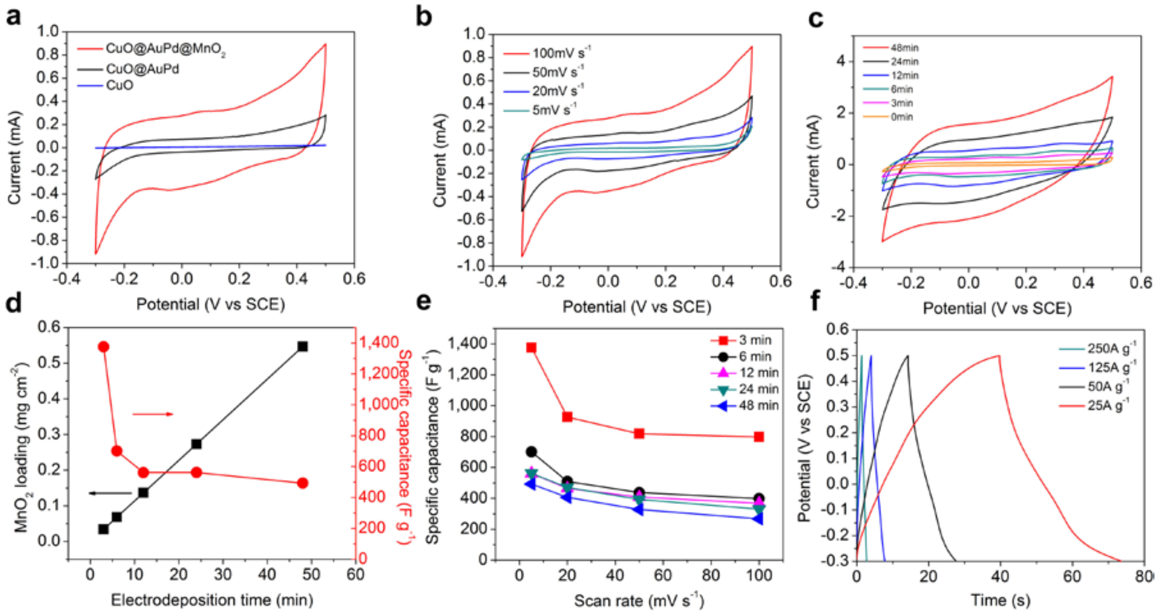

Figure 5.2 (a) CV curves of CuO@AuPd@MnO_2 NWs compared to pure CuO NWs and CuO@AuPd NWs at a scan rate of 100 mV s^{-1} in 1M aqueous KOH electrolyte. (b) CV curves of CuO@AuPd@MnO_2 NWs at different scan rates (5 – 100 mV s^{-1}). (c) CV curves of CuO@AuPd@MnO_2 NWs at a scan rate of 100 mV s^{-1} with different MnO_2 deposition time of 0, 3, 6, 12, 24, and 48 min, respectively. (d) MnO_2 loading and specific capacitance at a scant rate of 5 mV s^{-1} of CuO@AuPd@MnO_2 NWs as a function of electrodeposition time. (e) Specific

capacitance of CuO@AuPd@MnO_2 NWs at different MnO_2 electrodeposition times as a function of scan rate. (f) GCD curves of CuO@AuPd@MnO_2 NWs at different current densities (25 – 250 A g^{-1}).

To further evaluate the charge-discharge storage capacity of our electrodes, galvanostatic charge-discharge (GCD) measurements were performed using the same three-electrode configuration system as the CV measurements. GCD curves of the CuO@AuPd@MnO_2 NWs at different current densities (25 – 250 A g^{-1}) show linear and symmetrical charge and discharge profiles (Figure 5.2f), indicating good supercapacitve behavior of these NWs.

A solid state CSC is simply fabricated by placing the outer tubular electrode onto the inner electrode (both pre-coated with gel electrolyte) where the two electrodes are separated by an ion porous separator (Figure 5.3a). CV measurements were also performed to test the flexibility and bendability of CSC. Figure 5.3b shows the CV curves of our device tested under different bending angles ranging from 0 to 180 degrees. The shapes of all four CV curves are almost identical to one another, indicating the good flexibility of our device. Moreover, the rectangular and symmetrical shape of the CV curves exhibits ideal pseudocapacitive nature of MnO_2 and superior reversible redox reaction. A bend test of our devices was also carried out by folding the device at different angles up to 100 times. The supercapacitor device remained at 93.4% of its initial capacitance even after folding at 180 degree for 100 times (Figure 5.3c), revealing the excellent bendability of our device. To further evaluate the electrochemical performance of our device, GCD measurements were performed. Figure 5.3d exhibits the GCD curves at various current densities ranging from 0.087 to 3.472 A cm^{-3}. The charge-discharge curves are symmetric and linear in nature, which further confirms the good electrochemical capacitive characteristics and fast charging-discharging process characteristics of CSC. The electrochemical performance of CSC is further evaluated using EIS with frequency ranging from 10 mHz to 100 kHz. The Nyquist plots (Figure 5.3e) shows a straight line which indicates an ideal capacitive behavior of CSC. Moreover, the resistance of the device is very close to the intercept of the Nyquist curve on the real axis (the inset of Figure 5.3e), demonstrating the low internal resistivity of the electrode and good conductivity of the electrolyte. Figure 5.3f displays the Bode plots of the CSC. The phase angle is close to -90° for frequency up to 5 Hz, suggesting an ideal capacitor is approached for CSC. The relaxation time (59 ms) is calculated based on the frequency (17 Hz) that possesses a phase angle of -45° at which point that the capacitive and resistive impedances are equal.[8] The fast frequency response may attribute to the large and accessible surface area of the CSC. This exceptional tiny time constant for the CSC shows very competitive potential compared with other reported values for supercapacitors such as activated carbon (700 ms),[9] MnO_2/carbon composite (500 ms),[6] PEDOT/CNT (80 ms),[10] graphene (19 ms),[11] onion-like carbon (26 ms),[9] etc.

Good cycling performance is one of the vital characteristics for energy storage devices. Figure 5.4a shows the long-term cycle stability of CSC at a scan rate of 100 mV s^{-1}. The capacitance still remains at 99% of its initial value after 5,000 cycles, revealing excellent cycle stability. Energy density and power density are the other two important parameters to characterize the performance of energy storage devices. Figure 4b presents the volumetric power and energy densities of the solid electrolyte based CSC. The average volumetric energy density is 0.55 mWh cm^{-3} with a volumetric power density of 413 mW cm^{-3}. These results are substantially higher than that of the recently reported all-solid-state supercapacitors (SCs), such as ZnO@MnO_2-SCs (0.018 mWh cm^{-3} and 9 mW cm^{-3}, PVA-LiCl),[12] carbon nanotube SCs

(CNT-SCs, 0.02 mWh cm^{-3} and 20 mW cm^{-3}, PVA-H_3PO_4),[13] TiN SCs (0.05 mWh cm^{-3} and 150 mW cm^{-3}, PVA-KOH),[5] Graphene-SCs (0.06 mWh cm^{-3} and 200 mW cm^{-3}, PVA-H_3PO_4),[14] MnO_2/carbon-nanoparticles SCs (MnO_2/CNPs-SCs, 0.12 mWh cm^{-3} and 200 mW cm^{-3}, PVA-H_3PO_4),[6] TiO_2@MnO_2 and TiO_2@C asymmetric SCs (TiO_2@MnO_2//TiO_2@C-SCs, 0.15 mWh cm^{-3} and 230 mW cm^{-3}, PVA-LiCl),[15] and Co_9S_8//Co3O4@RuO_2-SCs (0.22 mWh cm^{-3} and 520 mW cm^{-3}, PVA-KOH).[16]

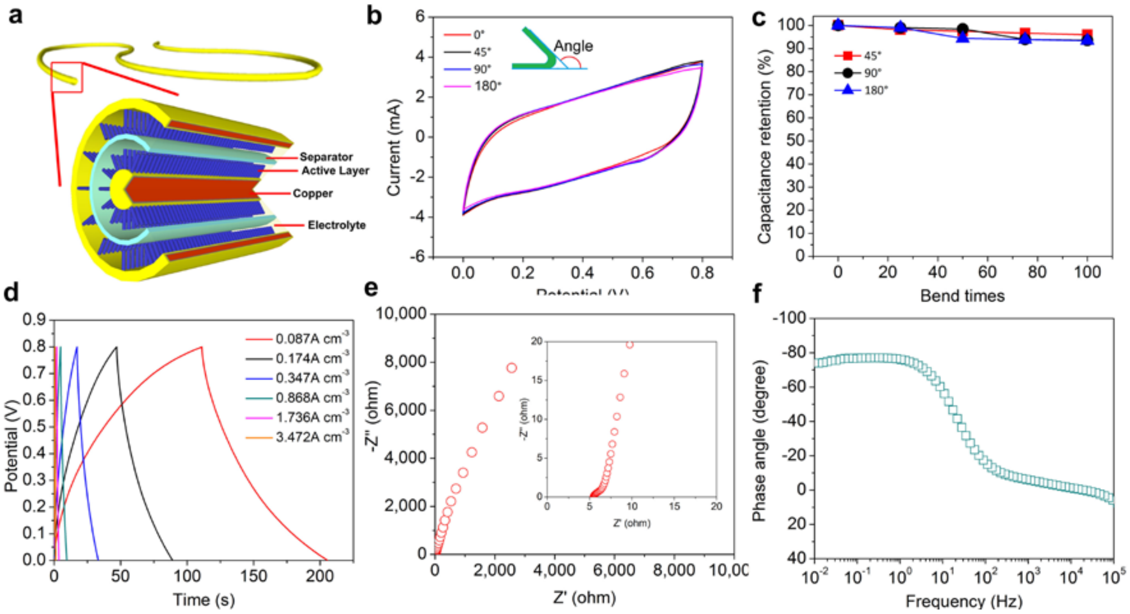

Figure 5.3 (a) A schematic diagram of CSC using solid electrolyte. (b) Subtle changes of CV curves collected at a scan rate of 100 mV s^{-1}, under different bending angles ranging from 0 – 180°. (c) Bending the device up to 100 times at different bending angles showing excellent bendability of our devices. (d) GCD curves of device at different current densities. (e) Nyquist plots of the CSC. (f) Bode plots of the CSC.

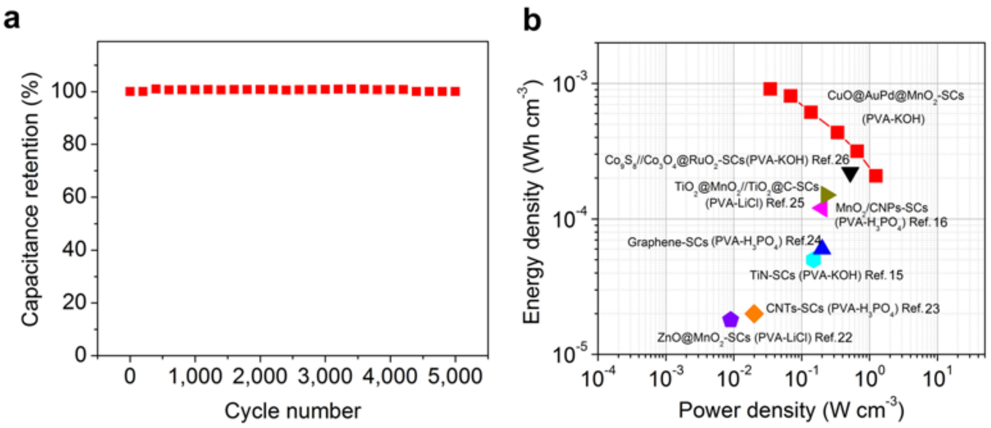

Figure 5.4 (a) Cycle performance of the device at a scan rate of 100 mV s^{-1} for 5,000 cycles. (b) Power and energy densities of the device.

Superior electrochemical performance of CSC may attribute to three factors. First, surface area of each electrode is significantly enhanced by nanoarchitecturing, which provides much more electrochemical-active sites for the reversible redox reactions. As shown in Figure 5.1b and c, CuO NWs were vertically grown on the copper wire, which increases the surface area immensely compared to a smooth surface of copper wire (more than 2 orders of magnitude enhancement). After depositing active material onto this nanostructure, more electrochemically active sites will be used during charge-discharge process compared to a non-nanostructured surface. This results in substantial improvements of electrochemical properties. Second, NW structure provides more open space, which facilitates the accessibility of electrolyte. As shown in Figure 5.1e, MnO$_2$ was conformly coated onto NWs and each NW is completely separated without touching each other, which enables the electrolyte to access the MnO$_2$ from the bottom site of each NW. Third, the internal resistance is sharply reduced by the large and binder-free contact area between AuPd and MnO$_2$. When depositing MnO$_2$ onto a non-nanostructured surface, the condensed packing of MnO$_2$ will block electrons from reaching the first layer of

MnO_2, whereas the path for electron transport will be significantly shortened through the use of a nanostructured design.

5.6 Conclusion

In summary, CuO@AuPd@MnO_2 core-shell NWs as electrode of the energy storage part of CSC exhibits excellent electrochemical properties, in which case a specific capacitance of 1,376 F g^{-1} was obtained at a scan rate of 5 mV s^{-1}. Moreover, CSC base on CuO@AuPd@MnO_2 NWs show extraordinary flexibility and bendability, 99.6% capacitance retention (even after 5,000 cycles), and high power and energy densities (0.55 mWh cm^{-3} and 413 mW cm^{-3}). All these results demonstrate that CSC can have high impact on the future energy storage applications.

5.7 References

1. X. Jiang, T. Herricks and Y. Xia, *Nano Lett.*, 2002, **2**, 1333-1338.
2. J. Yan, E. Khoo, A. Sumboja and P. S. Lee, *ACS Nano*, 2010, **4**, 4247-4255.
3. Z. Yu, B. Duong, D. Abbit and J. Thomas, *Adv. Mater.*, 2013, **25**, 3302-3306.
4. X. Lu, T. Zhai, X. Zhang, Y. Shen, L. Yuan, B. Hu, L. Gong, J. Chen, Y. Gao, J. Zhou, Y. Tong and Z. L. Wang, *Adv. Mater.*, 2012, **24**, 938-944.
5. X. Lu, G. Wang, T. Zhai, M. Yu, S. Xie, Y. Ling, C. Liang, Y. Tong and Y. Li, *Nano Lett.*, 2012, **12**, 5376-5381.
6. L. Yuan, X. H. Lu, X. Xiao, T. Zhai, J. Dai, F. Zhang, B. Hu, X. Wang, L. Gong and J. Chen, *ACS Nano*, 2012, **6**, 656-661.

7. L. Bao, J. Zang and X. Li, *Nano Lett.*, 2011, **11**, 1215-1220.

8. P. Taberna, P. Simon and J.-F. Fauvarque, *J. Electrochem. Soc.*, 2003, **150**, A292-A300.

9. D. Pech, M. Brunet, H. Durou, P. Huang, V. Mochalin, Y. Gogotsi, P.-L. Taberna and P. Simon, *Nat. Nanotechnol.*, 2010, **5**, 651-654.

10. J. A. Lee, M. K. Shin, S. H. Kim, H. U. Cho, G. M. Spinks, G. G. Wallace, M. D. Lima, X. Lepró, M. E. Kozlov and R. H. Baughman, *Nat. Commun.*, 2013, **4**, 1970.

11. M. F. El-Kady and R. B. Kaner, *Nat. Commun.*, 2013, **4**, 1475-1473.

12. P. Yang, X. Xiao, Y. Li, Y. Ding, P. Qiang, X. Tan, W. Mai, Z. Lin, W. Wu, T. Li, H. Jin, P. Liu, J. Zhou, C. P. Wong and Z. L. Wang, *ACS Nano*, 2013, **7**, 2617-2626.

13. M. Kaempgen, C. K. Chan, J. Ma, Y. Cui and G. Gruner, *Nano Lett.*, 2009, **9**, 1872-1876.

14. M. F. El-Kady, V. Strong, S. Dubin and R. B. Kaner, *Science*, 2012, **335**, 1326-1330.

15. X. Lu, M. Yu, G. Wang, T. Zhai, S. Xie, Y. Ling, Y. Tong and Y. Li, *Adv. Mater.*, 2013, **25**, 267-272.

16. J. Xu, Q. Wang, X. Wang, Q. Xiang, B. Liang, D. Chen and G. Shen, *ACS Nano*, 2013, **7**, 5453-5462.

6 FABRICATION OF ASYMMETRIC SUPERCAPACITORS WITH FUNCTIONALIZED GRAPHENE AEROGEL AND MnO_2[*]

6.1 Introduction

Bridging the properties of batteries and conventional capacitors, supercapacitors (SCs) are an emerging technology that fills a crucial gap in today's rapidly evolving energy storage needs. With desirable properties of high power density, fast charge-discharge rate, and excellent cycle stability [1-5], SCs can be used in a wide range of applications such as hybrid vehicles, portable electronics, pacemakers, etc. [6-9]. Improving the energy density of SCs is critical for widespread use. The energy density of a SC is calculated using the equation $E=1/2CV^2$, where E is the energy density, C is the cell capacitance, and V is the cell voltage [10, 11]. Obviously, the exponent of 2 in the above equation makes the cell voltage to play an essential and efficient role in enhancing energy density. There are two major approaches to broaden the cell voltage. One is to use organic or ionic liquid electrolytes which raise the voltage window up to 3 V [12, 13]. However, the toxicity, high-cost, and poor ionic conductivity of organic electrolytes and the limitation of working temperature of ionic liquid electrolytes make this approach unfavorable. Second is to develop aqueous electrolyte-based asymmetric supercapacitors (ASCs), which include a battery-type Faradic cathode as an energy source and a capacitor-type anode as a power source [14-16]. An ASC takes advantage of the different voltage windows of both the cathode and anode so that an enhanced operation voltage in a cell system can be readily achieved, resulting in an improved specific capacitance and substantially boosted energy density.

---

[*] The work presented in this chapter has been published in Z. Yu, M. McInnis, J. Calderon, S. Seal, L. Zhai, and J. Thomas, *Nano Energy* 2015, 11, 611-620. Reproduction has been permitted by © 2015 Elsevier.

Despite the considerable effort dedicated towards the development of cathode materials such as MnO_2 [17], NiO [18, 19], $Ni(OH)_2$ [20, 21], CoO_x [22], etc., less attention is focused on anode material development. Carbon-based materials commonly serve as an anode in ASCs including activated carbon [23, 24], carbon nanofiber [25], carbon nanotube (CNT) [26], graphene [27], etc. Among them, graphene has stood out due to its outstanding characteristics such as large surface area, solution processability, high electrical conductivity, excellent mechanical properties, and superior electrochemical stability [28-34]. However, a significant surface area loss is normally observed during processing because of the aggregation of graphene nanosheets [35-37], resulting in a reduced electrochemically active area which considerably limits the specific capacitance. A feasible approach is to fabricate graphene nanosheets into a graphene aerogel (GA); a stable 3D network which can effectively hamper the aggregation of graphene nanosheets [38-40]. The GA electrode's open 3D network structure provides maximal active surface area while the honeycomb structure (~10 µm pore diameter) facilitates effective electrolyte ion transportation [41]. One significant limitation is that the oxidation-reduction process lowers the electrical conductivity relative to pristine graphene due to defect site formation [29, 42]. Therefore, it is advantageous to fabricate a GA with enhanced electrical conductivity. Functionalization of the GA with metal nanoparticles increases the bulk electrical conductivity as the metal nanoparticles preferentially anchor at the otherwise electrical impeding defect sites [43], and lowers the work function of the composite [44].

Here we report a novel functionalized GA fabrication method of producing a high surface area electrode material (328 $m^2\ g^{-1}$) for ASCs. In this method, palladium (Pd) nanoparticles are introduced into the 3D network structure of GA (denoted as P-GA), which reduces the electrical resistivity from 950 to 16 Ω cm (more than 50 times improvement). Although Pd is a relatively expensive metal, it is environmentally and electrochemically stable, making it a potential candidate to improve the device performance. Electrodes prepared based on P-GA show high specific capacitance (175.8 F g^{-1} at 5 mV s^{-1}), excellent rate capability, superior coulombic efficiency, and remarkable reversibility. Moreover, ASCs assembled using this functionalized GA show stable extended cell voltage, fast charge-discharge capability, excellent cycle stability, and high energy and power densities. In addition, we have further demonstrated the applicability of our ASC in energy storage by lighting up a LED, highlighting the significant potential of our functionalized GA for high performance energy storage devices.

6.2 Preparation of Pd Salt-Loaded GO Aerogels

GO was prepared by modified Hummers method starting from graphite powder [45]. Briefly, graphite was oxidized using concentrated H_2SO_4 and $KMnO_4$ and the resulting GO was purified and isolated via successive centrifugation and dispersion cycles in water, then dried under vacuum. A 100 mM stock solution of ligated palladium ions was prepared by slowly adding 0.002 moles of palladium chloride ($PdCl_2$) into 20mL of a 100 mM ethylenediaminetetraacetic acid (EDTA) solution while stirring. This mixture was refluxed for 30 minutes to achieve dissolution and to degas the solvent, and was then used immediately after cooling to room temperature. After appropriate dilution of the metal ligand complex to the desired concentration with a total volume of 500 µL, 500 µL of a freshly sonicated (30 minutes Branson S-450D horn sonicator at 10% amplitude) 20 g/L suspension of GO was added and thoroughly mixed in a 1 cm x 1 cm plastic cuvette. Parafilm was used to seal the bottom, to better facilitate freezing. Each solution was then placed onto a block of dry ice and allowed to freeze fully (~20 minutes) before lyophilization. Lyophilization was carried out using a Labcono freeze drying chamber at 20 μbarr with the collector set at -52 °C. GA samples were prepared in an identical manner, except without addition of $PdCl_2$/EDTA solution. The GO aerogel loaded with Pd salt has a brown color, while the reduced P-GA exhibits a black sponge-like appearance. The 3D morphology of as-prepared GA is verified by scanning electron microscopy (SEM) characterization. An interconnected and well-defined 3D structure of graphene nanosheets with a porous nature can be easily observed in Figure 6.1b. From the enlarged image in Figure 6.1c, ripples and wrinkles are evidenced on the graphene nanosheets, which may have been caused by the high surface energy combined with the strain formed during the thermal reduction process [46].

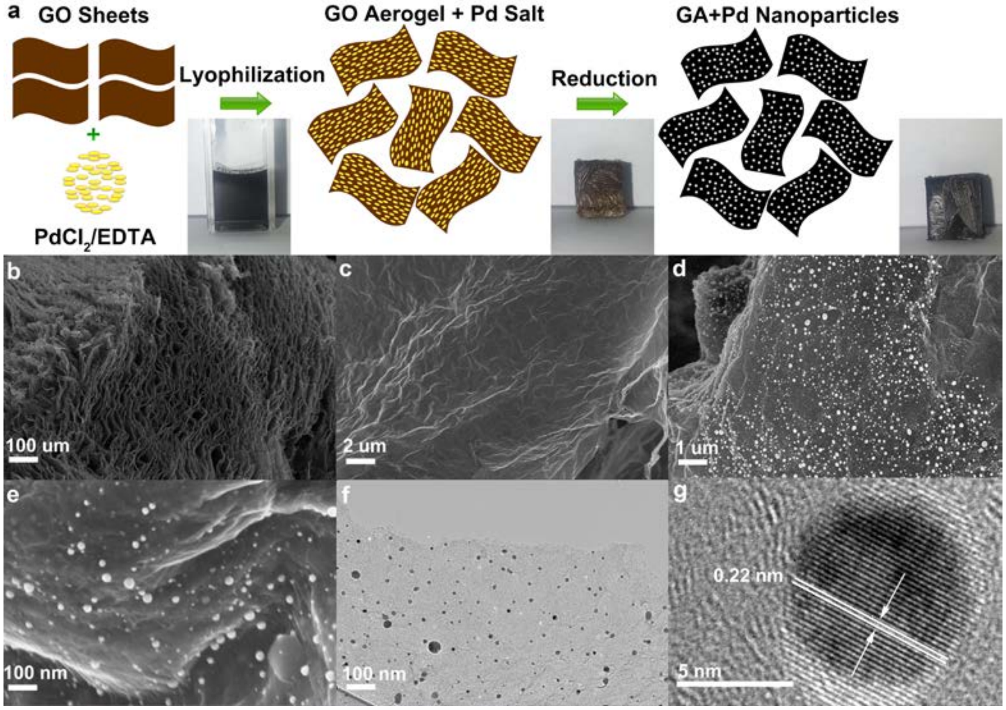

Figure 6.1 (a) Schematics illustration showing the fabrication process of P-GA. SEM images of the (b, c) GA and (d, e) P-GA. (f) TEM and (g) HRTEM images of P-GA.

6.3 Synthesis of Pd Nanoparticle Decorated GA

The freshly lyophilized light brown GO aerogels were first reduced using hydrazine hydrate. Samples were placed under flowing nitrogen environment for 1 hour, then the nitrogen flow was passed through a solution of hydrazine monohydrate to provide an atmosphere saturated with hydrazine vapor. After 0.5 hours at room temperature, the vessel was heated in an oil bath at 30°C/hr to 90°C and held at this temperature for 1 hour. The hydrazine vapor was purged with pure nitrogen gas while the system cooled to room temperature. To further reduce the GO and Pd ions, the samples were placed in a furnace under the flow of hydrogen gas and were first heated to 400 °C for 60 min for the formation of GA and further heated to 900 °C for 10 min for the formation of Pd nanoparticles. As displayed in Figure 6.1d, Pd nanoparticles were embedded onto GA with a uniform dispersion. The specific surface area and volumetric surface area of GA are 947 m^2g^{-1} and 1.48 m^2 cm^{-3}, respectively. For P-GA, the specific surface area decreases to 328 m^2 g^{-1} due to the high density of Pd, while the volumetric surface area increases to 8.31 m^2 cm^{-3} due to an enhancement of the surface roughness. The electrical resistivity is decreased from 950 Ω cm to 16 Ω cm when samples are loaded with Pd nanoparticles. This is due to the fact that defect sites on the GO act as anchors for nanoparticle formation [43], effectively bridging insulating areas. This, as well as the well-known effect that the metal nanoparticles are able to lower the composite's work function [44], which produces higher electrical conductivity, and therefore improved capacitance as charge more efficiently travels though the electrode.

The size of the Pd nanoparticles ranges from a few nanometers to several dozens of nanometers (Figure 6.1e). The uniform dispersion and size distribution of Pd nanoparticles are further demonstrated by transmission electron microscopy (TEM) as shown in Figure 6.1f. A high resolution TEM is provided in Figure 6.1g to examine the crystallinity of Pd nanoparticles. The fringe spacing of the particle lattice is 0.22 nm, which agrees well with the (1 1 1) lattice spacing of face-centered cubic (fcc) Pd (0.224 nm).

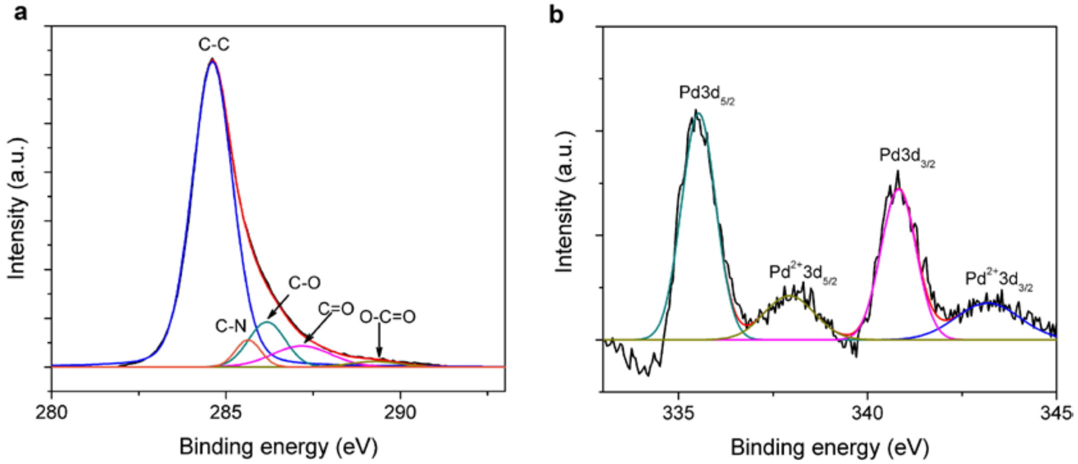

Figure 6.2 XPS spectra of (a) C1s and (b) Pd 3d with deconvolution.

The chemical composition of P-GA was analyzed using X-ray photoelectron spectroscopy (XPS) in Figure 6.2. Deconvoluted C 1s spectra shows five peaks which correspond to sp^2 C – C bonds of graphene at 284.6 eV, alcohol, phenolic, and ether C – O bonds at 286.2 eV, carbonyl C = O bonds at 287.2 eV, carboxyl O = C – O bonds at 289.3 eV, and carbonitride C – N bonds at 285.6 eV (Figure 6.2a) [38, 40]. The presence of C – N bonds may attribute to either a residual product of EDTA or the hydrazine reduction process. The efficient reduction of GO is evidenced in the XPS spectrum where the contribution of the C-C signal makes up most of the total C1s signal. The binding energies of 335.5 eV and 340.8 eV correspond to Pd $3d_{5/2}$ and Pd $3d_{3/2}$ for the metallic Pd^0, respectively (Figure 6.2b) [47], further confirm the presence of metallic Pd. Additionally, Pd^{2+} binding energies at 343.2 eV and 337.9 eV were also observed, which is likely due to surface oxides on the Pd nanoparticles.

6.4 Fabrication of Electrodes and ASCs

An anode was prepared by placing the P-GA (pre-cut and pressed into small slices) onto a nickel substrate with silver paste (SPI 05001-AB) in between in order to form ohmic contact. A cathode was prepared by anodic electrodepositing MnO_2 onto a nickel substrate at a constant current of 0.5 mA cm^{-2}. The electrolyte for the deposition was prepared by dissolving 0.01M manganese acetate ($MnAc_2$) and 0.02 M ammonium acetate (NH_4Ac) in a solvent mixture of 90% DI water and 10% dimethyl sulfoxide (DMSO). The ASCs were assembled by sandwiching the cathode and anode with a separator (Celgard 3501, NC) in between. A 0.1 M sodium sulfate (Na_2SO_4) solution was employed as the electrolyte.

6.5 Materials Characterization and Electrochemical Measurements

Morphologies were examined using scanning electron microscopy (SEM) and chemical compositions were investigated using X-ray photoelectron spectroscopy (XPS). Cyclic voltammetry (CV), galvanostatic charge-discharge (GCD), and electrochemical impedance spectroscopy (EIS) characteristics were tested using an electrochemical workstation (Bio-Logic, SP-150). EIS measurements were carried out by applying an AC voltage at 5 mV amplitude with different frequencies (10 mHz to 100 kHz). To study the electrochemical properties of individual electrodes (half-cell test), a three-electrode system was used, including a working electrode, a platinum plate as counter electrode, and a saturated calomel electrode (SCE) as reference electrode. For the ASCs (full-cell) test, a two-electrode configuration was directly connected to the cathode and anode of an ASC.

6.6 Performance Evaluation of Electrodes/Devices

As the aerogel structure provides highly enhanced surface area and Pd nanoparticles improve the electrical conductivity, we have tested P-GA as an electrode material for SCs. The electrochemical studies for the individual electrodes were conducted in a three-electrode configuration in 0.1 M sodium sulfate (Na_2SO_4) electrolyte, with a platinum counter electrode and a saturated calomel electrode (SCE) reference electrode. The Pd content is optimized in this study. Figure 3a shows the CV collected for P-GA and GA electrodes at a scan rate of 50 mV s^{-1}. The P-GA electrode exhibited much higher current density than GA electrode, indicating better electron transportation. Figure 3b shows the CV of P-GA electrode at different scan rates (5 – 500 mV s^{-1}) with a negative voltage window ranging from -0.8V to 0 V. The consistency of these box-like curves at different scan rates suggests the excellent capacitive behavior of P-GA electrode. Figure 3c shows the specific capacitances and rate performance of P-GA electrode at various scan rates. The highest specific capacitance obtained for the P-GA electrode was 175.8 F g^{-1} at a scan rate of 5 mV s^{-1}, which is much higher than the value obtained for the GA electrode (51.9 F g^{-1} at 5 mV s^{-1}) and other previously reported carbon aerogel based electrodes [48-50]. Moreover, the P-GA electrode shows excellent rate capability, with retention of 48.3% of the initial capacitance as the scan rate increases from 5 to 500 mV s^{-1}. Galvanostatic charge-discharge (GCD) curves collected for the P-GA electrode is shown in Figure 3d. The consistent observation of symmetrical GCD curves at different current densities implies the superior coulombic efficiency and great reversibility of the P-GA electrode. The above data demonstrate that the P-GA electrodes have giant advantages as potential candidates for high-performance negative electrodes.

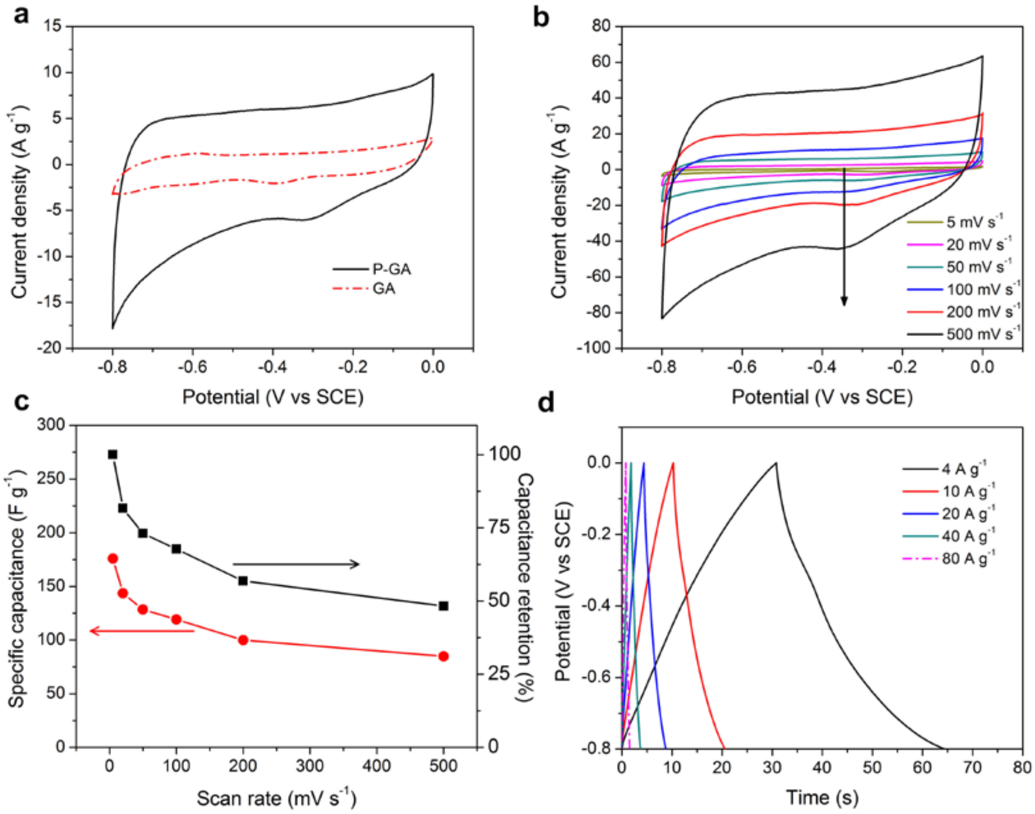

Figure 6.3 (a) CV curves of P-GA and GA electrodes at a scan rate of 50 mV s^{-1}. (b) CV curves of P-GA electrode at different scan rates (5 – 500 mV s^{-1}). (c) Specific capacitance and capacitance retention for the GA electrode as a function of scan rates. (d) GCD curves of P-GA electrode at different current densities (4 – 80 A g^{-1}).

At the same time, an electrode based on MnO_2 was selected as potential cathode for our study. CV of MnO_2 electrode was carried out with a positive voltage window ranging from 0V to 0.8V. The CV curves present consistent box-like shapes as the scan rate increases from 5 to 500 mV s^{-1}, implying excellent capacitive properties of MnO_2 electrode. Figure 4a presents the CV curves of both P-GA and MnO_2 electrodes at a scan rate of 50 mV s^{-1}. The two rectangular shaped CV curves occupy a voltage window from -0.8 V to 0.8V, implying an ASC device assembled from these two electrode could have a potential voltage window of 1.6 V. Specific capacitances of MnO_2 and P-GA at 50 mV s^{-1} are 243.7 and 128.5 F g^{-1} separately. The different specific capacitance of P-GA and MnO_2 electrodes will lead to a mismatching of charges stored. In order to keep the charge balance (q+=q-), loading mass of active material from cathode and anode should be adjusted and kept at a constant ratio of ~ 0.53.

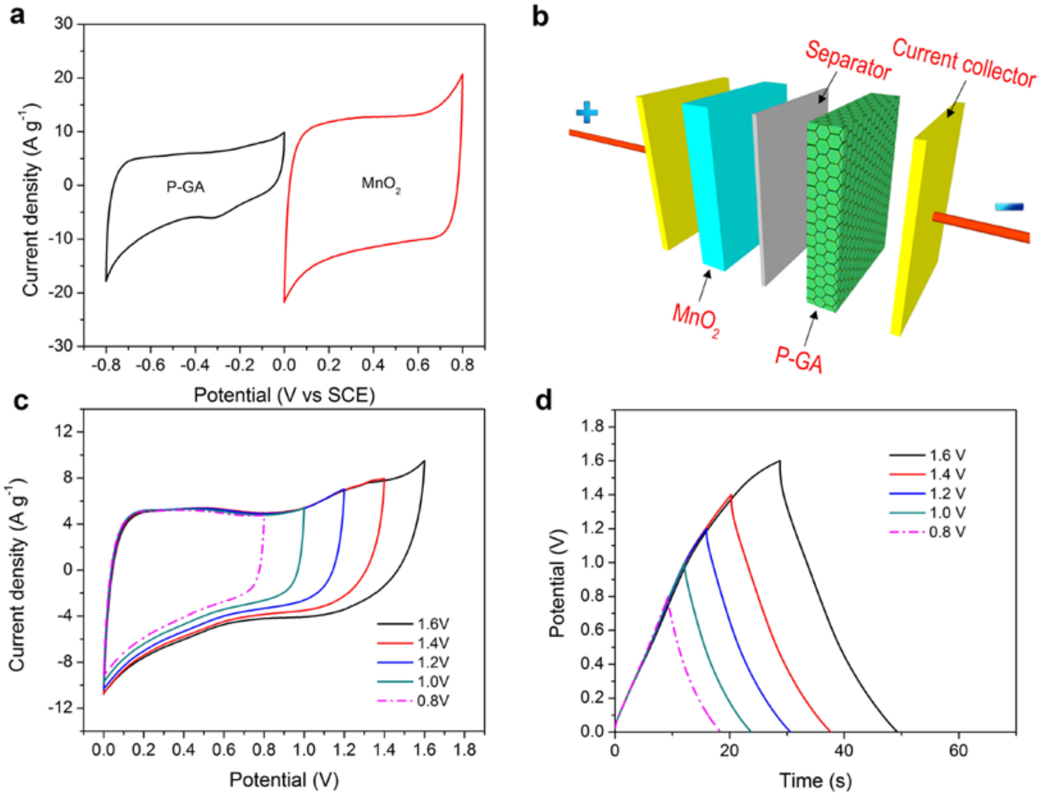

Figure 6.4 (a) Comparative CV curves of MnO_2 and P-GA electrodes performed in a three-electrode configuration at a scan rate of 50 mV s^{-1}. (b) Schematic of the assembled structure of an ASC based on MnO_2 as cathode and P-GA as anode. (c) CV and (d) GCD curves of an optimized MnO_2//P-GA ASC measured at different voltage windows in a two-electrode configuration.

An ASC device was then assembled using P-GA (negative electrode) and MnO_2 (positive electrode) as illustrated in Figure 4b (assigned as MnO_2//P-GA). Figure 4c exhibits CV curves of an optimized MnO_2//P-GA ASC at various potential windows in 0.1 M Na_2SO_4 aqueous solution at scan rate of 100 mV s^{-1}. The assembled ASC shows quasi-rectangular shape even at the voltage window up to 1.6 V, indicating the feasibility of employing P-GA and MnO_2 as negative and positive electrodes respectively and good capacitive behavior of the assembled ASC device. In addition, GCD measurements were also performed to investigate the feasibility of as-assembled MnO_2//P-GA ASC. Figure 4e shows the GCD curves at various potential windows ranging from 0.8 V to 1.6 V at a current density of 4 A g^{-1}. The GCD curves exhibit stable triangular shape up to 1.6V which further supports the stable electrochemical voltage of the MnO_2//P-GA ASC device.

Figure 5a shows the CV curves of MnO_2//P-GA ASC measured at various scan rates of 5, 20, 50, 100, 200, and 500 mV s^{-1} with a voltage window of 1.6 V. No significant redox peaks are observed indicates ideal capacitive behavior. Moreover, CV profiles remain a relatively rectangular shape without apparent distortion as the scan rate increases from 5 to 500 mV s^{-1}, manifesting the favorable fast charge and discharge characteristic for power devices. The maximum specific capacitance for MnO_2//P-GA ASC reaches 108.9 F g^{-1} at a scan rate of 5 mV s^{-1}. Additionally, the specific capacitance still remains at 37.8 F g^{-1} (34.7% retention) even when the scan rate is increased by 100 times to 500 mV s^{-1}. GCD curves of MnO_2//P-GA ASC at various current densities are shown in Figure 5b. The good symmetry of the GCD curves validates its efficient capacitive behavior. The electrochemical impedance spectroscope (EIS) is performed to further examine the electrochemical performance of MnO_2//P-GA ASC with different frequency (10 mHz to 100 kHz). The Nyquist plots (Figure 5c) presents a nearly vertical line, indicating an ideal capacitive nature of MnO_2//P-GA ASC. In addition, the resistance of MnO_2//P-GA ASC is relatively near the intercept of the Nyquist curve on the real axis as shown in the inset of Figure 5c, demonstrating the great conductivity of the electrolyte and small internal resistivity of the electrode. Figure 5d exhibits the Bode plots of the MnO_2//P-

GA ASC. The nearly -90° phase angle with frequency up to 1 Hz of MnO_2//P-GA ASC implies an ideal capacitor is obtained. The relaxation time (233 ms) is measured based on the frequency (4.29 Hz) that has a phase angle of -45° at which point gives the equal resistive and capacitive impedances.[51] This exceptionally small time constant for the MnO_2//P-GA ASC is competitive compared with other reported values for SCs such as carbon aerogel (2000 ms) [52], activated carbon (700 ms) [53], MnO_2/carbon composite (500 ms) [54], AuPd-MnO_2 core-shell (59 ms) [55], etc.

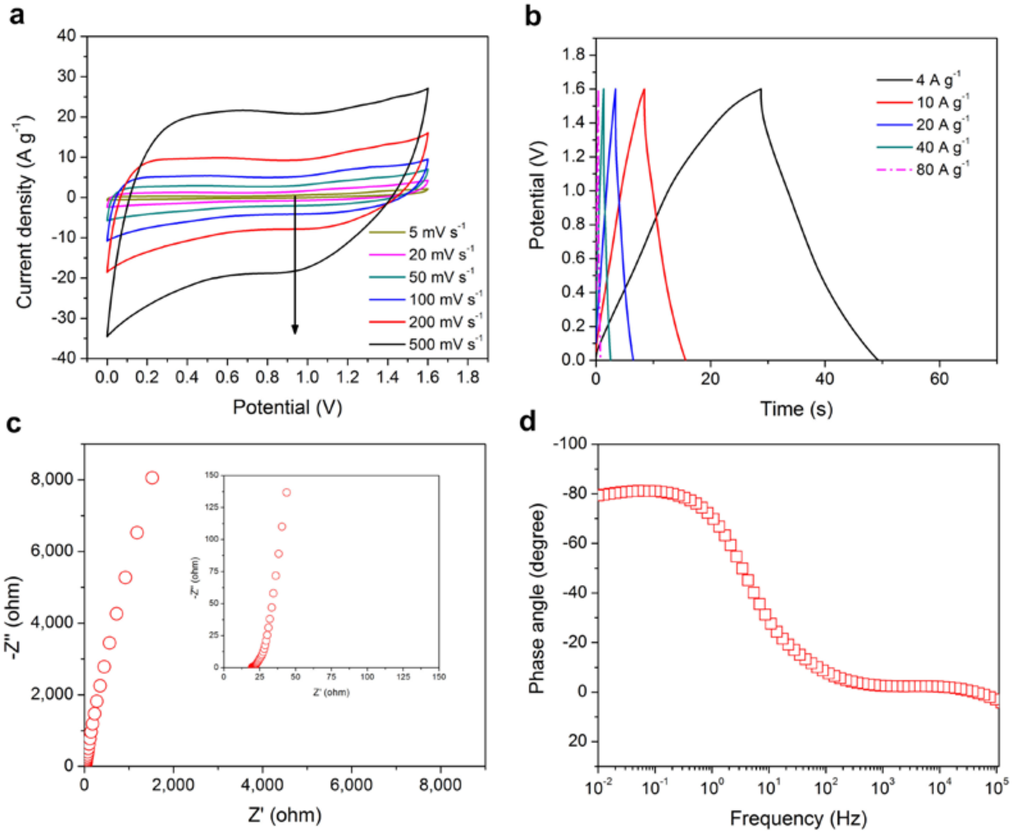

Figure 6.5 (a) CV curves of MnO_2//P-GA ASC at different scan rates (5 – 500 mV s^{-1}). (b) CV curves of MnO_2//P-GA ASC at different current densities (4 – 80 A g^{-1}). (c) Nyquist and (d) Bode plots for the MnO_2//P-GA ASC.

Cycling stablility is a vital characterictic for evaluating the performance of energy storage devices. Figure 6a displays the cyclic performance of MnO_2//P-GA ASC at a scan rate of 200 mV s^{-1}. The capacitance still remains at 89.6% of its initial value after 3,000 cycles, suggesting remarkable cycling stability. The two other important parameters, energy density and power densities, have also been widely used to evaluate the performance of energy storge devices. Figure 6b shows Ragone plots (energy density vesus power density) of MnO_2//P-GA ASC. The average energy density is 13.9 Wh kg^{-1} with a power density of 13.3 kW kg^{-1}. These results are higher or comparable to other recently reported values of ASCs, such as MnO_2 nanowire-graphene//graphene (MnO_2 NW-Graphene//Graphene, 7.2 Wh kg^{-1} and 5.0 kW kg^{-1}) [56], nickel hydroxide-graphite//activated graphene oxide ($Ni(OH)_2$-graphite//AGO, 6.9 Wh kg^{-1} and 44.0 kW kg^{-1}) [57], reduced graphene oxide-ruthenium oxide//reduced graphene oxide-polyaniline (RGO-RuO_2//RGO-PANI, 6.7 Wh kg^{-1} and 50.0 kW kg^{-1}) [58], graphene-MnO_2//activated carbon nanofiber (Graphene-MnO_2//ACN, 10 Wh kg^{-1} and 12.0 kW kg^{-1}) [23], and MnO_2//graphene hydrogel (MnO_2//GH, 14.9 Wh kg^{-1} and 10.0 kW kg^{-1}) [35], etc. To further demonstrate the feasibility of our MnO_2//P-GA ASC, two ASCs were assembled in series to light up a commercially available red light-emitting-diode (LED, 2V) as shown in the inset of Figure 6b. These promising results for P-GA may lead to other applications such as sensing or catalysis and our fabrication procedure should be generally applicable to other thermally processable precursors. Investigation into incorporating less expensive metals and other functionalities into our GA is in progress.

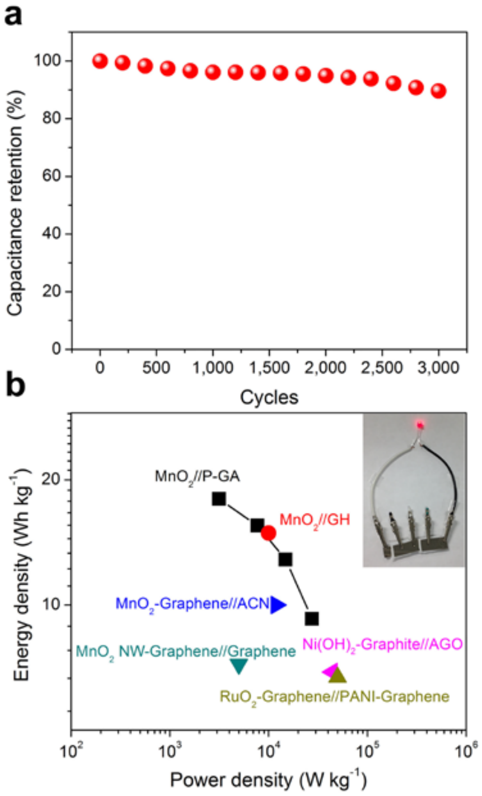

Figure 6.6 (a) Cycle performance of the device at a scan rate of 200 mv s^{-1}. (b) Ragone plots of MnO_2//P-GA ASC compared with other recently reported values of ASCs. The inset shows a LED lighting demonstration, with the diode driven by two devices in series.

6.7 Conclusion

We have developed a novel method to produce GA conformly loaded with Pd nanoparticles. This technique produces P-GA with a high surface area of 328 m^2 g^{-1} and a low electrical resistivity of 16 Ω cm, which is more than a 50 times lower than one without Pd. Electrodes fabricated using P-GA show highly improved electrochemical capacitive behavior than the GA one, which is attributed to the reduced resistivity. Significantly, we have successfully demonstrated a high performance ASC based on this P-GA anode and MnO_2 cathode. MnO_2//P-GA ASC shows an average energy and power densities of 13.9 Wh kg^{-1} and

13.3 kW kg^{-1}. These values are substantially enhanced compared to other recently published ASC devices. The employment of P-GA anode for ASCs broadens the pathway of chasing high energy and power densities energy storage devices.

6.8 References

1. P. Simon and Y. Gogotsi, *Nat. Mater.*, 2008, **7**, 845-854.
2. Z. Yu, B. Duong, D. Abbit and J. Thomas, *Adv. Mater.*, 2013, **25**, 3302-3306.
3. G. Wang, L. Zhang and J. Zhang, *Chem. Soc. Rev.*, 2012, **41**, 797-828.
4. L. L. Zhang and X. Zhao, *Chem. Soc. Rev.*, 2009, **38**, 2520-2531.
5. Z. Yu, C. Li, D. Abbitt and J. Thomas, *J. Mater. Chem. A*, 2014, **2**, 10923-10929.
6. J. R. Miller and P. Simon, *Science*, 2008, **321**, 651-652.
7. J. R. Miller and A. F. Burke, *Electrochem. Soc. Interface*, 2008, **17**, 53-57.
8. Y. Hou, Y. Cheng, T. Hobson and J. Liu, *Nano Lett.*, 2010, **10**, 2727-2733.
9. Z. Yang, J. Deng, X. Chen, J. Ren and H. Peng, *Angew. Chem. Int. Ed.*, 2013, **52**, 13453-13457.
10. M. D. Stoller and R. S. Ruoff, *Energy Environ. Sci.*, 2010, **3**, 1294-1301.
11. L. Demarconnay, E. Raymundo-Pinero and F. Beguin, *J. Power Sources*, 2011, **196**, 580-586.
12. A. Lewandowski, A. Olejniczak, M. Galinski and I. Stepniak, *J. Power Sources*, 2010, **195**, 5814-5819.
13. B. Duong, Z. Yu, P. Gangopadhyay, S. Seraphin, N. Peyghambarian and J. Thomas, *Adv. Mater. Interfaces*, 2014, **1**, 1300014.

14. Y. Wang and Y. Xia, *Electrochem. Commun.*, 2005, **7**, 1138-1142.

15. P.-C. Chen, G. Shen, Y. Shi, H. Chen and C. Zhou, *ACS Nano*, 2010, **4**, 4403-4411.

16. X. Xiao, T. Li, Z. Peng, H. Jin, Q. Zhong, Q. Hu, B. Yao, Q. Luo, C. Zhang and L. Gong, *Nano Energy*, 2014, **6**, 1-9.

17. P. Yang, Y. Ding, Z. Lin, Z. Chen, Y. Li, P. Qiang, M. Ebrahimi, W. Mai, C. P. Wong and Z. L. Wang, *Nano Lett.*, 2014, **14**, 731-736.

18. D.-W. Wang, F. Li and H.-M. Cheng, *J. Power Sources*, 2008, **185**, 1563-1568.

19. Y. Chen, Z. Yu, Y. Chen, L. Luo and X. Wang, Materials for Renewable Energy & Environment (ICMREE), 2011 International Conference on, Shanghai, 2011.

20. Z. Tang, C.-H. Tang and H. Gong, *Adv. Funct. Mater.*, 2012, **22**, 1272-1278.

21. J. Yan, Z. Fan, W. Sun, G. Ning, T. Wei, Q. Zhang, R. Zhang, L. Zhi and F. Wei, *Adv. Funct. Mater.*, 2012, **22**, 2632-2641.

22. C. Zhou, Y. Zhang, Y. Li and J. Liu, *Nano Lett.*, 2013, **13**, 2078-2085.

23. Z. Fan, J. Yan, T. Wei, L. Zhi, G. Ning, T. Li and F. Wei, *Adv. Funct. Mater.*, 2011, **21**, 2366-2375.

24. X. Wang, C. Yan, A. Sumboja and P. S. Lee, *Nano Energy*, 2014, **3**, 119-126.

25. L.-F. Chen, Z.-H. Huang, H.-W. Liang, Q.-F. Guan and S.-H. Yu, *Adv. Mater.*, 2013, **25**, 4746-4752.

26. H. Jiang, C. Li, T. Sun and J. Ma, *Nanoscale*, 2012, **4**, 807-812.

27. A. Sumboja, C. Y. Foo, X. Wang and P. S. Lee, *Adv. Mater.*, 2013, **25**, 2809-2815.

28. A. K. Geim and K. S. Novoselov, *Nat. Mater.*, 2007, **6**, 183-191.

29. Y. Zhu, S. Murali, W. Cai, X. Li, J. W. Suk, J. R. Potts and R. S. Ruoff, *Adv. Mater.*, 2010, **22**, 3906-3924.

30. J. J. Yoo, K. Balakrishnan, J. Huang, V. Meunier, B. G. Sumpter, A. Srivastava, M. Conway, A. L. Mohana Reddy, J. Yu and R. Vajtai, *Nano Lett.*, 2011, **11**, 1423-1427.

31. Y. Sun, Q. Wu and G. Shi, *Energy Environ. Sci.*, 2011, **4**, 1113-1132.

32. T. Chen, Y. Xue, A. K. Roy and L. Dai, *ACS Nano*, 2014, **8**, 1039-1046.

33. H.-J. Choi, S.-M. Jung, J.-M. Seo, D. W. Chang, L. Dai and J.-B. Baek, *Nano Energy*, 2012, **1**, 534-551.

34. P. Chen, J.-J. Yang, S.-S. Li, Z. Wang, T.-Y. Xiao, Y.-H. Qian and S.-H. Yu, *Nano Energy*, 2013, **2**, 249-256.

35. H. Gao, F. Xiao, C. B. Ching and H. Duan, *Acs Appl. Mater. Interfaces*, 2012, **4**, 2801-2810.

36. Y. Gong, S. Yang, L. Zhan, L. Ma, R. Vajtai and P. M. Ajayan, *Adv. Funct. Mater.*, 2014, **24**, 125-130.

37. X. Cao, Z. Yin and H. Zhang, *Energy Environ. Sci.*, 2014, **7**, 1850-1865.

38. P. Yang, X. Xiao, Y. Li, Y. Ding, P. Qiang, X. Tan, W. Mai, Z. Lin, W. Wu, T. Li, H. Jin, P. Liu, J. Zhou, C. P. Wong and Z. L. Wang, *ACS Nano*, 2013, **7**, 2617-2626.

39. Z. S. Wu, A. Winter, L. Chen, Y. Sun, A. Turchanin, X. Feng and K. Müllen, *Adv. Mater.*, 2012, **24**, 5130-5135.

40. H.-P. Cong, X.-C. Ren, P. Wang and S.-H. Yu, *ACS Nano*, 2012, **6**, 2693-2703.

41. S. Yun, S.-O. Kang, S. Park and H. S. Park, *Nanoscale*, 2014, **6**, 5296-5302.

42. Y. Wang, Z. Shi, Y. Huang, Y. Ma, C. Wang, M. Chen and Y. Chen, *J. Phys. Chem. C*, 2009, **113**, 13103-13107.

43. Y. Okamoto, *Chem. Phys. Lett.*, 2006, **420**, 382-386.

44. R. Kumar, D. Varandani, B. Mehta, V. Singh, Z. Wen, X. Feng and K. Müllen, *Nanotechnology*, 2011, **22**, 275719.

45. W. S. Hummers Jr and R. E. Offeman, *J. Am. Chem. Soc.*, 1958, **80**, 1339-1339.

46. F. Liu, S. Song, D. Xue and H. Zhang, *Adv. Mater.*, 2012, **24**, 1089-1094.

47. M. O. Nutt, K. N. Heck, P. Alvarez and M. S. Wong, *Appl. Catal. B: Environ.*, 2006, **69**, 115-125.

48. H. Qian, A. R. Kucernak, E. S. Greenhalgh, A. Bismarck and M. S. Shaffer, *ACS Appl. Mater. Interfaces*, 2013, **5**, 6113-6122.

49. X. Zhang, Z. Sui, B. Xu, S. Yue, Y. Luo, W. Zhan and B. Liu, *J. Mater. Chem.*, 2011, **21**, 6494-6497.

50. K. Gao, Z. Shao, X. Wang, Y. Zhang, W. Wang and F. Wang, *RSC Advances*, 2013, **3**, 15058-15064.

51. P. Taberna, P. Simon and J.-F. Fauvarque, *J. Electrochem. Soc.*, 2003, **150**, A292-A300.

52. G. Rasines, P. Lavela, C. Macías, M. Haro, C. Ania and J. Tirado, *J. Electroanal. Chem.*, 2012, **671**, 92-98.

53. D. Pech, M. Brunet, H. Durou, P. Huang, V. Mochalin, Y. Gogotsi, P.-L. Taberna and P. Simon, *Nat. Nanotechnol.*, 2010, **5**, 651-654.

54. L. Yuan, X. H. Lu, X. Xiao, T. Zhai, J. Dai, F. Zhang, B. Hu, X. Wang, L. Gong and J. Chen, *ACS Nano*, 2012, **6**, 656-661.

55. Z. Yu and J. Thomas, *Adv. Mater.*, 2014, **26**, 4279-4285.

56. Z.-S. Wu, W. Ren, D.-W. Wang, F. Li, B. Liu and H.-M. Cheng, *ACS Nano*, 2010, **4**, 5835-5842.

57. J. Ji, L. L. Zhang, H. Ji, Y. Li, X. Zhao, X. Bai, X. Fan, F. Zhang and R. S. Ruoff, *ACS Nano*, 2013, **7**, 6237-6243.

58. J. Zhang, J. Jiang, H. Li and X. S. Zhao, *Energy Environ. Sci.*, 2011, **4**, 4009-4015.

7 FABRICATION OF ASYMMETRIC SUPERCAPACITORS WITH Fe_2O_3 NANORODS AND MnO_2 NANOWHISKERS*

7.1 Introduction

The ever growing utilization of renewable energy sources, such as solar or wind, requires efficient energy storage systems. Among different energy storage devices, supercapacitors (SCs) have been extensively investigated due to their fast charge-discharge rate, high power density, and superior cycle stability.[1-3] Recently, cable-shaped SCs have emerged as a novel device configuration because of their remarkable advantages over conventional sandwich-like SCs, such as smaller size, lighter weight, easier to bend, better portability *etc*.[4-6] To date, while several studies based on cable-shaped SCs have been performed,[7-14] most devices were assembled as symmetric SCs. On the other hand, asymmetric supercapacitors (ASCs) possess much wider cell potentials compared to symmetric SCs,[15-18] resulting in substantially higher energy densities based on the equation $E = \frac{1}{2}CV^2$, where E is the energy density, C is the cell capacitance, and V is the cell potential. In addition, we have recently developed a dual-function energy storing electrical cable that can transmit and store electricity independently.[19] However, the energy storage component in this integrated device is still a symmetric SC which limits its energy density. Therefore, it is important to incorporate ASCs in these cable-like device configurations.

Here, we developed a coil-type asymmetric supercapacitor electrical cable (CASEC) which not only serves as a cable-shaped ASC but also as a dual-function energy-storing electrical-cable with a coil-type design for better mechanical stability. As shown in Figure 7.1a, a

---

[*] The work presented in this chapter has been published in Z. Yu, J. Moore, J. Calderon, L. Zhai, and J. Thomas, Submitted.

strand of carbon fibers is extracted from a commercial available carbon fabric and placed inside a Teflon-lined stainless-steel autoclave to undergo a hydrothermal reaction yielding FeOOH nanorods (NRs). The carbon fibers were then rinsed with deionized water to remove any excess reaction solution and annealednitrogen gas. This process results in the finalized anode: a strand of carbon fibers uniformly coated with Fe_2O_3 NRs. The intention behind the usage of carbon fibers as a backbone to grow Fe_2O_3 NRs is that carbon materials are lightweight and stable. Moreover, as suggested by *Gogotsi*,[20] carbon outer electrodes (*e.g.* carbon fibers) could potentially be wrapped around the inner electrode, which might be knitted or embedded into textiles, depending on the size of the inner electrode. Fabrication of the cathode begins with heat treating ordinary copper wire (Figure 7.1b). This process grows CuO nanowhiskers (NWs) uniformly around the core of the wire which remains as copper. In addition to the CuO NWs, a cupric oxide layer was formed upon heating, which serves as an insulator layer and prevents current leakage from the inner copper core.[19] A current collector material, in this case AuPd alloy, is then coated onto the CuO NW structure via plasma sputter deposition. Electrodeposition of MnO_2 completes the core-shell structure of the cathode. To create the CASEC, both electrodes are wet with LiCl/PVA gel electrolyte and set to dry. Once both electrodes are dry, an ion porous separator is placed around the cathode and the anode is wound tightly around thus completing the fabrication process. Figure 7.1c shows a schematic of the resulting device.

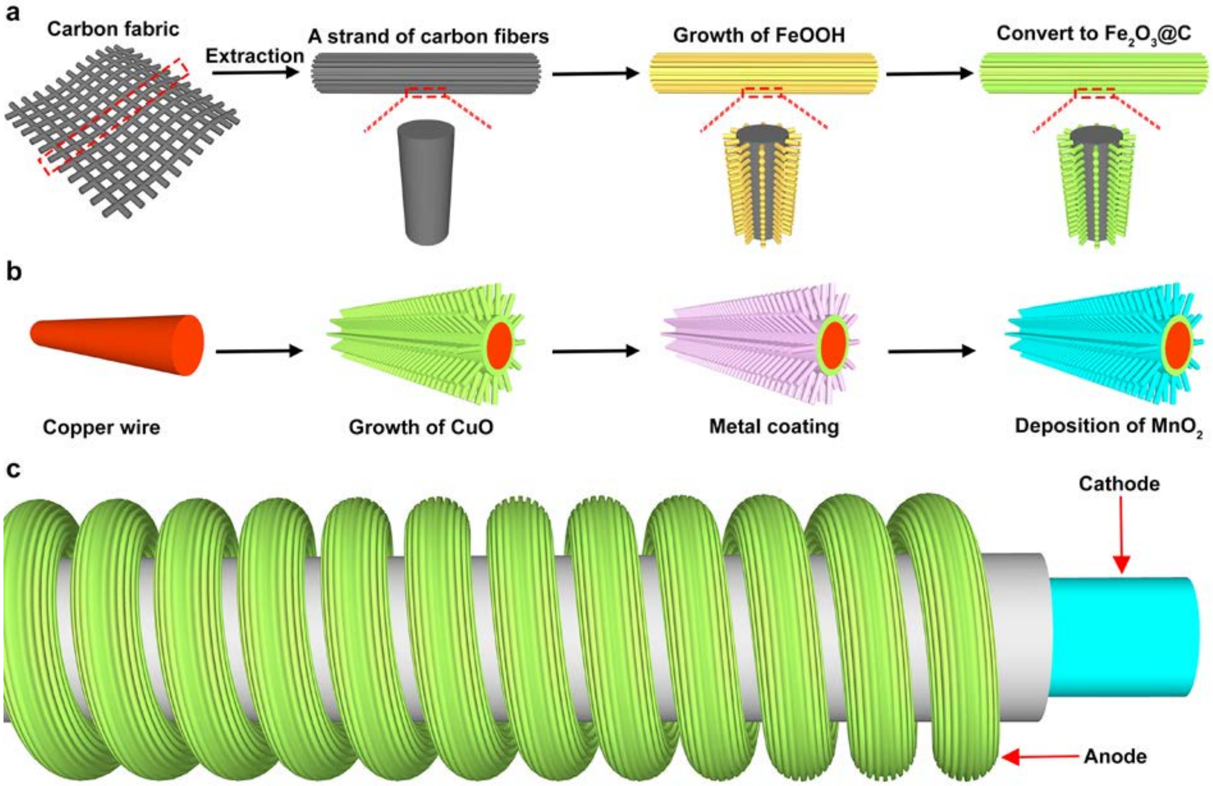

Figure 7.1 Schematics illustration showing the fabrication process of (a) an anode and (b) a cathode, respectively. (c) Illustration of a CASEC.

7.2 Preparation of Anodes

A strand of carbon fibers was first extracted from a commercial carbon fabric. Fe_2O_3 nanorods (NRs) were grown on the carbon fibers by modifying a previously reported method.[21] Briefly, 20 mL aqueous solution containing 0.15 M ferric chloride ($FeCl_3·6H_2O$) and 1 M sodium nitrate ($NaNO_3$) was prepared and filled into a Teflon-lined stainless-steel autoclave with 50 mL capacity. A strand of carbon fibers was immersed into the precursor solution. One terminal of the strand of carbon fibers was sealded using a Teflon tape to avoid any hydrothermally growth, which can later serve as a connection point to contect with outside electric circuit upon peeling off the tape. The autoclave was heated to 95 °C for 6h, followed by cooling to room temperature. FeOOH NRs were uniformly grown onto these carbon fibers. In order to obtain a thin carbon shell coating, an additional hydrothermal treament was carried out at 180 °C for 4h in a water based solution containing 0.1M glucose. The samples were further heated in N_2 at 400 °C for 1h to obtain Fe_2O_3@C core-shell structured NRs. Scanning electron microscope (SEM) image shows that the Fe_2O_3 NRs were uniformly grown on each carbon fiber (Figure 7.2a). The Fe_2O_3 NRs have diameters ~ 100 to 200 nm and lengths ~ 300 to 600 nm (Figure 7.2b). Figure 7.2c exhibits transmission electron microscopy (TEM) image with low magnification of a Fe_2O_3 NR, which agrees with the SEM results. A high resolution transmission electron microscopy (HRTEM) is presented in Figure 7.2d. A fringe spacing of 0.27 nm which assigned to the (104) planes (Joint Committee on Powder Diffraction Standards (JCPDS) #33-0664) confirms the hematite structure.

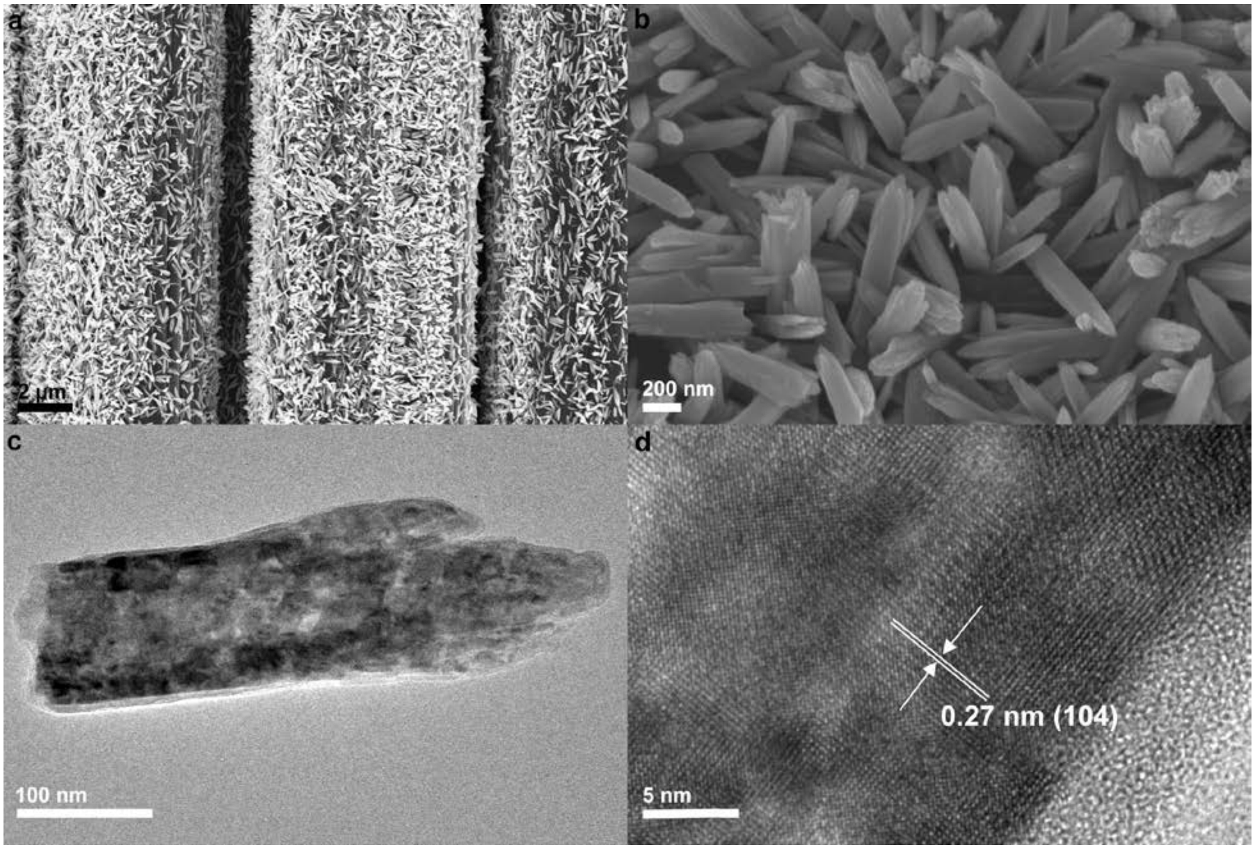

Figure 7.2 (a) SEM image shows carbon fibers that were uniformly grown with Fe2O3@C nanorods. (b) Close-up view of SEM image shows Fe2O3@C nanorods grown upward. (c) TEM and (d) HRTEM images of a Fe2O3@C nanorod.

7.3 Preparation of Cathodes

CuO nanowhiskers (NWs) were first grown on a copper wire via a facile heat treatment reported elsewhere.[22] A thin layer of metal coating (AuPd alloy) was carried out using a sputter coater at a current of 40.0 mA for 20 min. Afterwards, MnO_2 was deposited onto the nanostructures via an anodic electrodeposition at a current density of 0.5 mA cm^{-2}. The electrolyte used for electrodeposition was prepared by dissolving 0.02 M ammonium acetate and 0.01 M manganese acetate into a solvent containing 10 v/v% of dimethyl sulfoxide and 90 v/v% of de-ionized (DI) water. Figure 7.3a shows a copper wire after heat treatment, indicating the

CuO NWs were uniformly surrounded on the copper wire surface. A cross-section SEM image (Figure 7.3b) confirms the vertically grown CuO NWs with a length of ~ 10 – 15 μm. MnO_2 was then conformally deposited onto each CuO NW (pre-coated with metal alloy) as shown in Figure 7.3c. Figure 7.3d is the TEM image of the resulting NWs, revealing the CuO core and MnO_2 shell.

7.4 Fabrication of Solid-State Devices

A CASEC was obtained by tightly coiling an anode onto a cathode with an ionic conductive and electronic insulated separator (Celgard 3501) in between. Before the coiling process, both the anode and cathode were immersed into a gel electrolyte and allowed to dry. The gel electrolyte was made by dissolving 8.48 g lithium chloride (LiCl) and 4 g polyvinyl alcohol (PVA) in 40 mL DI water and heated at 90 °C under constant stirring until the solution turned to clear. After coiling process, appropriate gel electrolyte was again applied across the whole device and was left to solidify at 25 °C for several hours in order to obtain a solid-state CASEC.

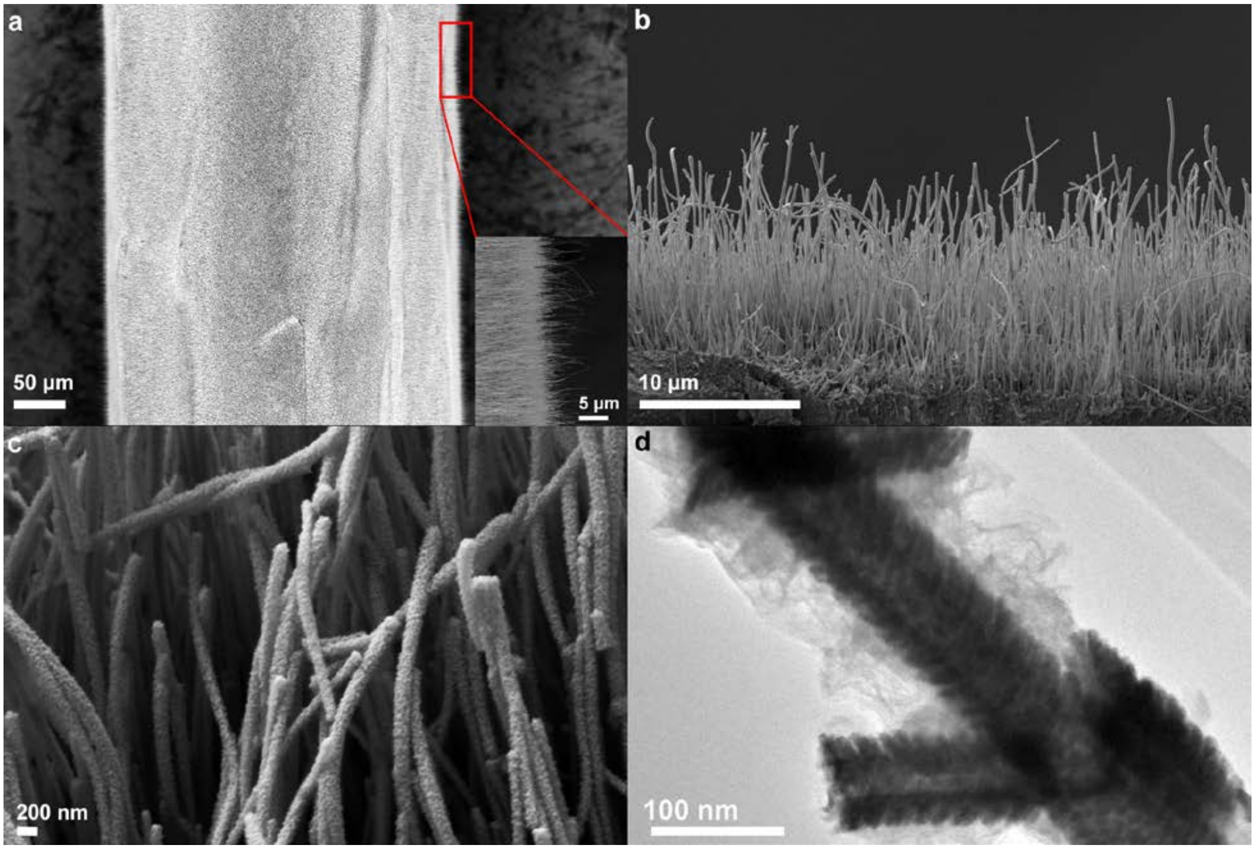

Figure 7.3 (a) SEM shows a copper wire grown with CuO NWs. The inset shows the surface of copper wire is fully covered by the CuO NWs. (b) Cross-section SEM image shows vertically grown CuO NWs with lengths more than 10 μm. (c) SEM and (d) images show CuO NWs that were conformally coated with MnO2.

7.5 Materials Characterization and Electrochemical Measurements

Surface morphologies were examined both by scanning electron microscopy (SEM) and transmission electron microscopy (TEM). X-ray photoelectron spectroscopy (XPS) was conducted to evaluate the chemical compositions. In order to compare the performance of anodes and cathodes, a three-electrode system which includes a working electrode (based on the as-synthesized materials), a platinum plate as counter electrode, and a saturated calomel electrode (SCE) as reference electrode was used. Cyclic voltammetry (CV) and galvanostatic charge-discharge (GCD) were carried out via this three-electrode system in 5M LiCl solution using an electrochemical workstation (Bio-Logic, SP-150). The characterization experiments of the CASECs using gel electrolyte were performed by a two-electrode system at various voltage window ranging from 0.8 to 1.6 V.

7.6 Performance Evaluation of Electrodes/Devices

CV was conducted to investigate the electrochemical properties of anode and cathode. Figure 7.4a and b show the CV curves of anode and cathode at scan rates ranging from 5 to 500 mV/s. The CV curves of anode, which display ideal rectangular shapes, attribute to the pseudocapacitive nature of Fe_2O_3,[23, 24] in which a reversible Fe^{3+}/Fe^{2+} couple occurs during the redox reaction. All the CV curves of cathode manifest nearly rectangular shape, indicating excellent reversibility and electrochemical behavior. This is likely due to the nanostructured current collector design, which substantially improves the electronic conductivity.[3] Figure 7.4c shows the specific capacitance of both anode and cathode with respect to scan rate. The specific capacitance of anode is 90.8 F g^{-1} at 20 mV s^{-1}, which is substantially higher than other Fe_2O_3 based electrodes, such as Fe_2O_3 nanoflowers (73 F g^{-1}, ~20 mV s^{-1}),[25] Fe_2O_3 nanotubes (~ 26 F g^{-1}, 10 mV s^{-1}),[26] and Fe_2O_3 nanoforests (64.5 F g^{-1}, 10 mV s^{-1}).[27] For the cathode, a specific capacitance of 508.1 F g^{-1} is achieved at a scan rate of 20 mV s^{-1}, which is also higher than other recently reported MnO_2 based electrodes, such as MnO_2 nanopillars (484.2 F g^{-1}, 20 mV s^{-1}),[28] MnO_2 NRs (302 F g^{-1}, 5 mV s^{-1}),[29] MnO_2 thin films (410 F g^{-1}, 20 mV s^{-1}),[30] and MnO_2 nanosheets (~400 F g^{-1}, ~10 mV s^{-1}).[31] . Additionally, the different CV areas of anode and cathode would lead to a mismatch of charges stored. As a result, the mass loading from anode and cathode should be controlled at a constant ratio of ~ 0.133 in order to keep the charge balance (q+=q-).

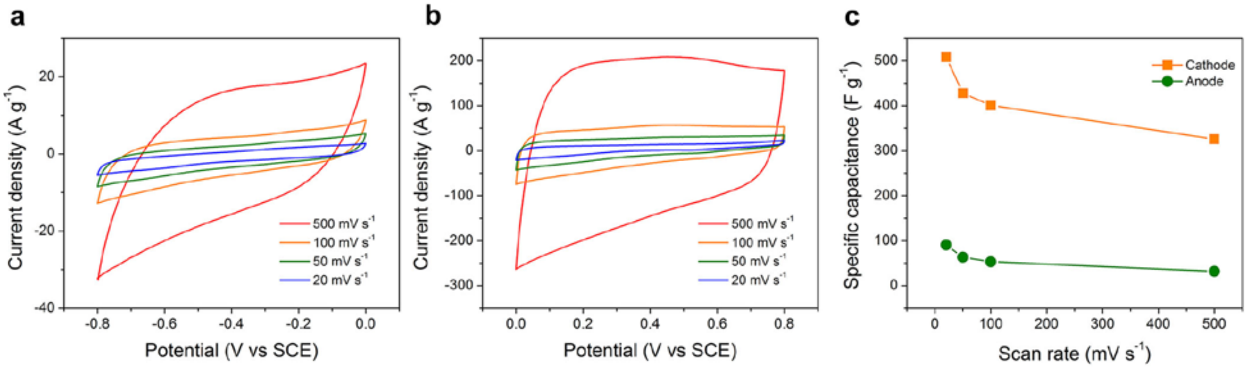

Figure 7.4 CV curves of (a) anode and (b) cathode at different scan rates (20 – 500 mV s^{-1}). (c) Specific capacitance of anode and cathode as a function of scan rate, respectively.

As mentioned earlier, a CASEC is prepared by simply coiling the anode onto the cathode with a separator in between. In addition, LiCl/PVA gel electrolyte is applied to both anode and cathode before the coiling. As an energy storage device, a two-electrode system was carried out to test the supercapacitive performance. Figure 7.5a reveals the excellent performance of our device in the enhanced voltage window of 1.6V at various scan rates. All the CV curves exhibit nearly rectangular shape, manifesting good electrochemical behavior of the device. GCD measurements of CASEC were carried out at different current densities (Figure 7.5b). The charge-discharge profiles exhibit quasi-triangle characteristic, indicating good reversibility and fast charge-discharge nature. The highest volumetric specific capacitance for CASEC is 1.6 F cm^{-3} at 0.13 A cm^{-3}, which is significantly greater than other recently reported values for solid-state ASCs.[27, 32, 33] Moreover, excellent rate capability (95.4%) is achieved with increased current density up to 1.32 A cm^{-3}. Cycle stability is one of the critical characteristics for developing practical energy storage devices. Figure 7.5c presents the long-term cycle stability of the CASEC at a scan rate of 200 mV s^{-1}. The capacitance maintains a promising 97.1% of its initial value after 4000 charge-discharge cycles, revealing the design's superior cycle stability. A Ragone plot exhibits the energy density vs power density of a CASEC compared to other recently reported values (Figure 7.5d). The highest energy density of the CASEC is 0.53 mWh cm^{-3}, which is significantly higher than other solid-state SCs, such as ZnO@MnO$_2$-SCs (0.018 mWh cm^{-3}),[34] carbon nanotube SCs (CNT-SCs, 0.02 mWh cm^{-3}),[35] Graphene-SCs (0.06 mWh cm^{-3}),[36] TiO$_2$@MnO$_2$ and TiO$_2$@C asymmetric SCs (TiO$_2$@MnO$_2$//TiO$_2$@C-SCs, 0.15 mWh cm^{-3}),[32] CuO@AuPd@MnO$_2$-SCs (0.21 mWh cm^{-3}),[19] and Co$_9$S$_8$//Co3O4@RuO$_2$-SCs (0.22 mWh cm^{-3}).[37]

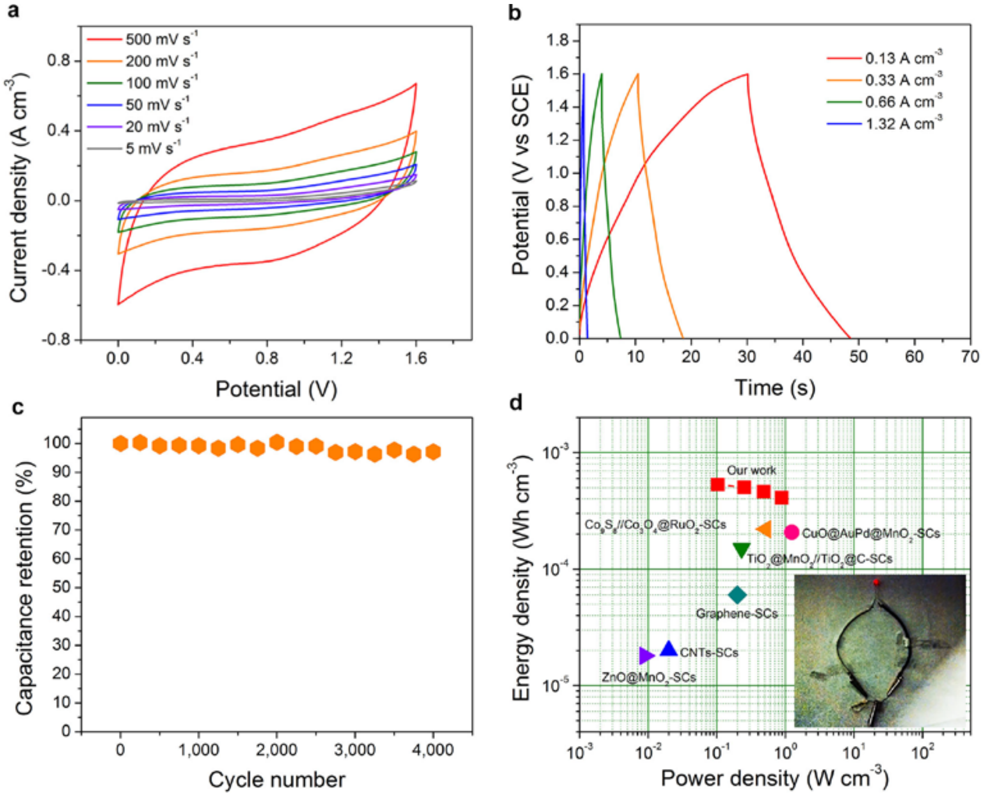

Figure 7.5 (a) CV and (b) GCD curves of CASECs. (c) Cycle performance of the device at a scan rate of 200 mV s^{-1}. (d) Ragone Plots of the device compared with other recently reported values of ASCs. The inset shows a LED powered by the tandem devices.

We designed experiments to verify the dual functionality of CASEC (Figure 7.6a). We first measured the output voltage of the pre-charged CASEC before connecting the electrical circuit (LED not working). The voltage of the CASEC showed 1.575 V (Figure 7.6b), which suggests charge maintaining state of the CASEC. After we connected the electrical circuit (LED working), the voltage still stayed at 1.575 V (Figure 7.6c), suggesting that the electrical conduction function does not interfere with the energy storage function of CASEC.

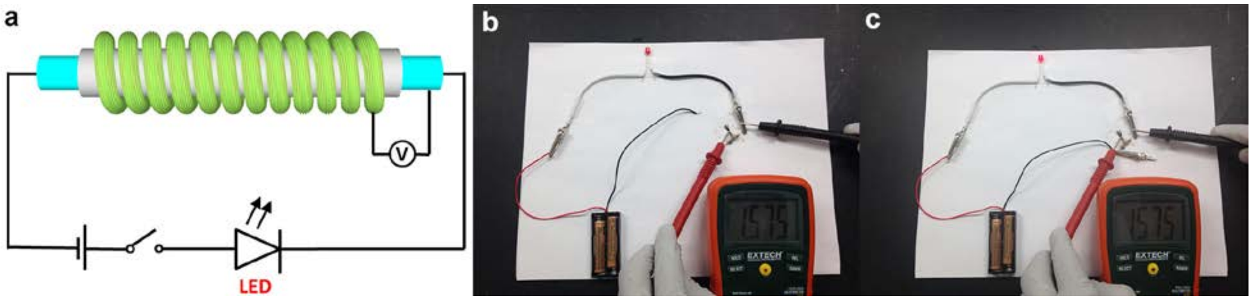

Figure 7.6 (a) Schematic of the configuration to measure dual functionality of CSC. (b) Before the power was turned on (open circuit), the voltage of a pre-charged CASEC showed 1.575 V. (c) After the power was turned on (LED on), the voltage of the pre-charged CASEC still showed 1.575 V.

7.7 Conclusion

We have successfully developed a novel CASEC that combines a cable-shaped ASC with an electrical cable. With a coiled design using a strand of carbon fibers, not only the mechanical stability is improved, but also makes it feasible to be used in knitted textiles or embedded into textiles. As an energy storage device alone, CASECs show excellent electrochemical properties including symmetrical CV and GCD curves, extraordinary rate capability (95.4%), high energy density (0.53 mWh cm^{-3}), and superior cycle stability (97.1% after 4000 cycles). Additionally, the dual-function experiment further testifies the feasibility of both transmitting and storing electricity. All these results demonstrate that CASECs have a promising future for applications like high-performance and multi-function electronics.

7.8 References

1. P. Simon and Y. Gogotsi, *Nat. Mater.*, 2008, **7**, 845-854.

2. P. Simon, Y. Gogotsi and B. Dunn, *Science*, 2014, **343**, 1210-1211.

3. Z. Yu, L. Tetard, L. Zhai and J. Thomas, *Energy Environ. Sci.*, 2015, DOI: 10.1039/C4EE03229B, DOI: 10.1039/C1034EE03229B.

4. X. Wang, X. Lu, B. Liu, D. Chen, Y. Tong and G. Shen, *Adv. Mater.*, 2014, **26**, 4763-4782.

5. S.-Y. Lee, K.-H. Choi, W.-S. Choi, Y. H. Kwon, H.-R. Jung, H.-C. Shin and J. Y. Kim, *Energy Environ. Sci.*, 2013, **6**, 2414-2423.

6. D. Yu, Q. Qian, L. Wei, W. Jiang, K. Goh, J. Wei, J. Zhang and Y. Chen, *Chem. Soc. Rev.*, 2015, DOI: 10.1039/C1034CS00286E.

7. Y. Fu, X. Cai, H. Wu, Z. Lv, S. Hou, M. Peng, X. Yu and D. Zou, *Adv. Mater.*, 2012, **24**, 5713-5718.

8. J. A. Lee, M. K. Shin, S. H. Kim, H. U. Cho, G. M. Spinks, G. G. Wallace, M. D. Lima, X. Lepró, M. E. Kozlov and R. H. Baughman, *Nat. Commun.*, 2013, **4**, 1970.

9. J. Bae, M. K. Song, Y. J. Park, J. M. Kim, M. Liu and Z. L. Wang, *Angew. Chem. Int. Ed.*, 2011, **50**, 1683-1687.

10. X. Wang, B. Liu, R. Liu, Q. Wang, X. Hou, D. Chen, R. Wang and G. Shen, *Angew. Chem. Int. Ed.*, 2014, **53**, 1849-1853.

11. T. Chen, R. Hao, H. Peng and L. Dai, *Angew. Chem. Int. Ed.*, 2015, **54**, 618-622.

12. X. Chen, H. Lin, J. Deng, Y. Zhang, X. Sun, P. Chen, X. Fang, Z. Zhang, G. Guan and H. Peng, *Adv. Mater.*, 2014, **26**, 8126-8132.

13. H. Xu, X. Hu, Y. Sun, H. Yang, X. Liu and Y. Huang, *Nano Res.*, 2014, DOI: 10.1007/s12274-014-0595-8.

14. X. Xiao, T. Li, P. Yang, Y. Gao, H. Jin, W. Ni, W. Zhan, X. Zhang, Y. Cao and J. Zhong, *Acs Nano*, 2012, **6**, 9200-9206.

15. Z. Fan, J. Yan, T. Wei, L. Zhi, G. Ning, T. Li and F. Wei, *Adv. Funct. Mater.*, 2011, **21**, 2366-2375.

16. Z. Yu, M. McInnis, J. Calderon, S. Seal, L. Zhai and J. Thomas, *Nano Energy*, 2015, **11**, 611-620.

17. J. Zhang, J. Jiang, H. Li and X. S. Zhao, *Energy Environ. Sci.*, 2011, **4**, 4009-4015.

18. Z.-S. Wu, W. Ren, D.-W. Wang, F. Li, B. Liu and H.-M. Cheng, *ACS Nano*, 2010, **4**, 5835-5842.

19. Z. Yu and J. Thomas, *Adv. Mater.*, 2014, **26**, 4279-4285.

20. Y. Gogotsi, *Nature*, 2014, **509**, 568-570.

21. Y. Ling, G. Wang, J. Reddy, C. Wang, J. Z. Zhang and Y. Li, *Angew. Chem. Int. Ed.*, 2012, **51**, 4074-4079.

22. X. Jiang, T. Herricks and Y. Xia, *Nano Lett.*, 2002, **2**, 1333-1338.

23. M. B. Sassin, A. N. Mansour, K. A. Pettigrew, D. R. Rolison and J. W. Long, *ACS nano*, 2010, **4**, 4505-4514.

24. P. Yang, Y. Ding, Z. Lin, Z. Chen, Y. Li, P. Qiang, M. Ebrahimi, W. Mai, C. P. Wong and Z. L. Wang, *Nano Lett.*, 2014, **14**, 731-736.

25. S. Shivakumara, T. R. Penki and N. Munichandraiah, *ECS Electrochemistry Letters*, 2013, **2**, A60-A62.

26. K. Lee, S. Deng, H. M. Fan, S. Mhaisalkar, H. Tan, E. S. Tok, K. Loh, W. Chin and C. H. Sow, *Nanoscale*, 2012, **4**, 2958-2961.

27. X. Lu, Y. Zeng, M. Yu, T. Zhai, C. Liang, S. Xie, M. S. Balogun and Y. Tong, *Adv. Mater.*, 2014, **26**, 3148-3155.

28. Z. Yu, B. Duong, D. Abbitt and J. Thomas, *Adv. Mater.*, 2013, **25**, 3302-3306.

29. L. Yuan, X.-H. Lu, X. Xiao, T. Zhai, J. Dai, F. Zhang, B. Hu, X. Wang, L. Gong, J. Chen, C. Hu, Y. Tong, J. Zhou and Z. L. Wang, *Acs Nano*, 2011, **6**, 656-661.

30. Z. Yu, C. Li, D. Abbitt and J. Thomas, *J. Mater. Chem. A*, 2014, **2**, 10923-10929.

31. J. Liu, J. Jiang, C. Cheng, H. Li, J. Zhang, H. Gong and H. J. Fan, *Adv. Mater.*, 2011, **23**, 2076-2081.

32. X. Lu, M. Yu, G. Wang, T. Zhai, S. Xie, Y. Ling, Y. Tong and Y. Li, *Adv. Mater.*, 2013, **25**, 267-272.

33. W. Zilong, Z. Zhu, J. Qiu and S. Yang, *J. Mater. Chem. C*, 2014, **2**, 1331-1336.

34. P. Yang, X. Xiao, Y. Li, Y. Ding, P. Qiang, X. Tan, W. Mai, Z. Lin, W. Wu, T. Li, H. Jin, P. Liu, J. Zhou, C. P. Wong and Z. L. Wang, *ACS Nano*, 2013, **7**, 2617-2626.

35. M. Kaempgen, C. K. Chan, J. Ma, Y. Cui and G. Gruner, *Nano Lett.*, 2009, **9**, 1872-1876.

36. M. F. El-Kady, V. Strong, S. Dubin and R. B. Kaner, *Science*, 2012, **335**, 1326-1330.

37. J. Xu, Q. Wang, X. Wang, Q. Xiang, B. Liang, D. Chen and G. Shen, *ACS nano*, 2013, **7**, 5453-5462.

8 CONCLUSION

8.1 Summary

In this dissertation, different approaches to fabricate nanostructured electrodes and their electrochemical performance are discussed. Chapter 1 and 2 provided an overview of the basic concepts of supercapacitors and the benefits of nanostructuring. Chapter 3 to 7 experimental described different nanoarchitectured supercapacitor electrodes/devices.

In Chapter 3, I demonstrated an efficient method, called spin-on nanoprint (SNAP), to produce well-ordered nanopillars with reusable template. The as-prepared polymer based nanostructure was employed as backbones to coat active materials. Supercapacitor electrodes based on these printed nanostructures showed considerable capacitance enhancement (~ 4 times) compared to those prepared based on non-nanostructures.

In Chapter 4, I further presented the SNAP method to fabricate nanostructured carbon electrodes. Supercapacitor devices assembled based on these carbon electrodes manifested 10 times enhancement in energy and power densities compared to those based on non-nanostructured carbon electrodes.

In Chapter 5, a template-free method was presented to fabricate high aspect ratio nanowhisker structures. Active materials were subsequently deposited on these nanostructures in order to prepare supercapacitor electrodes. This nanostructured design enabled a superb specific capacitance (1376 F g^{-1}) and extraordinary reversibility. The symmetric supercapacitors showed remarkable flexibility, excellent cycle stability, and high energy and power densities.

In Chapter 6, I presented a facile method to decorate palladium nanoparticles on graphene aerogel (GA) as asymmetric supercapacitor (ASC) anode materials. The resulting functionalized GA showed high surface area (328 $m^2\ g^{-1}$), specific capacitance (175.8 $F\ g^{-1}$ at 5 $mV\ s^{-1}$), great rate capability, and remarkable reversibility. ASCs fabricated from MnO_2 and functionalized GA showed improved voltage window, (175.8 $F\ g^{-1}$ at 5 $mV\ s^{-1}$), exceptional cycle stability, and excellent energy and power densities (13.9 $W\ h\ kg^{-1}$ and 13.3 $kW\ kg^{-1}$).

In Chapter 7, a coil-type asymmetric supercapacitor electrical cable (CASEC) is developed, which allows transmitting electricity and storing energy simultaneously and independently. The CASECs showed remarkable rate capability (95.4%), great energy and power densities, and superior cycle stability. Moreover, integrating electrical conduction and storage opened up many new opportunities for further developing lightweight and space-saving electronic gadgets.

8.2 Future Directions

Nanoarchitecturing electrode materials are very promising and feasible for the next generation energy storage devices. However, rational nanoarchitectured design is essential in order to realize high electrochemical performance including reversibility, rate capability, cycle stability, specific capacitance, and so on.

3D nanostructured current collector is very attractive if used in energy storage devices because they can provide highly efficient electronic transport. A feasible approach is to create conductive nanostructures on Ni foam. With conformal coating of active materials on the 3D nanostructured Ni foam, desired reversibility, rate capability, and specific capacitance can be easily achieved not only because of the excellent electronic conductivity but also because of the superb ionic conductivity due to the open structure of Ni foam. However, even though such design can provide some impressive properties, a stable cycling life is still not guaranteed especially when pseudocapacitive materials are employed. In order to further realize good cycle stability, a promising avenue is to coat a protective layer on the active materials. This is because the protective layer, such as conductive polymer layer, could effectively inhibit the dissolution of active materials, which might in turn retain a relative stable specific capacitance.

The future direction of nanoarchitectured design is not merely limited to the above-mentioned one. Other strategic directions can also be adopted if all the desired electrochemical performance can be obtained.

APPENDIX A:
COPYRIGHT PERMISSION LETTER FOR FIGURE 2.3

ELSEVIER LICENSE
TERMS AND CONDITIONS

Feb 16, 2015

This is a License Agreement between Zenan Yu ("You") and Elsevier ("Elsevier") provided by Copyright Clearance Center ("CCC"). The license consists of your order details, the terms and conditions provided by Elsevier, and the payment terms and conditions.

All payments must be made in full to CCC. For payment instructions, please see information listed at the bottom of this form.

Supplier	Elsevier Limited The Boulevard,Langford Lane Kidlington,Oxford,OX5 1GB,UK
Registered Company Number	1982084
Customer name	Zenan Yu
Customer address	12424 Research Parkway
	ORLANDO, FL 32826
License number	3571090779710
License date	Feb 16, 2015
Licensed content publisher	Elsevier
Licensed content publication	Journal of Power Sources
Licensed content title	Controllable preparation of multishelled NiO hollow nanospheres via layer-by-layer self-assembly for supercapacitor application
Licensed content author	Zeheng Yang,Feifei Xu,Weixin Zhang,Zhousheng Mei,Bo Pei,Xiao Zhu
Licensed content date	15 January 2014
Licensed content volume number	246
Licensed content issue number	n/a
Number of pages	8
Start Page	24
End Page	31
Type of Use	reuse in a thesis/dissertation
Intended publisher of new work	other
Portion	figures/tables/illustrations
Number of figures/tables/illustrations	4
Format	both print and electronic
Are you the author of this Elsevier article?	No

Will you be translating?	No
Title of your thesis/dissertation	Nanoarchitectured Energy Storage Devices
Expected completion date	Apr 2015
Estimated size (number of pages)	100
Elsevier VAT number	GB 494 6272 12
Permissions price	0.00 USD
VAT/Local Sales Tax	0.00 USD / 0.00 GBP
Total	0.00 USD
Terms and Conditions	

INTRODUCTION

1. The publisher for this copyrighted material is Elsevier. By clicking "accept" in connection with completing this licensing transaction, you agree that the following terms and conditions apply to this transaction (along with the Billing and Payment terms and conditions established by Copyright Clearance Center, Inc. ("CCC"), at the time that you opened your Rightslink account and that are available at any time at http://myaccount.copyright.com).

GENERAL TERMS

2. Elsevier hereby grants you permission to reproduce the aforementioned material subject to the terms and conditions indicated.

3. Acknowledgement: If any part of the material to be used (for example, figures) has appeared in our publication with credit or acknowledgement to another source, permission must also be sought from that source. If such permission is not obtained then that material may not be included in your publication/copies. Suitable acknowledgement to the source must be made, either as a footnote or in a reference list at the end of your publication, as follows:

“Reprinted from Publication title, Vol /edition number, Author(s), Title of article / title of chapter, Pages No., Copyright (Year), with permission from Elsevier [OR APPLICABLE SOCIETY COPYRIGHT OWNER].” Also Lancet special credit - “Reprinted from The Lancet, Vol. number, Author(s), Title of article, Pages No., Copyright (Year), with permission from Elsevier.”

4. Reproduction of this material is confined to the purpose and/or media for which permission is hereby given.

5. Altering/Modifying Material: Not Permitted. However figures and illustrations may be altered/adapted minimally to serve your work. Any other abbreviations, additions, deletions and/or any other alterations shall be made only with prior written authorization of Elsevier Ltd. (Please contact Elsevier at permissions@elsevier.com)

6. If the permission fee for the requested use of our material is waived in this instance, please be advised that your future requests for Elsevier materials may attract a fee.

APPENDIX B:
COPYRIGHT PERMISSION LETTER FOR FIGURE 2.4

JOHN WILEY AND SONS LICENSE
TERMS AND CONDITIONS

Feb 16, 2015

This Agreement between Zenan Yu ("You") and John Wiley and Sons ("John Wiley and Sons") consists of your license details and the terms and conditions provided by John Wiley and Sons and Copyright Clearance Center.

License Number	3571091118367
License date	Feb 16, 2015
Licensed Content Publisher	John Wiley and Sons
Licensed Content Publication	Advanced Energy Materials
Licensed Content Title	Core–Shell Structure of Polypyrrole Grown on V2O5 Nanoribbon as High Performance Anode Material for Supercapacitors
Licensed Content Author	Qunting Qu,Yusong Zhu,Xiangwen Gao,Yuping Wu
Licensed Content Date	May 9, 2012
Pages	6
Type of use	Dissertation/Thesis
Requestor type	University/Academic
Format	Print and electronic
Portion	Figure/table
Number of figures/tables	1
Original Wiley figure/table number(s)	Figure 1
Will you be translating?	No
Title of your thesis / dissertation	Nanoarchitectured Energy Storage Devices
Expected completion date	Apr 2015
Expected size (number of pages)	100
Requestor Location	Zenan Yu 12424 Research Parkway Suite 400 ORLANDO, FL 32826 United States Attn: Zenan Yu
Billing Type	Invoice
Billing Address	Zenan Yu 12424 Research Parkway Suite 400 ORLANDO, FL 32826

United States
Attn: Zenan Yu

Total 0.00 USD

Terms and Conditions

TERMS AND CONDITIONS

This copyrighted material is owned by or exclusively licensed to John Wiley & Sons, Inc. or one of its group companies (each a"Wiley Company") or handled on behalf of a society with which a Wiley Company has exclusive publishing rights in relation to a particular work (collectively "WILEY"). By clicking �accept� in connection with completing this licensing transaction, you agree that the following terms and conditions apply to this transaction (along with the billing and payment terms and conditions established by the Copyright Clearance Center Inc., ("CCC's Billing and Payment terms and conditions"), at the time that you opened your Rightslink account (these are available at any time at http://myaccount.copyright.com).

Terms and Conditions

- The materials you have requested permission to reproduce or reuse (the "Wiley Materials") are protected by copyright.

- You are hereby granted a personal, non-exclusive, non-sub licensable (on a stand-alone basis), non-transferable, worldwide, limited license to reproduce the Wiley Materials for the purpose specified in the licensing process. This license is for a one-time use only and limited to any maximum distribution number specified in the license. The first instance of republication or reuse granted by this licence must be completed within two years of the date of the grant of this licence (although copies prepared before the end date may be distributed thereafter). The Wiley Materials shall not be used in any other manner or for any other purpose, beyond what is granted in the license. Permission is granted subject to an appropriate acknowledgement given to the author, title of the material/book/journal and the publisher. You shall also duplicate the copyright notice that appears in the Wiley publication in your use of the Wiley Material. Permission is also granted on the understanding that nowhere in the text is a previously published source acknowledged for all or part of this Wiley Material. Any third party content is expressly excluded from this permission.

- With respect to the Wiley Materials, all rights are reserved. Except as expressly granted by the terms of the license, no part of the Wiley Materials may be copied, modified, adapted (except for minor reformatting required by the new Publication), translated, reproduced, transferred or distributed, in any form or by any means, and no derivative works may be made based on the Wiley Materials without the prior permission of the respective copyright owner. You may not alter, remove or suppress in any manner any copyright, trademark or other notices displayed by the Wiley Materials. You may not license, rent, sell, loan, lease, pledge, offer as security, transfer or assign the Wiley Materials on a stand-alone basis, or any of the rights granted to you hereunder to any other person.

- The Wiley Materials and all of the intellectual property rights therein shall at all times remain the exclusive property of John Wiley & Sons Inc, the Wiley Companies, or

APPENDIX C:
COPYRIGHT PERMISSION LETTER FOR FIGURE 2.5

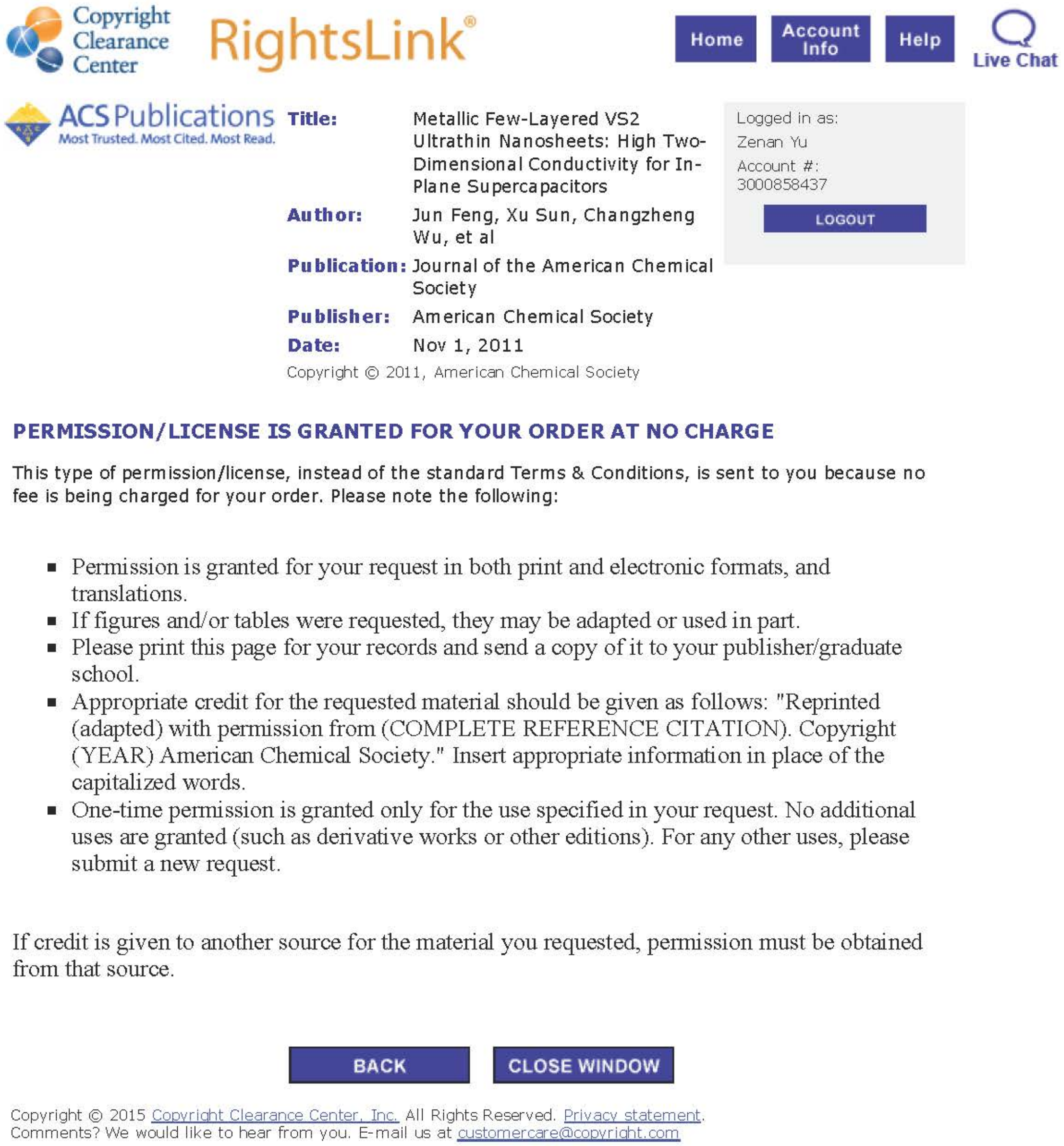

Title: Metallic Few-Layered VS2 Ultrathin Nanosheets: High Two-Dimensional Conductivity for In-Plane Supercapacitors

Author: Jun Feng, Xu Sun, Changzheng Wu, et al

Publication: Journal of the American Chemical Society

Publisher: American Chemical Society

Date: Nov 1, 2011

Copyright © 2011, American Chemical Society

Logged in as:
Zenan Yu
Account #:
3000858437

PERMISSION/LICENSE IS GRANTED FOR YOUR ORDER AT NO CHARGE

This type of permission/license, instead of the standard Terms & Conditions, is sent to you because no fee is being charged for your order. Please note the following:

- Permission is granted for your request in both print and electronic formats, and translations.
- If figures and/or tables were requested, they may be adapted or used in part.
- Please print this page for your records and send a copy of it to your publisher/graduate school.
- Appropriate credit for the requested material should be given as follows: "Reprinted (adapted) with permission from (COMPLETE REFERENCE CITATION). Copyright (YEAR) American Chemical Society." Insert appropriate information in place of the capitalized words.
- One-time permission is granted only for the use specified in your request. No additional uses are granted (such as derivative works or other editions). For any other uses, please submit a new request.

If credit is given to another source for the material you requested, permission must be obtained from that source.

Copyright © 2015 Copyright Clearance Center, Inc. All Rights Reserved. Privacy statement.
Comments? We would like to hear from you. E-mail us at customercare@copyright.com

APPENDIX D:
COPYRIGHT PERMISSION LETTER FOR FIGURE 2.6

ELSEVIER LICENSE
TERMS AND CONDITIONS

Feb 16, 2015

This is a License Agreement between Zenan Yu ("You") and Elsevier ("Elsevier") provided by Copyright Clearance Center ("CCC"). The license consists of your order details, the terms and conditions provided by Elsevier, and the payment terms and conditions.

All payments must be made in full to CCC. For payment instructions, please see information listed at the bottom of this form.

Supplier	Elsevier Limited The Boulevard,Langford Lane Kidlington,Oxford,OX5 1GB,UK
Registered Company Number	1982084
Customer name	Zenan Yu
Customer address	12424 Research Parkway ORLANDO, FL 32826
License number	3571100033253
License date	Feb 16, 2015
Licensed content publisher	Elsevier
Licensed content publication	Electrochimica Acta
Licensed content title	Structural evolution of multi-walled carbon nanotube/MnO2 composites as supercapacitor electrodes
Licensed content author	Qiang Li,Jordan M. Anderson,Yiqing Chen,Lei Zhai
Licensed content date	1 January 2012
Licensed content volume number	59
Licensed content issue number	n/a
Number of pages	10
Start Page	548
End Page	557
Type of Use	reuse in a thesis/dissertation
Intended publisher of new work	other
Portion	figures/tables/illustrations
Number of figures/tables/illustrations	1
Format	both print and electronic
Are you the author of this Elsevier article?	No

Will you be translating?	No
Title of your thesis/dissertation	Nanoarchitectured Energy Storage Devices
Expected completion date	Apr 2015
Estimated size (number of pages)	100
Elsevier VAT number	GB 494 6272 12
Permissions price	0.00 USD
VAT/Local Sales Tax	0.00 USD / 0.00 GBP
Total	0.00 USD
Terms and Conditions	

INTRODUCTION

1. The publisher for this copyrighted material is Elsevier. By clicking "accept" in connection with completing this licensing transaction, you agree that the following terms and conditions apply to this transaction (along with the Billing and Payment terms and conditions established by Copyright Clearance Center, Inc. ("CCC"), at the time that you opened your Rightslink account and that are available at any time at http://myaccount.copyright.com).

GENERAL TERMS

2. Elsevier hereby grants you permission to reproduce the aforementioned material subject to the terms and conditions indicated.

3. Acknowledgement: If any part of the material to be used (for example, figures) has appeared in our publication with credit or acknowledgement to another source, permission must also be sought from that source. If such permission is not obtained then that material may not be included in your publication/copies. Suitable acknowledgement to the source must be made, either as a footnote or in a reference list at the end of your publication, as follows:

“Reprinted from Publication title, Vol /edition number, Author(s), Title of article / title of chapter, Pages No., Copyright (Year), with permission from Elsevier [OR APPLICABLE SOCIETY COPYRIGHT OWNER].” Also Lancet special credit - “Reprinted from The Lancet, Vol. number, Author(s), Title of article, Pages No., Copyright (Year), with permission from Elsevier.”

4. Reproduction of this material is confined to the purpose and/or media for which permission is hereby given.

5. Altering/Modifying Material: Not Permitted. However figures and illustrations may be altered/adapted minimally to serve your work. Any other abbreviations, additions, deletions and/or any other alterations shall be made only with prior written authorization of Elsevier Ltd. (Please contact Elsevier at permissions@elsevier.com)

6. If the permission fee for the requested use of our material is waived in this instance, please be advised that your future requests for Elsevier materials may attract a fee.

APPENDIX E:

COPYRIGHT PERMISSION LETTERS FOR RELEVANT PUBLICATIONS UPON WHICH THIS DISSERTATION IS BASED ON IN PART

Supercapacitor electrode materials: nanostructures from 0 to 3 dimensions

Z. Yu, L. Tetard, L. Zhai and J. Thomas, *Energy Environ. Sci.*, 2015, Advance Article, **DOI:** 10.1039/C4EE03229B

JOHN WILEY AND SONS LICENSE
TERMS AND CONDITIONS

Dec 04, 2014

This is a License Agreement between Zenan Yu ("You") and John Wiley and Sons ("John Wiley and Sons") provided by Copyright Clearance Center ("CCC"). The license consists of your order details, the terms and conditions provided by John Wiley and Sons, and the payment terms and conditions.

All payments must be made in full to CCC. For payment instructions, please see information listed at the bottom of this form.

License Number	3521970452886
License date	Dec 04, 2014
Licensed content publisher	John Wiley and Sons
Licensed content publication	Advanced Materials
Licensed content title	Highly Ordered MnO2 Nanopillars for Enhanced Supercapacitor Performance
Licensed copyright line	Copyright © 2013 WILEY-VCH Verlag GmbH & Co. KGaA, Weinheim
Licensed content author	Zenan Yu,Binh Duong,Danielle Abbitt,Jayan Thomas
Licensed content date	May 2, 2013
Start page	3302
End page	3306
Type of use	Dissertation/Thesis
Requestor type	Author of this Wiley article
Format	Print and electronic
Portion	Full article
Will you be translating?	No
Title of your thesis / dissertation	Nanoarchitectured Energy Storage Devices
Expected completion date	Apr 2015
Expected size (number of pages)	100
Total	0.00 USD
Terms and Conditions	

TERMS AND CONDITIONS

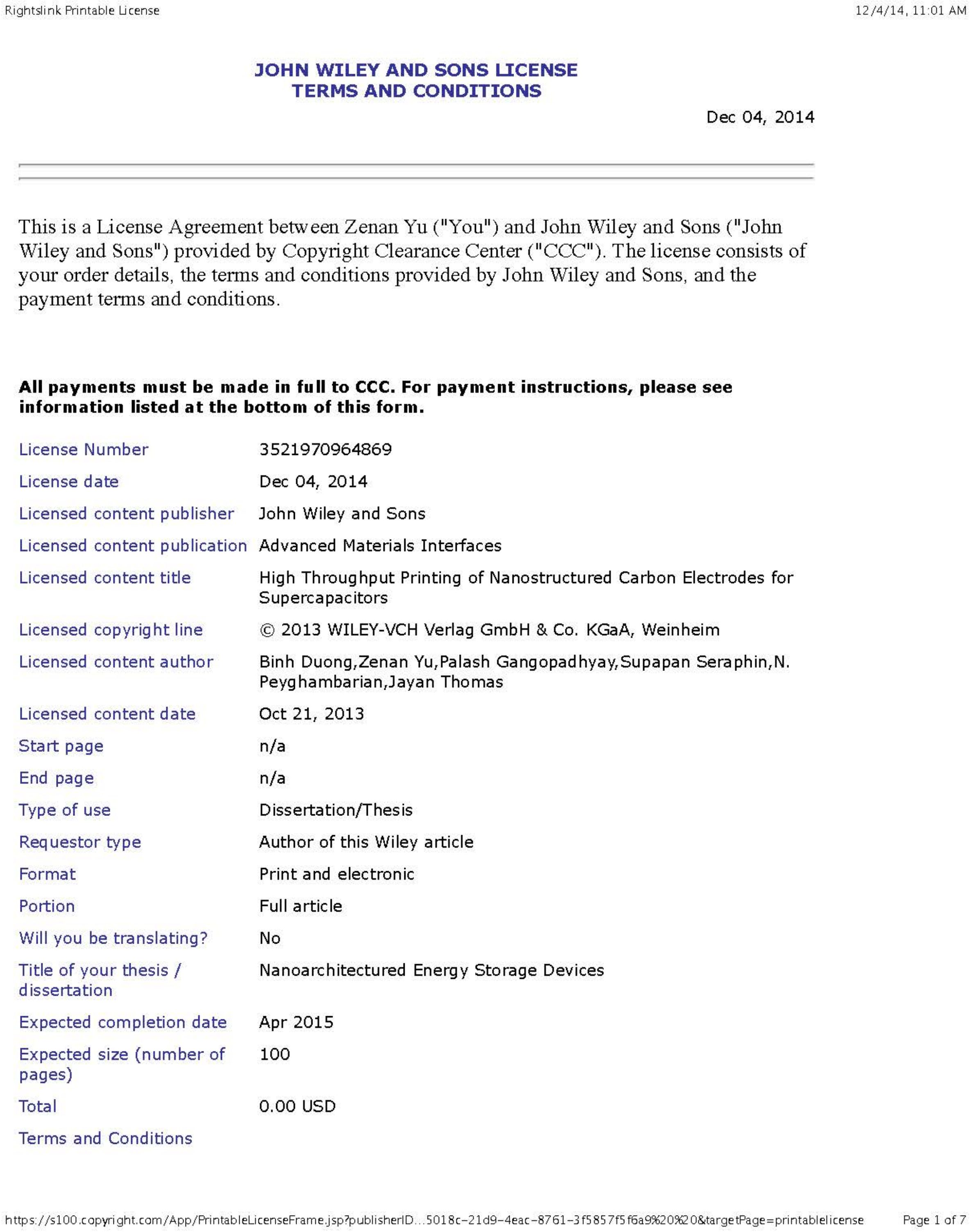

JOHN WILEY AND SONS LICENSE
TERMS AND CONDITIONS

Dec 04, 2014

This is a License Agreement between Zenan Yu ("You") and John Wiley and Sons ("John Wiley and Sons") provided by Copyright Clearance Center ("CCC"). The license consists of your order details, the terms and conditions provided by John Wiley and Sons, and the payment terms and conditions.

All payments must be made in full to CCC. For payment instructions, please see information listed at the bottom of this form.

License Number	3521970964869
License date	Dec 04, 2014
Licensed content publisher	John Wiley and Sons
Licensed content publication	Advanced Materials Interfaces
Licensed content title	High Throughput Printing of Nanostructured Carbon Electrodes for Supercapacitors
Licensed copyright line	© 2013 WILEY-VCH Verlag GmbH & Co. KGaA, Weinheim
Licensed content author	Binh Duong,Zenan Yu,Palash Gangopadhyay,Supapan Seraphin,N. Peyghambarian,Jayan Thomas
Licensed content date	Oct 21, 2013
Start page	n/a
End page	n/a
Type of use	Dissertation/Thesis
Requestor type	Author of this Wiley article
Format	Print and electronic
Portion	Full article
Will you be translating?	No
Title of your thesis / dissertation	Nanoarchitectured Energy Storage Devices
Expected completion date	Apr 2015
Expected size (number of pages)	100
Total	0.00 USD
Terms and Conditions	

JOHN WILEY AND SONS LICENSE
TERMS AND CONDITIONS

Dec 04, 2014

This is a License Agreement between Zenan Yu ("You") and John Wiley and Sons ("John Wiley and Sons") provided by Copyright Clearance Center ("CCC"). The license consists of your order details, the terms and conditions provided by John Wiley and Sons, and the payment terms and conditions.

All payments must be made in full to CCC. For payment instructions, please see information listed at the bottom of this form.

License Number	3521970837862
License date	Dec 04, 2014
Licensed content publisher	John Wiley and Sons
Licensed content publication	Advanced Materials
Licensed content title	Energy Storing Electrical Cables: Integrating Energy Storage and Electrical Conduction
Licensed copyright line	© 2014 WILEY-VCH Verlag GmbH & Co. KGaA, Weinheim
Licensed content author	Zenan Yu,Jayan Thomas
Licensed content date	Mar 27, 2014
Start page	4279
End page	4285
Type of use	Dissertation/Thesis
Requestor type	Author of this Wiley article
Format	Print and electronic
Portion	Full article
Will you be translating?	No
Title of your thesis / dissertation	Nanoarchitectured Energy Storage Devices
Expected completion date	Apr 2015
Expected size (number of pages)	100
Total	0.00 USD
Terms and Conditions	

TERMS AND CONDITIONS

ELSEVIER LICENSE
TERMS AND CONDITIONS

Jan 27, 2015

This is a License Agreement between Zenan Yu ("You") and Elsevier ("Elsevier") provided by Copyright Clearance Center ("CCC"). The license consists of your order details, the terms and conditions provided by Elsevier, and the payment terms and conditions.

All payments must be made in full to CCC. For payment instructions, please see information listed at the bottom of this form.

Supplier	Elsevier Limited The Boulevard,Langford Lane Kidlington,Oxford,OX5 1GB,UK
Registered Company Number	1982084
Customer name	Zenan Yu
Customer address	12424 Research Parkway ORLANDO, FL 32826
License number	3557140270669
License date	Jan 27, 2015
Licensed content publisher	Elsevier
Licensed content publication	Nano Energy
Licensed content title	Functionalized graphene aerogel composites for high-performance asymmetric supercapacitors
Licensed content author	None
Licensed content date	January 2015
Licensed content volume number	11
Licensed content issue number	n/a
Number of pages	10
Start Page	611
End Page	620
Type of Use	reuse in a thesis/dissertation
Portion	full article
Format	both print and electronic
Are you the author of this Elsevier article?	Yes
Will you be translating?	No
Title of your thesis/dissertation	Nanoarchitectured Energy Storage Devices

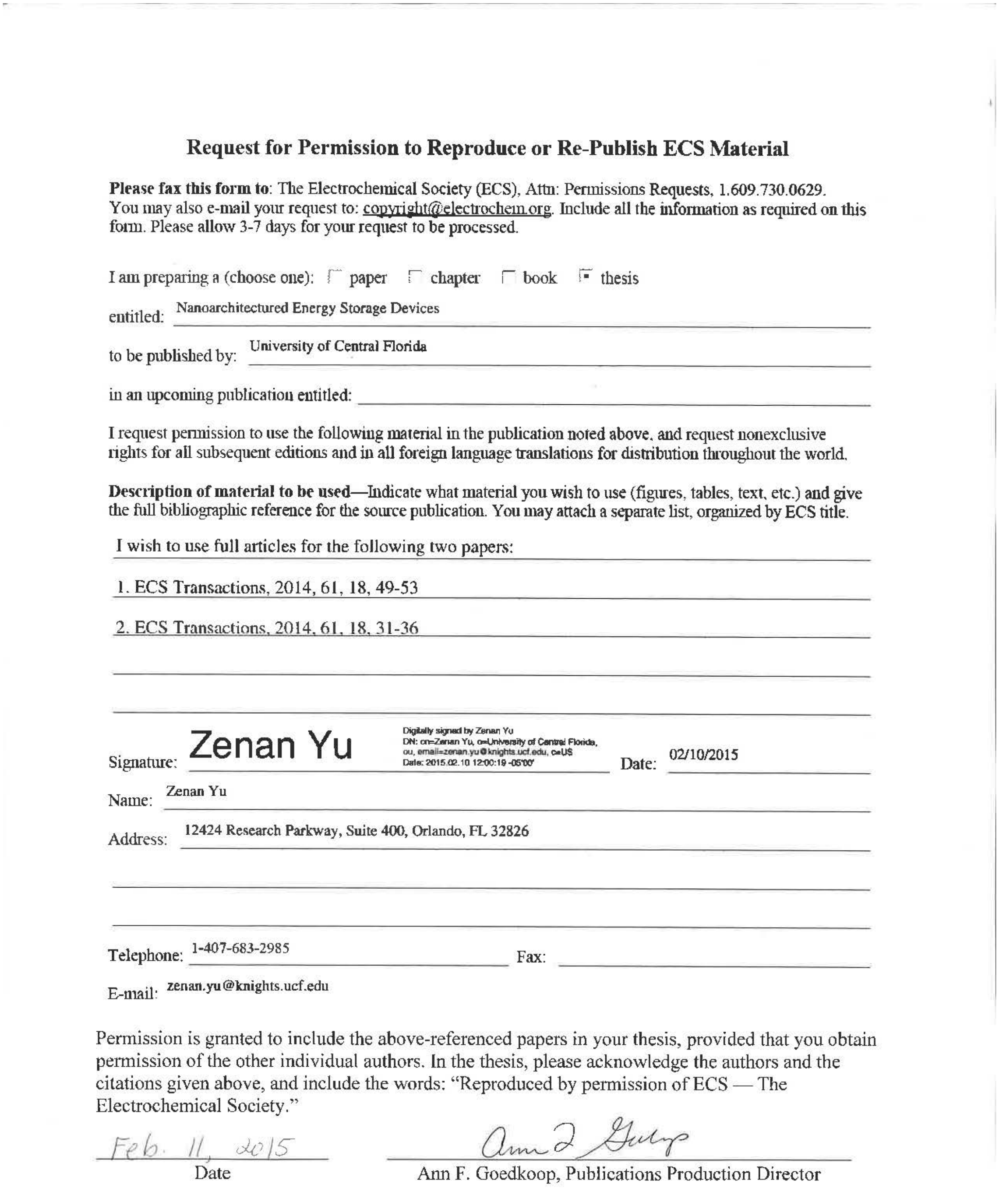

Request for Permission to Reproduce or Re-Publish ECS Material

Please fax this form to: The Electrochemical Society (ECS), Attn: Permissions Requests, 1.609.730.0629. You may also e-mail your request to: copyright@electrochem.org. Include all the information as required on this form. Please allow 3-7 days for your request to be processed.

I am preparing a (choose one): ☐ paper ☐ chapter ☐ book ☒ thesis

entitled: Nanoarchitectured Energy Storage Devices

to be published by: University of Central Florida

in an upcoming publication entitled:

I request permission to use the following material in the publication noted above, and request nonexclusive rights for all subsequent editions and in all foreign language translations for distribution throughout the world.

Description of material to be used—Indicate what material you wish to use (figures, tables, text, etc.) and give the full bibliographic reference for the source publication. You may attach a separate list, organized by ECS title.

I wish to use full articles for the following two papers:

1. ECS Transactions, 2014, 61, 18, 49-53

2. ECS Transactions, 2014, 61, 18, 31-36

Signature: Zenan Yu Digitally signed by Zenan Yu DN: cn=Zenan Yu, o=University of Central Florida, ou, email=zenan.yu@knights.ucf.edu, c=US Date: 2015.02.10 12:00:19 -05'00' Date: 02/10/2015

Name: Zenan Yu

Address: 12424 Research Parkway, Suite 400, Orlando, FL 32826

Telephone: 1-407-683-2985 Fax:

E-mail: zenan.yu@knights.ucf.edu

Permission is granted to include the above-referenced papers in your thesis, provided that you obtain permission of the other individual authors. In the thesis, please acknowledge the authors and the citations given above, and include the words: “Reproduced by permission of ECS — The Electrochemical Society.”

Feb. 11, 2015
Date

Ann F. Goedkoop, Publications Production Director

APPENDIX F:
LIST OF RELEVANT PUBLICATIONS

This dissertation is based in part on the following publications:

1. Z. Yu, J. Moore, L. Tetard, L. Zhai and J. Thomas, “Recent progress in asymmetric supercapacitors” *Adv. Mater.* In preparation. (Invited)
2. Z. Yu, J. Moore, J. Calderon, L. Zhai, and J. Thomas, “Coil-type asymmetric supercapacitor electrical cables” Submitted.
3. Z. Yu, L. Tetard, L. Zhai and J. Thomas, “Supercapacitor electrode materials: Nanostructures from 0 to 3 dimensions” *Energy Environ. Sci.* 2015, 8, 702-730.
4. Z. Yu, M. McInnis, J. Calderon, S. Seal, L. Zhai, and J. Thomas, “Functionalized graphene aerogel composites for high-performance asymmetric supercapacitors” *Nano Energy* 2015, 11, 611-620.
5. Z. Yu, and J. Thomas, “Energy storing electrical cables: Integrating energy storage and electrical conduction” *Adv. Mater.* 2014, 26, 4279-4285.
6. Z. Yu, C. Li, D. Abbitt, and J. Thomas, “Flexible, sandwich-like Ag- nanowire/PEDOT:PSS-nanopillar/MnO_2 high performance supercapacitor” *J. Mater. Chem. A* 2014, 2, 10923-10929.
7. Z. Yu, J. Moore, B. Duong, C. Li, and J. Thomas, "PAN@ AuPd@ MnO2 core-shell nanopillars for high-performance electrochemical energy storage", *ECS Trans.* 2014, 61, 49-53.
8. Z. Yu, J. Moore, J. Lorenzo, C. Li, and J. Thomas, "Dual-function coaxial supercapacitor cable", *ECS Trans.* 2014, 61, 31-36.

9. B. Duong, Z. Yu, P. Gangopadhyay, S. Seraphin, N. Peyghambarian, and J. Thomas, “High throughput printing of nanostructured carbon electrodes for supercapacitors” *Adv. Mater. Interfaces* 2014, 1, 130014.

10. Z. Yu, B. Duong, D. Abbitt and J. Thomas, “Highly ordered MnO_2 nanopillars for enhanced supercapacitor performance” *Adv. Mater.* 2013, 25, 3302-3306.